EXPERIMENTAL CONSTRAINTS ON NUCLEOSYNTHESIS IN OXYGEN-NEON NOVAE

By

Cathleen Fry

A DISSERTATION

Submitted
to Michigan State University
in partial fulfillment of the requirements
for the degree of

Physics – Doctor of Philosophy

2018

ProQuest Number: 10976193

ProQuest 10976193

ABSTRACT

EXPERIMENTAL CONSTRAINTS ON NUCLEOSYNTHESIS IN OXYGEN-NEON NOVAE

By

Cathleen Fry

Classical novae occur in close binary systems consisting of a white dwarf and a star with a hydrogen rich envelope. The white dwarf accretes hydrogen which ignites in a thermonuclear runaway. Nucleosynthesis proceeds close to the valley of stability through a series of (p, γ) and (p, α) reactions and β^+ decays. Each of these events ejects $10^{-7} - 10^{-3}$ $M_\odot$ of material. Some of this ejected material condenses into grains, and these grains can be identified in primitive meteorites by comparing their measured isotopic ratios to those predicted by various stellar models.

The $^{30}P(p, \gamma)^{31}S$ reaction rate potentially acts as a bottleneck, controlling nucleosynthetic flow in the $30 \leq A \leq 40$ region. Large uncertainties in this rate dominate the uncertainty in expected silicon isotopic ratios and also certain elemental ratios which have been proposed to help constrain the peak temperatures reached in classical novae. Resonances expected to contribute to this rate are known, but the corresponding resonance strengths are not known. As a step towards determining experimental resonance strengths, we ran an experiment to determine lifetimes of these states populated via the $^{32}S(^3He,\alpha)^{31}S$ reaction and using the Doppler Shift Lifetime chamber and GRIFFIN detectors at TRIUMF. Our initial run failed due to a number of issues. Diagnosis of those issues and improvements informed by this analysis are discussed. Preliminary data from a second run are included to demonstrate improvements in our setup. Two states in the region of astrophysical interest have been observed, and we expect to be able to provide constraints on the lifetimes of these two states as well as a number of bound states.

Similarly, the $^{34g,m}Cl(p, \gamma)^{35}Ar$ reaction rate impacts predictions of sulfur isotopic ratios. These ratios were only very recently measured in nova candidate grains, and other measured isotopic ratios (C, N, Si) are not currently sufficient to distinguish between classical nova and type II supernova grain origins. As a first step toward determining this reaction rate, we have performed

an experiment at Maier-Leibniz Laboratorium using the ^{36}Ar$(d,t)^{35}$Ar reaction to populate the states of interest and a Q3D magnetic spectrograph to extract excitation energies. 17 new levels have been discovered, and the uncertainties associated with previously known levels have been reduced from 10 keV to typically 3 keV.

To perserverance

ACKNOWLEDGMENTS

Without my advisor, Chris Wrede, none of this dissertation work would have been possible. Chris gave me a lot of space and opportunities to grow as a scientist. When something went wrong, he was always ready with another plan, with something else we could try. If he didn't have funding for a summer school, conference, or experiment I wanted to attend, he was always supportive of me writing small travel grants. While my path through grad school was bumpy and nonlinear, he and the rest of my committee, Alex Brown, Laura Chomiuk, Wade Fisher, and Artemis Spyrou, stuck with me through a few project changes.

I'm grateful for the entire Wrede group. David Pérez-Loureiro and Mike Bennett were particularly helpful as I was getting started in grad school. Brent Glassman and I have been in the group together for over five years now, and he was always willing to listen to me talk through a problem. Sarah Schwartz, Jason Surbrook, Tamas Budner, and Moshe Friedman have also provided helpful input throughout my career. While our group has had many undergraduate students in my time as a graduate student, I have to give special thanks to Pranjal Tiwari for his patience while I learned how to be a mentor.

As someone who lead experiments at two different facilities in different countries, I have collaborators all over the world to thank for their successes. For my first experiment, in only my second semester of graduate school, I have to thank Alan Chen and Anuj Parikh, as well as the local group at MLL. My second experiment ran twice, and there are numerous people to thank for making that happen. In particular, Barry Davids provided a lot of insight into this project, from proposal writing to target making to data analysis. Oliver Kirsebom provided me with a lot of tools he developed for the analysis of another dataset from the DSL setup. Nick Esker was invaluable in the second run, and I'm glad to leave the remaining data analysis in his hands.

I also have to thank the people that helped me find my love of nuclear physics. Michael Thoennessen provided me with an excellent opportunity to learn about the history of nuclear physics

TABLE OF CONTENTS

LIST OF TABLES

LIST OF FIGURES

CHAPTER 1

INTRODUCTION

Where were the elements in the universe synthesized? How were they synthesized? How do we explain the observed abundance patterns? What drives energy generation in stars? These are some of the questions nuclear astrophysics seeks to answer.

1.1   Nuclear astrophysics

A star at the beginning of its lifetime is made predominantly of ^{1}H and ^{4}He. Once the core of the star has reached sufficient temperatures, the ^{1}H can be fused to form ^{4}He and release ≈ 30 MeV of energy per ^{4}He. Once this hydrogen is depleted in the core, if the star is massive enough (>0.7 M$_{\odot}$), gravitational contraction increases the temperature and pressure in the star. The star then burns ^{4}He to form ^{12}C and ^{16}O, and releases energy. This series of contractions and burning in sufficiently large stars can liberate energy and synthesize elements up to the iron region, where ^{56}Fe, ^{58}Fe, and ^{62}Ni have the highest binding energy per nucleon, as seen in Figure 1.1.
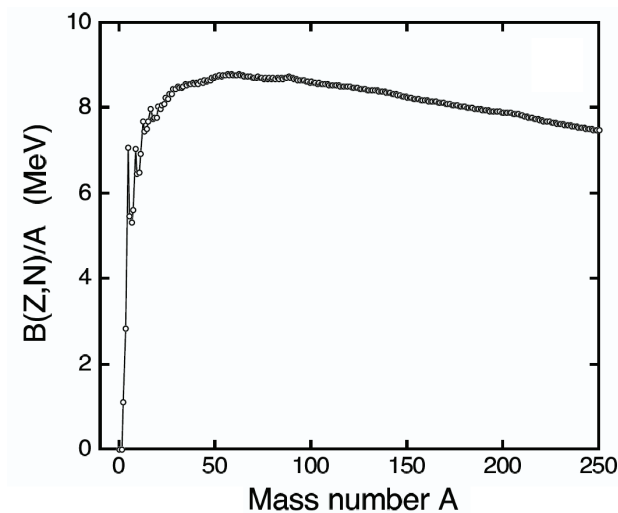
Figure 1.1 Binding energy per nucleon as a function of mass number, *A*. Figure from [1].

Elements with higher masses are energetically unfavorable to produce, and are not explained by quiescent burning in stars. These elements are synthesized in more extreme stellar environments. Due to the high Coulomb barrier, charged particle fusion is hindered, but a series of neutron captures and β^- decays can bypass this issue. In the r-process, neutron captures are rapid, relative to the β^- decay rates. In contrast, the s-process, neutron captures are slow relative to the β^- decay rates, and proceeds much closer to stability. These two processes account for the production of most nuclei heavier than iron, while another process is needed to produce the p-nuclei, which are neutron deficient isotopes blocked by other stable isotopes from s- and r-processes.

1.2   Binary star systems

A binary star system consists of two stars orbiting their center of mass., and roughly half of stars exist in binary systems. If the stars differ in mass, their rate of evolution and orbital speeds will differ. Each star has a Roche lobe, within which orbiting materials are gravitationally bound to the star, and if the star extends past its Roche lobe, the extended material can be transferred to the companion star [1]. At the inner Lagrangian point, the gravitational potentials of the two stars are equal. A diagram of the binary system can be seen in Figure 1.2.
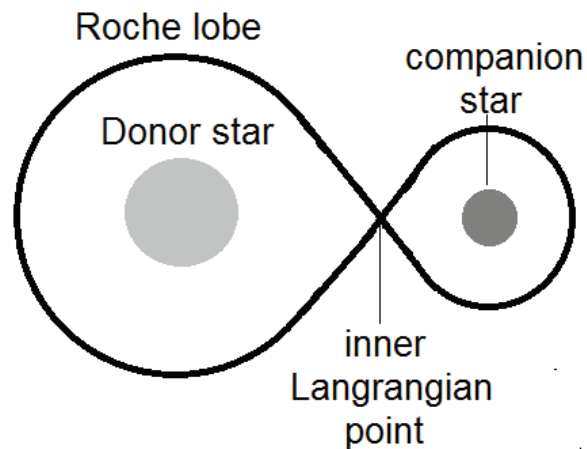
Figure 1.2 Diagram of the binary system. Each star, their Roche lobes, and the inner Lagrangian point are labeled.

1.2.1 Classical novae

Classical novae occur in close binary systems consisting of a white dwarf and a companion star with a hydrogen rich envelope. When the material on the surface of the companion star overflows its Roche lobe, the material can be transferred to the white dwarf. This material collects in an accretion disk surrounding the white dwarf. Some of this matter accumulates on the surface of the white dwarf and is heated by the high gravitational potential. This inner shell eventually becomes degenerate, and hot enough to ignite hydrogen burning, increasing temperature. This does not expand the degenerate layer, and the temperature continues to increase. This leads to thermonuclear runaway on the accreted material, eventually causing an explosion.

Nova outbursts eject $\approx 10^{-7} - 10^{-3}$ $M_\odot$ of material at velocities on the order of 10^6 m/s, reach peak luminosities of 10^5 $L_\odot$, and reach peak temperatures of 0.1-0.4 GK. These events can recur on typical time scales of 10^4-10^5 years. Approximately 35 occur in the Galaxy per year, of which 5-10 are detected. The other events are obscured by dust in the plane of the galaxy. These events have been observed throughout the entire electromagnetic spectrum [17].

1.3 Stellar dust

Many stellar events are known to eject matter, including classical novae. While most of this matter enters the interstellar medium in the form of a gas, some of the ejecta can condense and form dust, or small grains, typically a few µm or smaller. This dust has been observed through a variety of observational astronomy techniques and is predicted in theoretical models.

Gas phase material from the bulk of stellar sources are homogenized in the interstellar medium, creating uniform isotopic ratios in many situations. However, primitive meteorites have been found to contain small (nm-µm) grains that do not show these uniform isotopic signatures. An explanation given for this is that these grains were formed in a star, ejecta, or stellar winds and stayed intact during the homogenization of the interstellar medium and the formation of the solar system.

1.3.1 Modeling of grain formation

Some stellar events that return matter to the interstellar medium are dusty, and these stellar sources will each be discussed in this subsection. This newly made stardust moves away from its stellar source and travels through the interstellar medium. These grains can collapse together with gas forming a new star, which is a relatively slow process. Through various processes, the composition of these grains is altered and only a small fraction of grains maintain their initial composition [18].

In a core collapse supernova model, the core continues contracting after Si burning, as the Fe-core gains mass until it reaches a Chandrasekhar mass and eventually collapses. After this explosion occurs, the knowledge of chemical yields is necessary to understand the ejecta. A blast wave deposits energy as it crosses the ejected materials. Neutrino-driven convection leads to mixing in the core, which occurs over a few hours and leads to a partial fragmentation of the core. After this mixing, the abundances are assumed to remain constant within each mass zone.

Chemical processes are assumed to not be effective before around day 100, due to the high temperatures. The temperature evolution within the ejecta is controlled by the deposition of energy from γ-rays and x-rays, which depend on elemental abundances at a given time. Chemical processes such as thermomolecular reactions, thermal fragmentation, and radiative association are then considered and evolved based on the temperature and density profile. A chemical network is then evolved to determine the formation of molecules which then condense into grains. Nucleation of these molecules into grains is the bottleneck of the grain formation process [2]. The time evolution of the total mass of several grain types can be seen in Figure 1.3.

Presolar grains from CO novae have not yet been measured in the laboratory, but this absence of SiC and graphite grains is consistent with condensation calculations for CO nova ejecta, due to higher abundance of oxygen relative to carbon. This leads carbon to be locked into CO molecules leaving oxygen to form oxide and silicate grains [4].

Other types of stellar events that produce presolar grains include type Ia supernovae, asymptotic giant branch (AGB) stars, and Wolf-Rayet stars. The known presolar minerals from giant stars
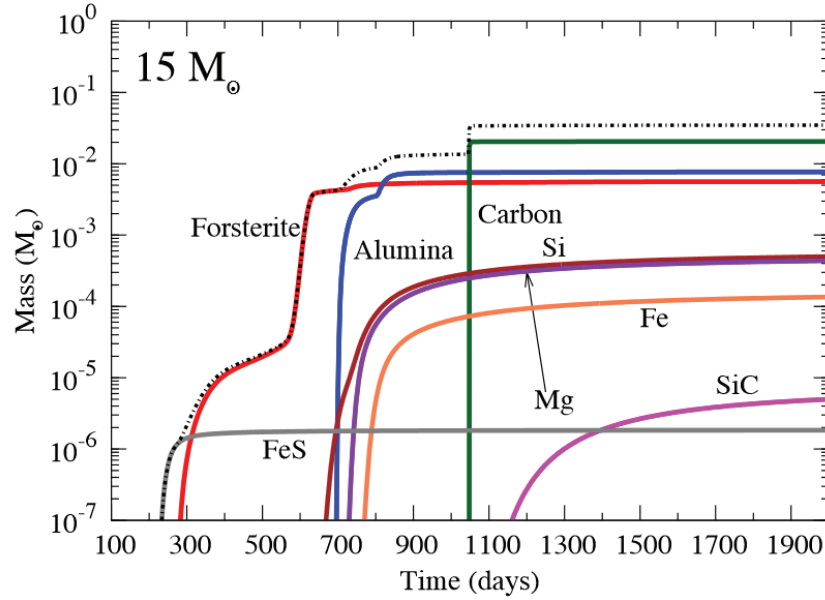
Figure 1.3 Dust mass for grains larger than 10 Å summed over ejecta zones in a type II supernova as a function of time post explosion. The dotted line shows the sum of all dust mass formed in the model with a progenitor of 15 $M_\odot$. Figure from [2].

include corundum, spinel, hibonite, silicon carbide and silicate grains. Graphite grains with high $^{12}C/^{13}C$ ratios are also potentially from these sites, as well as potentially some diamonds [19].

1.4 Presolar grains

Dust grains in the solar system that were condensed before the solar system formed are referred to as presolar grains. Some of these grains can be found within meteorites that have fallen to earth. They are characterized by isotopic ratios that differ from measured solar isotopic ratios. These grains can then be identified with sources by comparing measured isotopic ratios to model predictions for various stellar events outlined in subsection 1.3.1. A cartoon of the steps from grain formation to identification can be seen in Figure 1.4.

These grains can condense into several different minerals. In this subsection, several of the currently observed grain types are discussed. Suggested origins for some of these grains are given. Most of these grains have typical sizes of micrometers, whereas nanodiamonds are a notable exception, with sizes on the order of nanometers.

5
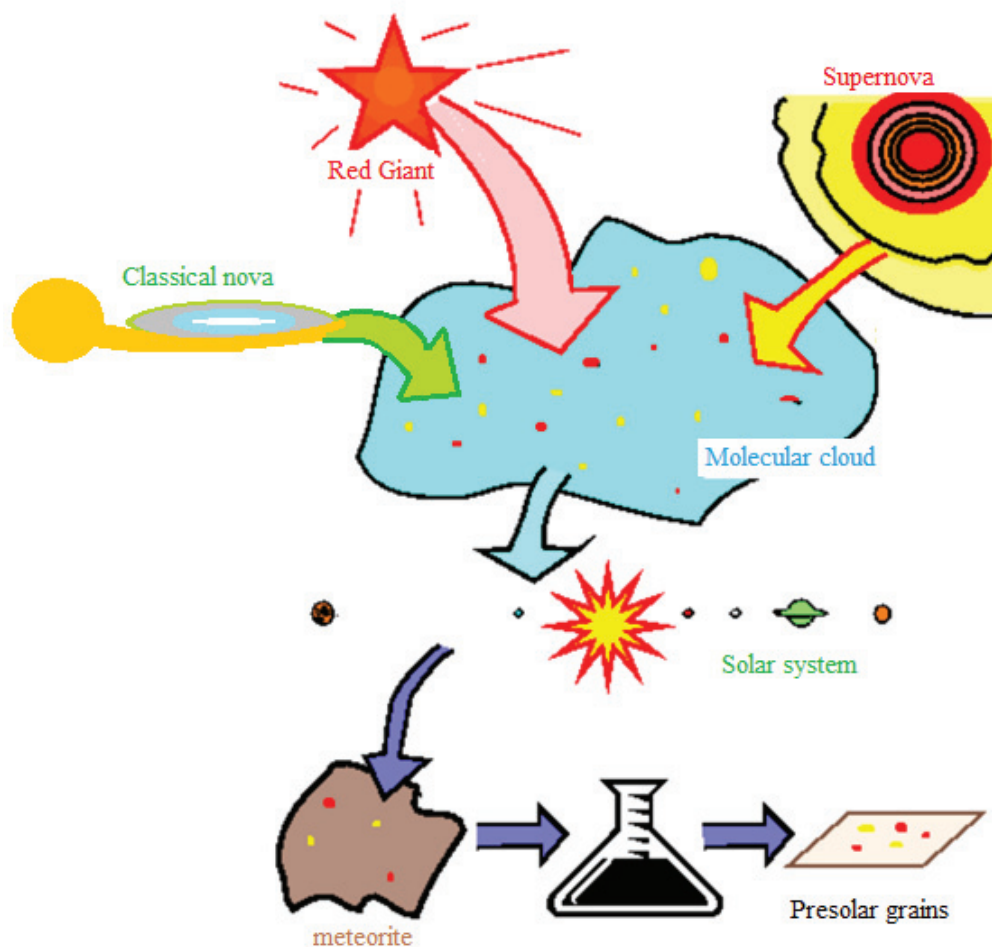
Figure 1.4 Cartoon of the steps from presolar grain formation through identification. Figure adapted from [3].

Nanodiamonds ($\sim$2.5 nm diameter) are the most abundant presolar grain, and many are identified by their Xe and Te isotopic ratios, which suggest type II supernovae origins. Isotopic measurements are limited by the small size and they must be measured in aggregate. C isotopic ratios are indistinguishable from solar ratios and nitrogen ratios are similar to solar in these grains. It has been suggested, based on this information, that the majority of nanodiamonds were formed in the solar system, and that only a small fraction are from supernovae [20].

Silicon carbide grains are the best studied type of grain, and isotopic measurements of single grains have revealed isotopic anomalies in nearly all measured elements. 90% of these grains have been identified as part of the "mainstream" population, and the remaining groups are much smaller.

One of these remaining groups is classical nova candidate grains. AGB stars are the proposed site for the formation of mainstream grains [21].
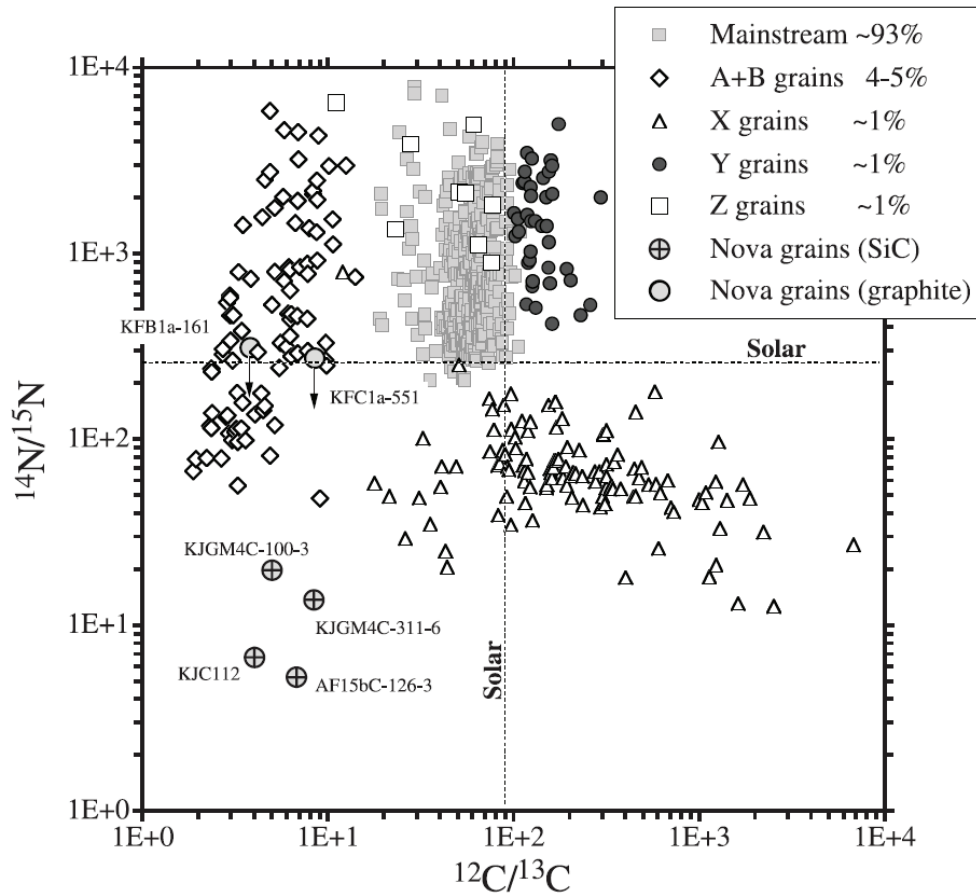
Figure 1.5 Measured C and N isotopic ratios for various presolar grains. The dotted lines are used to show solar isotopic ratios. Figure from [4].

Presolar graphite is less well understood. Subgrains have been found within these grains, which likely served as nucleation seeds for the condensation of the graphite. The majority of these grains are enriched in ^{12}C and have close to solar N ratios. Lower density grains have higher contents of trace elements and have similar isotopic ratios to those of SiC X-grains, which likely originated in supernovae. The higher density grains are proposed to have originated from several environments, including AGB stars, supernovae, and novae [21]. Secondary electron micrographs of two graphite grains and SiC grain are shown in Figure 1.6.

Unlike other grain types, only ~200 presolar oxide grains (mostly spinel and corundum) have

been identified, and they are expected to make a small contribution to the bulk of the interstellar dust. These are difficult to locate due to the large background from oxides with solar isotopic ratios. Most of the oxide grains are believed to have originated from O-rich red giants, and a supernova origin has been suggested for a few others. There is still no explanation for Group 4 grains, based on their O isotopic ratios [21].
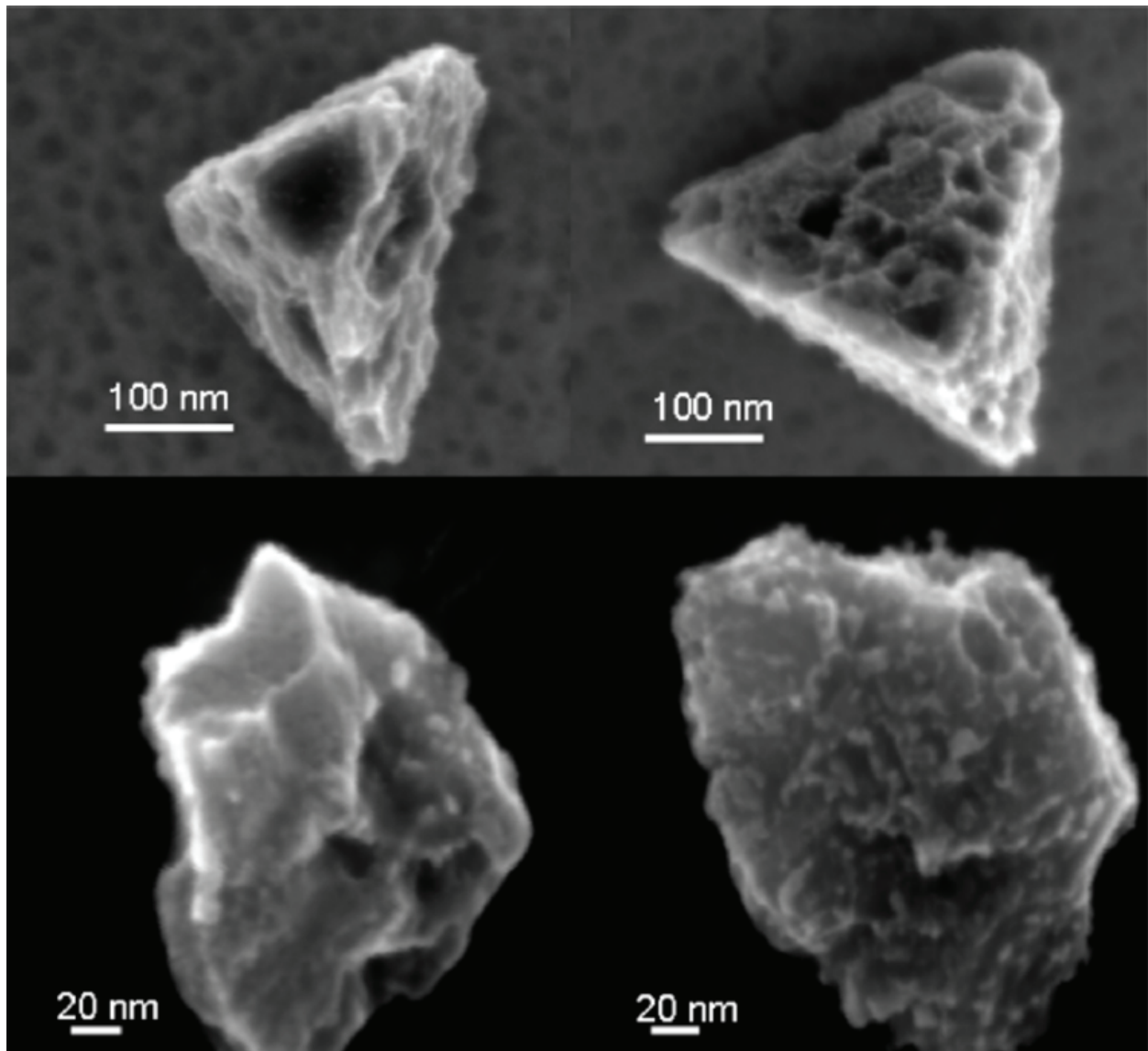
Figure 1.6 Secondary electron micrographs of silicon carbide grains from the Murchison meteorite. Figure from [5].

CHAPTER 2

CLASSICAL NOVA NUCLEOSYNTHESIS

This chapter discusses nucleosynthesis in classical novae. The study of two particular reactions, $^{30}\text{P}(p,\gamma)^{31}\text{S}$ and $^{34\text{g,m}}\text{Cl}(p,\gamma)^{35}\text{Ar}$, is motivated, and an overview of the currently available experimental information is given for both of these reactions.

Classical novae can be divided into two types, based on the type of underlying white dwarf. For main sequence stars with masses of 0.5 to 8 $M_\odot$, the core will contain carbon and oxygen, but not reach sufficient temperatures to produce neon. Stars with slightly higher masses, up to $\approx 10\ M_\odot$, can reach high enough temperatures to create neon [1]. CO novae are enriched in C, N, and O. In both cases, sufficient temperatures are not reached for significant breakout from the CNO hydrogen-burning cycle. ONe novae result in higher peak temperatures and nucleosynthesis proceeding on Ne and Mg seeds from the underlying white dwarf.

In most ONe classical novae elements as heavy as ^{40}Ca are believed to be synthesized through (p,γ) and (p,α) reactions and β^+ decays [1]. In comparison to other sites of explosive nucleosynthesis, the reaction path in novae is relatively localized near the valley of β stability. As a result, experimental information on the relevant nuclear reactions is abundant and there is a realistic opportunity to produce a complete set of experimentally determined reaction rates. The classical nova nucleosynthesis path can be seen in Figure 2.1.

2.1 Reaction rate formalism

Following the derivation in [1], consider a reaction of the type A(a,b)B, where a and A are both massive particles (not photons). The rate of this reaction can be described as

$$r_{aA} = N_a N_A v \sigma(v) \tag{2.1}$$
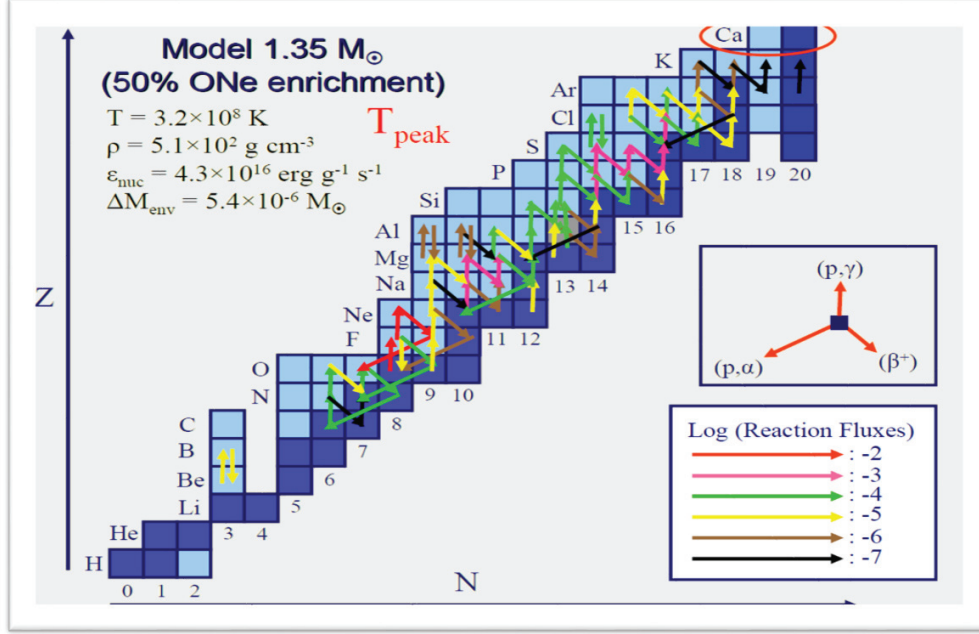
Figure 2.1 Classical nova nucleosynthesis path for a 1.35 $M_\odot$ ONe nova at peak temperature. Figure from [6].

where N_a and N_A are the number densities of particles a and A, v is the relative velocity, and $\sigma(v)$ is the nuclear cross section as a function of velocity. In a stellar plasma in thermodynamic equilibrium, the relative velocities are given by a probability distribution, $P(v)$. Given a distribution, the reaction rate can be written as

$$r_{aA} = N_a N_A \int_0^\infty v P(v) \sigma(v) dv = N_a N_A \langle \sigma v \rangle_{aA} \tag{2.2}$$

where $\langle \sigma v \rangle_{aA}$ is the reaction rate per particle pair. In a stellar plasma, nuclei typically move non-relativistically and are not degenerate. Therefore, the velocity distribution is given by the Maxwell-Boltzmann distribution.

$$P(v) = \left(\frac{m_{aA}}{2\pi kT} \right)^{3/2} e^{-m_{aA} v^2 / (2kT)} 4\pi v^2 \tag{2.3}$$

where k is the Boltzmann constant, T is the temperature, and m_{aA} is the reduced mass. The reaction rate per particle pair can then be written in terms of velocity or kinetic energy, as

$$\langle \sigma v \rangle = \int_0^\infty v P(v) \sigma(v) dv = \left(\frac{8}{\pi m_{aA}} \right)^{1/2} \frac{1}{(kT)^{3/2}} \int_0^\infty E \sigma(E) e^{-E/kT} dE. \tag{2.4}$$

10

The energy range where most charged particle nuclear reactions take place is strongly affected by two factors. The probability of penetrating the Coulomb barrier increases with energy, and probability to penetrate the Coulomb barrier is given by $e^{-2\pi\eta}$ where η is the Sommerfeld parameter, $\eta = \alpha Z_a Z_b \sqrt{\mu c^2/2E}$. However, the number of particles that have high energy is quite small, in the high energy tail of the Maxwell-Boltzmann distribution. These factors can be seen in Figure 2.2. Combining these two factors leads to the Gamow peak. This range is characterized by a centroid given by

$$E_0 = \left[\left(\frac{\pi}{\hbar} \right)^2 \left(Z_0 Z_1 e^2 \right)^2 \left(\frac{m_{aA}}{2} \right) (kT)^2 \right]^{1/3} \tag{2.5}$$

and a $1/e$ width Δ given by

$$\Delta = \frac{4}{\sqrt{3}} \sqrt{E_0 kT} \tag{2.6}$$

Thermonuclear reactions occur mainly in the energy range of $E_0 - \Delta/2$ to $E_0 + \Delta/2$.
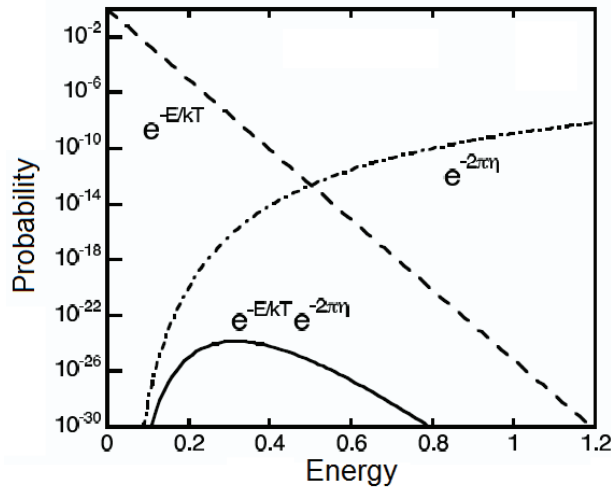
Figure 2.2 Graph showing the two components that contribute to the Gamow peak, the energy distribution, and Coulomb barrier penetrability. Figure from [1].

This work considers resonant capture reactions, where a particle is captured into an excited state in the compound nucleus, which enhances the reaction rate. Here, we consider narrow resonances, where the level density is sufficiently low that resonances have no significant overlap and the partial width is approximately constant across each resonance (the total width is less than a few keV, which corresponds to a lifetime $\approx 10^{-18}$ s or longer). The cross section for isolated resonances

can be described by a Breit-Wigner form given by

$$\sigma_{BW}(E) = \frac{\lambda^2}{4\pi} \frac{(2J+1)(1+\delta_{aA})}{(2J_a+1)(2J_A+1)} \frac{\Gamma_a\Gamma_b}{(E_r-E)^2+\Gamma^2/4} \tag{2.7}$$

If we define the following quantities:

$$\omega = \frac{(2J+1)(1+\delta_{aA})}{(2J_a+1)(2J_A+1)} \tag{2.8}$$

$$\gamma = \frac{\Gamma_a\Gamma_b}{\Gamma} = \frac{\hbar}{\tau}B_aB_b \tag{2.9}$$

where Γ_a and Γ_b are partial widths for exit channels a and b, respectively, τ is the lifetime of the compound state and B_a and B_b are the branching ratios for exit channels a and b, respectively, then the reaction rate for a single resonance can be written as:

$$\langle\sigma v\rangle = \left(\frac{2\pi}{m_{aA}kT}\right)^{3/2}\hbar^2e^{-E_r/kT}\omega\gamma \tag{2.10}$$

where $\omega\gamma$ is referred to as the resonance strength and E_r is the resonance energy. In cases where multiple resonances contribute to the reaction rate, these contributions are summed. For the reactions relevant to the present work, resonant capture dominates the reaction rates. The relevant energies can be seen diagrammatically in Figure 2.3.
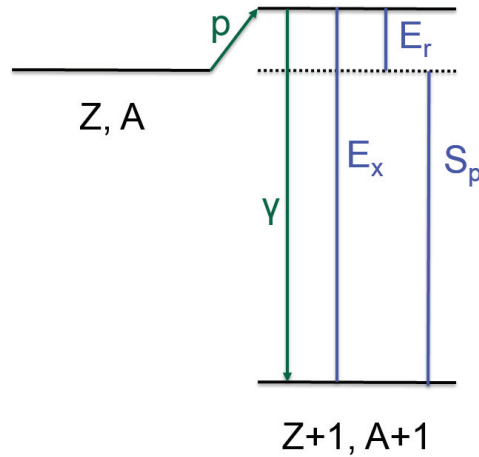
Figure 2.3 Diagram of energetics for capture of a proton capture with center of mass energy E_r onto a nucleus with Z protons and A-Z neutrons.

2.2 Methods for determining resonant capture reaction rates

There are several methods for determining these resonant capture reaction rates. In this section two theoretical methods and two experimental methods will be outlined below.

2.2.1 Hauser-Feshbach formalism

The derivation for this theoretical mod here follows [22], and is applicable when there are many resonances that contribute to the overall reaction rate. To obtain an energy averaged cross section in an interval I, with many narrow resonances, with spacing D, one can write the average cross section as:

$$\langle \sigma(E) \rangle = \frac{1}{I} \int_{E-I/2}^{E+I/2} \sum_p \sigma_p(E) dE \tag{2.11}$$

This expression can be rearranged as follows:

$$\langle \sigma(E) \rangle = \frac{1}{I} \sum_{p,E_p \in [E \pm \frac{I}{2}]} \int_0^\infty \sigma_p(E) dE = \frac{1}{I} \frac{I}{D} \int_0^\infty \sigma_p(E) dE \tag{2.12}$$

Using a Breit Wigner form for each resonance, as in Equation 2.7:

$$\langle \sigma(E) \rangle = \frac{\pi}{k^2} g_J \frac{2\pi}{D} \left\langle \frac{\Gamma_{\alpha p} \Gamma_{\alpha' p}}{\Gamma_p} \right\rangle = \frac{\pi}{k^2} g_J \frac{2\pi}{D} W_{\alpha \alpha'} \frac{\langle \Gamma_{\alpha p} \rangle \langle \Gamma_{\alpha' p} \rangle}{\langle \Gamma_p \rangle} \tag{2.13}$$

where $W_{\alpha\alpha'}$ is the width fluctuation factor, which accounts differences in the average of the whole width factor and the average of each individual width and $g_J = \frac{2J+1}{(2J_A+1)(2J_a+1)}$ is the spin statistical factor.

These average partial widths can be estimated by comparing to S matrix scattering cross sections, which can be calculated using the optical model. Here:

$$\sigma_\alpha(E) = \frac{\pi}{k^2} g_J \frac{2\pi}{D} \langle \Gamma_{\alpha p} \rangle \tag{2.14}$$

and the S matrix cross section can be written as:

$$\sigma_\alpha(E) = \frac{\pi}{k^2} g_J (1 - |\mathbf{S}_{\alpha\alpha}^{\mathrm{opt}}|^2) \tag{2.15}$$

Comparing these two equations, one can define a transmission coefficient:

$$(1 - |\mathbf{S}_{\alpha\alpha}^{\text{opt}}|^2) = \frac{2\pi}{D}\langle\Gamma_{\alpha p}\rangle = \mathscr{T}_\alpha \tag{2.16}$$

With these transmission coefficients, the averaged cross section can be rewritten as

$$\langle\sigma(E)\rangle = \frac{\pi}{k^2}g_J\frac{2\pi}{D}W_{\alpha\alpha'}\frac{\mathscr{T}_\alpha\mathscr{T}_{\alpha'}}{\sum_{\alpha''}\mathscr{T}_{\alpha''}} \tag{2.17}$$

When performing this averaging, one commonly used level density is a back-shifted Fermi gas model. The level density can be written as

$$\rho_{\text{bsfg}}(\varepsilon) = \frac{\sqrt{\pi}}{12a^{1/4}}\text{e}^{\left(\frac{2\sqrt{aU}}{U^{5/4}}\right)} \tag{2.18}$$

Here, instead of using the unshifted energy, an emprical shift is applied, where

$$U = \varepsilon - \Delta_{\text{bs}} \tag{2.19}$$

This backshift parameter Δ_{bs} is an empirical parameter related to pairing effects, which is used to replicate known odd-even effects in nuclei.

2.2.2 Shell Model

If the level density is not sufficient for the averaging needed in the Hauser-Feshbach calculations, another theoretical method for obtaining reaction rates is to calculate individual resonance properties using the nuclear shell model. Shell model calculations are performed by treating independently protons and neutrons in an average potential. This produces a shell structure analagous to electrons shells in noble gases for separately protons and neutrons. One downfall of this method is that the excitation energy uncertainties in shell model are often large. Since the reaction rate depends exponentially on the resonance energy, this translates to large uncertainties in the reaction rate.

2.2.3 Direct measurements

Ideally, the reaction rate can be directly measured experimentally, by measuring the cross section for the relevant resonance energies. These measurements, however are often not straightforward. These measurements suffer from low cross sections, which lead to low count rates. Many of the reactions take place on unstable nuclei. If the heavy nucleus is unstable, the measurement must then be done in inverse kinematics, and beam production rates tend to be low. A high resolution mass separator is also then required to separate the reaction products from the unreacted beam, which are very similar in mass.

2.2.4 Indirect measurements

If a direct measurement of the reaction rate is not feasible, or to guide rate estimates if the direct measurement is feasible, individual resonance properties can be measured and the reaction rate can be determined using the formalism outlined in Section 2.1. Unfortunately, indirect determinations of the reaction rate require many experiments to determine the different resonance properties. One can also use a combination of experimental and theoretical methods, such as experimentally determing resonance energies and identifying those resonances with shell model states to determine the resonance strengths.

2.3 $^{30}\text{P}(p, \gamma)^{31}\text{S}$

This section presents classical nova observables that are impacted by the experimentally unknown $^{30}\text{P}(p, \gamma)^{31}\text{S}$ rate. An overview of the currently available experimental information is also given. An experimental $^{30}\text{P}(p, \gamma)^{31}\text{S}$ rate is necessary because the level density in the region of interest for relevant temperatures is not sufficiently high to warrant the use of a statistical model rate.

2.3.1 Nucleosynthetic bottleneck

^{30}P$(p, \gamma)^{31}$S is potentially a bottleneck to nucleosynthetic flow beyond $A = 30$. As seen in Figure 2.4, when nucleosynthesis reaches ^{30}P, the available options are to β^+ decay or proton capture, as seen in Figure 2.4. The β^+ decay half life of ^{30}P is long (2.5 min.) relative to the duration of the peak temperatures in classical nova, effectively closing this path. Therefore, the flow to higher masses is regulated by the ^{30}P$(p, \gamma)^{31}$S rate.
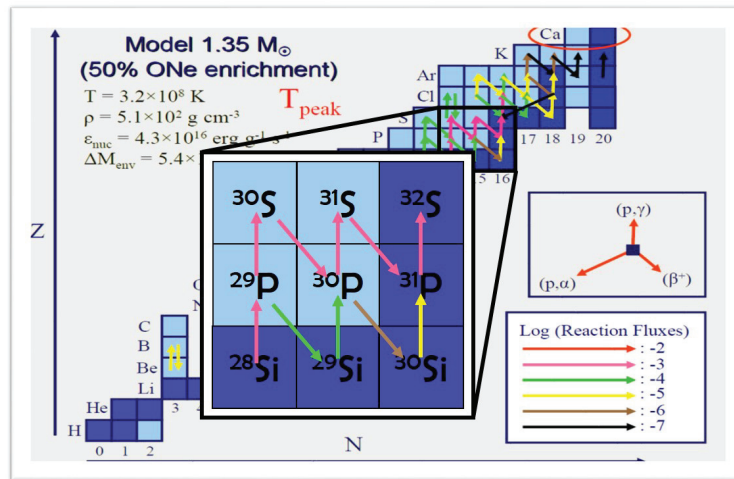
Figure 2.4 Classical nova nucleosynthesis path, zoomed in around ^{30}P. Figure adapted from [6].

2.3.2 Nova thermometers

Certain elemental ratios have been proposed as a way to determine the peak temperature of a classical nova. These ratios must vary monotonically with peak temperature, and ideally they would vary steeply with temperature. Downen *et al.* [7] have considered these ratios and these can be seen in Figure 2.5. Uncertainty in the ^{30}P$(p, \gamma)^{31}$S rate contributes the largest uncertainty in all of the ratios including S or P. Error bands for these ratios can be seen in Figure 2.6.

2.3.3 Si isotopic ratios

Silicon isotopic ratios have the potential to be used to identify presolar grains from classical novae, because the ^{30}Si/^{28}Si ratio is sensitive to the ^{30}P$(p, \gamma)^{31}$S reaction rate. With a fast ^{30}P$(p, \gamma)^{31}$S
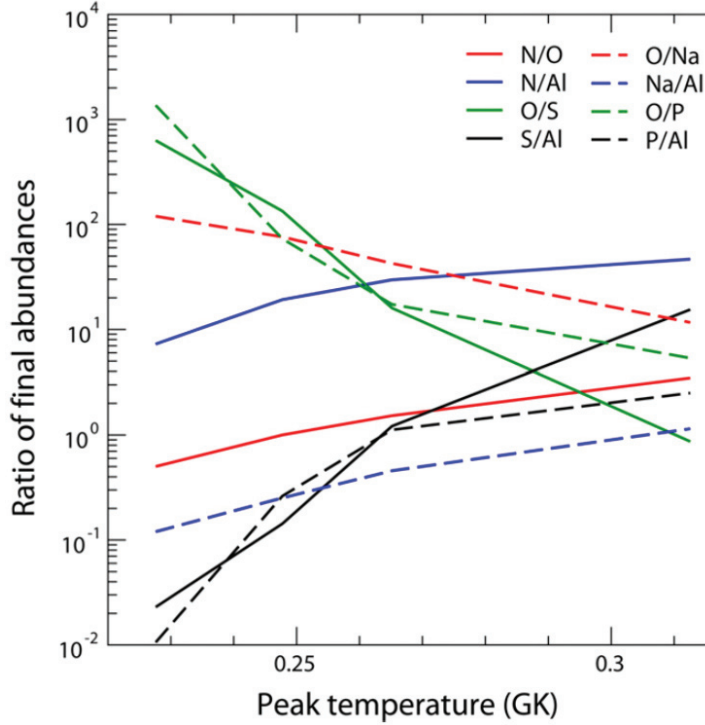
Figure 2.5 Elemental ratios proposed as nova thermometers. Figure from [7].

rate, little ^{30}P is left to β^+ decay to ^{30}Si. Qualitatively, high ^{30}Si/^{28}Si ratios are expected, but an experimental ^{30}P$(p, \gamma)^{31}$S reaction rate is needed to quantitatively constrain ^{30}Si production in novae. Measured Si isotopic ratios can be seen in Figure 2.7.

2.3.4 Current experimental information on ^{30}P$(p, \gamma)^{31}$S

Several experiments have already been performed in an attempt to work out the resonance energies and spins and parities of the relevant resonances, with $E_x \approx 6130 - 6700$ keV. Several techniques have been used to populate ^{31}S excited states. These techniques include single neutron transfer: ^{32}S$(p, d)^{31}$S [23, 24], ^{32}S$(d, t)^{31}$S [25, 26], ^{32}S$(^3$He$,\alpha)^{31}$S [27, 28, 29], in beam gamma spectroscopy: ^{12}C$(^{20}$Ne$, n\gamma)^{31}$S [30], ^{28}Si$(\alpha, n\gamma\gamma)^{31}$S [31], ^{24}Mg$(^{16}O,\alpha\alpha n\gamma)^{31}$S [32], and ^{16}O$(^{16}O, n\gamma)^{31}$S [33], other reactions such as ^{31}P$(^3$He$, t)^{31}$S [34, 35, 36], and ^{31}Cl β^+ decay [37, 38, 39].

While it is expected that most if not all of the states in the region of interest have been popu-
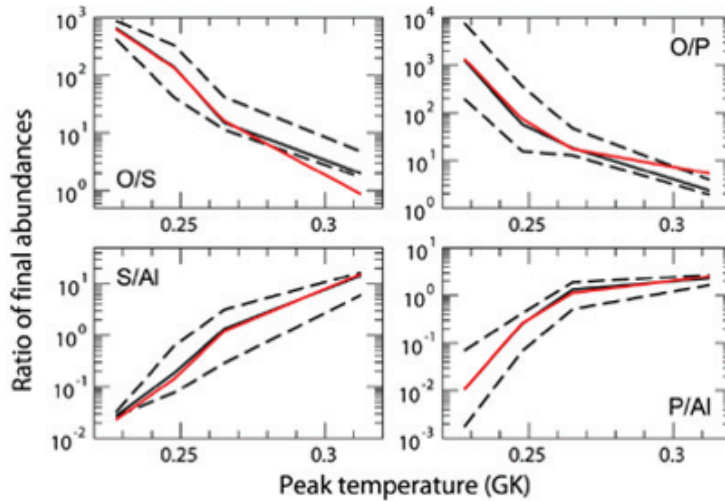
Figure 2.6 Error bands on predicted elemental ratios. The black line is the post processing prediction, and the dotted black lines show the uncertainties in the ratios. The uncertainties in these ratios are dominated by the uncertainty in the $^{30}P(p, \gamma)^{31}S$ rate. The predictions from full hydrodynamic calculations are shown in red. Figure from [7].
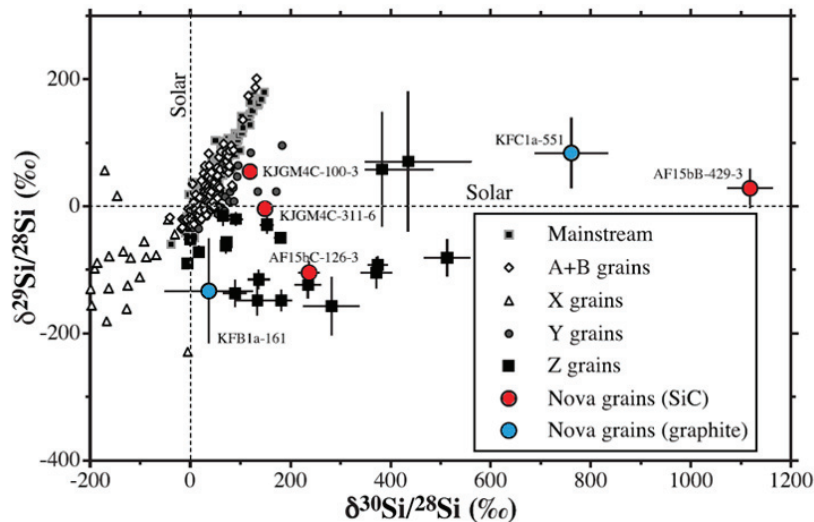
Figure 2.7 Measured silicon isotopic ratios in presolar grains. Nova grains are highlighted in blue and red. Figure adapted from [8].

lated, many of them have tentative or discrepant spin parity assignments. A partial level scheme, showing the region of interest, can be seen in Figure 2.8. None of the states of interest have known partial or total widths. Therefore, the resonance strengths are not yet known. These resonance strengths cannot currently be measured directly due to a lack of sufficiently intense ^{30}P beams at

the appropriate energy. Therefore, we must pursue indirect techniques. As a step toward determining these resonance strengths, this work outlines measurements that will constrain total widths of these resonances.
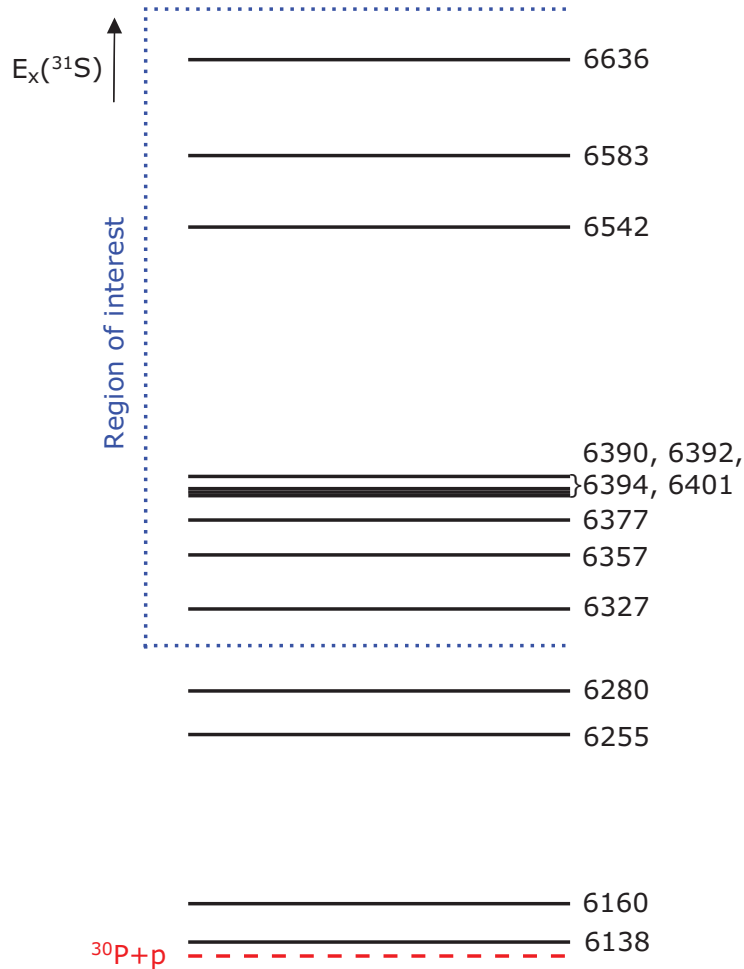
Figure 2.8 Current partial level scheme for ^{31}S. Data taken from [9].

2.4 ^{34g,m}Cl$(p, \gamma)^{35}$Ar

This section presents the structure of ^{34}Cl and ^{35}Ar and its impact on the ^{34g,m}Cl$(p, \gamma)^{35}$Ar rate as well as classical nova ^{34}S/^{32}S ratios, which are impacted by the currently experimentally unknown ^{34g,m}Cl$(p, \gamma)^{35}$Ar rate. An overview of the currently available experimental information is also given. An experimental ^{34g,m}Cl$(p, \gamma)^{35}$Ar rate is necessary because the level density in the region

of interest for relevant temperatures is not sufficiently high to warrant the use of a statistical model rate.

2.4.1 Isomeric state in ^{34}Cl

^{34}Cl has a low lying isomer ($E_x = 146.36(3)$ keV) with a half life of 32 min. in the laboratory. The ground state of ^{34}Cl has a shorter half life of 1.5 s, and due to the large angular momentum difference (3^+ for the isomer, and 0^+ for the ground state) transitions directly between these two states are highly suppressed. However, at stellar temperatures, higher lying excited states can be thermally excited. In particular, there are two 1^+ states at $E_x=461.00(4)$ and $665.56(4)$ keV that have decay branches to both the ground and isomeric states. This indirectly allows transitions between the ground state and isomeric state, effectively shortening the lifetime of the ^{34}Cl isomeric state. This effect on the ^{34m}Cl lifetime has been calculated in [10] and can be seen in Figure 2.9.
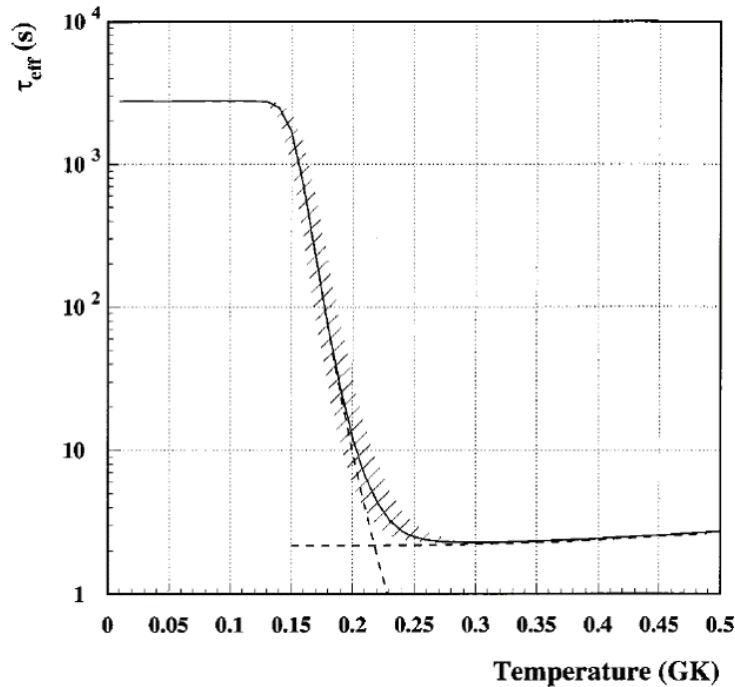
Figure 2.9 Lifetime of ^{34m}Cl as a function of temperature in an astrophysical plasma. Figure from [10].

However, the lifetimes of the β^+ decays of the ground state and the isomeric state are both

comparable to the proton capture lifetime. Therefore, the ^{34}Cl ground and isomeric states should potentially be considered separately, rather than as one total rate. Transitions between the ground and isomeric state also need to be considered.

2.4.2 Sulfur isotopic ratios

Given the current constraints on the relevant reaction rates, the currently measured isotopic ratios are insufficient to distinguish presolar grains from classical novae and type II supernovae. In both cases, low ^{14}N/^{15}N and ^{12}C/^{13}C ratios and high ^{30}Si/^{28}Si ratios are expected qualitatively. ^{34}S/^{32}S ratios have the potential to distinguish grains from these two origins. ^{32}S/^{33}S was proposed to distinguish grains of these origins, but [40] demonstrated that this ratio would not be distinct from the expected solar ratio. This same reference predicts a ^{32}S/^{34}S ratio of ≈ 100, which is distinct from both solar and type II supernova expected ratios.

However, the ^{34}S/^{32}S ratios are fairly sensitive to the currently experimentally unconstrained ^{34g,m}Cl$(p,\gamma)^{35}$Ar reaction rate. Once ^{34}Cl is reached in classical novae, it can either proton capture or β^+ decay, as seen in Figure 2.10. ^{34}Cl β^+ decays to ^{34}S, and if the ^{34g,m}Cl$(p,\gamma)^{35}$Ar reaction rate is fast, little ^{34}Cl remains, leading to less ^{34}S.
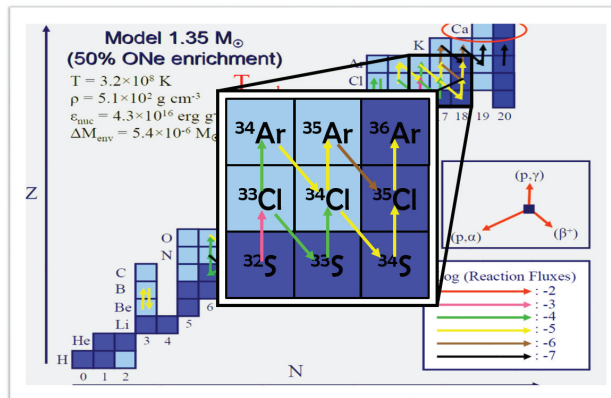
Figure 2.10 Classical nova nucleosynthesis path, zoomed in around ^{34}Cl. Figure adapted from [6].

Work is being done to measure sulfur isotopic ratios in presolar grains [41]. Contamination from the sulfuric acid used to separate the grains is an issue, but this is being overcome [42].

These ratios have not been measured yet in nova candidate grains.

2.4.3 Current experimental information on $^{34g,m}Cl(p,\gamma)^{35}Ar$

The Q value of this reaction is known to be 5896.3(8) keV for capture onto the ground state, and 6042.7(8) keV for capture onto the isomeric state. Prior to the work presented in this thesis, few levels just above the proton emission threshold were known and the known levels had an excitation energy uncertainty of 10-20 keV as seen in Figure 2.11. Since the reaction rate depends exponentially on the resonance energy, this contributes a large uncertainty to the reaction rate. The first measurements were performed by Kozub [23] and Johnson and Griffiths [43] just above the proton emission threshold, using the $^{36}Ar(p,d)^{35}Ar$ reaction, which lead to the discovery of three new levels with uncertainties of 20 keV. Betts *et al.* [44] then performed a measurement using $^{36}Ar(^{3}He,\alpha)^{35}Ar$, discovering two new levels and reducing the uncertainty on two of the known levels to 10 keV. In the thesis of Vouzoukas [45], another $^{36}Ar(^{3}He,\alpha)^{35}Ar$ was performed, discovering no new levels, but reducing uncertainties on 4 known levels. However, this work was never published in a refereed journal. This work presents an effort to search for new resonances and reduce uncertainties on the energies of known resonances.
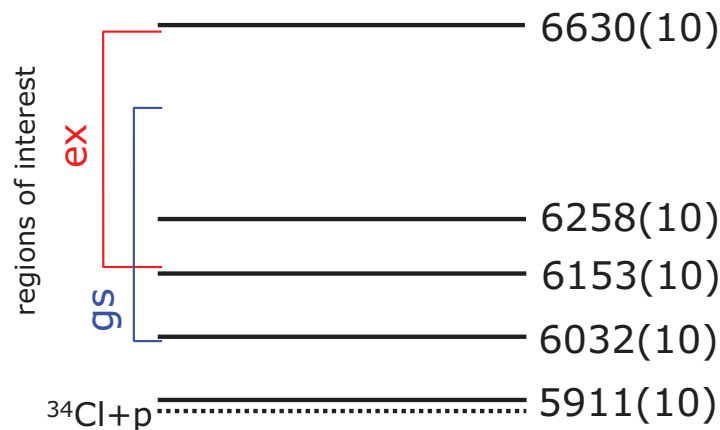
Figure 2.11 Previous partial level scheme for ^{35}Ar. Highlighted are the regions of interest for capture onto the ^{34}Cl ground and isomeric state. Data taken from [11].

CHAPTER 3

DOPPLER SHIFT ATTENUATION METHOD

In the Doppler Shift Attenuation Method (DSAM), a nucleus is populated in an excited state with a nuclear reaction. That excited state then slows down in a continuous medium. The amount of time that the excited nucleus spends traversing the stopping material before decaying by γ-ray emission is dependent on the lifetime of the state. Given the beam energy, target nuclei distribution, angular acceptances, and stopping powers in the medium, one can simulate γ ray energy lineshapes based on the expected Doppler shift for a range of possible excited state lifetimes. Comparing these lineshapes to data, excited state lifetimes can be extracted. A deeper discussion of the technique is given in this chapter.

3.1   Applicability of DSAM

Nuclear lifetimes range many orders of magnitude. Many different techniques are needed to cover this large range. Electronic timing can measure lifetimes down to nanoseconds, but resolution is insufficient to measure shorter lifetimes. Lifetimes down to a few picoseconds can be measured with methods where the recoiling nucleus recoils into vacuum, then into other discrete foils, where the lifetime is extracted by simulating relative populations of peaks Doppler shifted by different, discrete amounts. In the range ~ 3 fs $- 10$ ps, DSAM can be used to extract lifetimes that are too short for the recoil to leave a target, but still somewhat comparable to the slowing down time of the recoil in material. For excited states with lifetimes of $\sim$10 as-10 fs in states that emit protons, one can measure characteristic x-rays in coincidence with recoiling protons. One can compare the number of characteristic x-rays from the nucleus before and after proton emission, and use the ratio of x-ray integrals along with the characteristic time for x-ray emission of the nucleus to determine the lifetime of a proton emitting state.

3.2 Theory
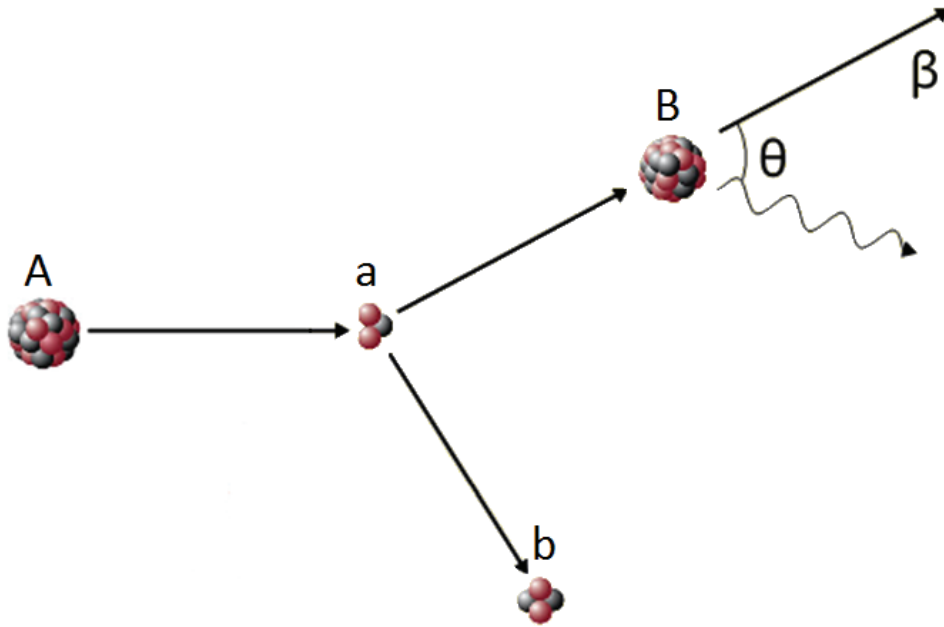
Figure 3.1 Diagram of a nuclear reaction. See text for details.

Here we consider a reaction A(a,b)B* as in Figure 3.1, where A and a are the projectile and target and b and B are the ejectile and excited recoil. For B* in vacuum, the speed v of a given atom is constant, and determined by reaction kinematics. The Doppler shift of the deexcitation γ-ray is then given by the formula:

$$E_\gamma = E_\gamma^0 \frac{\sqrt{1-\beta^2}}{1-\beta \cos\theta} \tag{3.1}$$

where $\beta = \frac{v}{c}$ and θ is the angle given by $\cos\theta = \frac{\tilde{\mathbf{v}}_r \cdot \tilde{\mathbf{p}}_\gamma}{v_r p_\gamma}$.

In DSAM, however, B* is created in a target and recoils within a stopping medium, making speed a function of time, giving

$$E_\gamma = E_\gamma^0 \frac{\sqrt{1-\beta^2(t)}}{1-\beta(t)\cos\theta} \tag{3.2}$$

Given the ability to calculate speed at a given time, the Doppler shifted γ-rays apparent in the lab frame are a measure of the decay time. To do this calculation, one needs stopping powers of the recoil within the stopping medium.

Nuclear excited state decays as a function of time follow an exponential decay law. The number of Doppler shifted γ rays emitted at each speed can be calculated.

$$N = N_0 e^{-t/\tau} \tag{3.3}$$

where N_0 is the number of initially populated excited states and τ is the lifetime.

3.2.1 Stopping powers

Ion energy loss in medium depends on the energy of the ion, the characteristic stopping power of the medium, and the density of the medium. High density solids have characteristic slowing down times of hundreds of femtoseconds. Targets for DSAM measurements are selected such that characteristic slowing down times are comparable to the lifetime of the excited state. This allows for measurements of lifetimes from a few fs to a few ps. If energy loss per distance is known, then change in velocity as a function of time is given by:

$$-M_r \frac{dv}{dt} = \frac{dE}{dx} \tag{3.4}$$

where M_r is the mass of the recoil with speed v at time t, and the stopping power is dE/dx.

Stopping powers are determined by two physical mechanisms, electronic and nuclear stopping. Electronic stopping is easily measured or calculated, and depends on long range electromagnetic interactions of electrons of the stopping atom with the moving ion. Nuclear stopping is due to inelastic collision between the moving ion and stopping atoms, and leads to large energy losses and large angular scattering, which is hard to measure.

In the low speed regime, $\beta \lesssim 0.5\%$, nuclear stopping dominates, so theoretical estimates must be used, due to difficulty in measurement, which leads to large uncertainties. In the medium speed regime, $0.5\% \lesssim \beta \lesssim 5\%$, nuclear and electronic stopping powers are of the same order, but measurements are feasible. For high speeds, $\beta \gtrsim 5\%$, electronic stopping powers dominate, and measurements tend to have lower uncertainties. In this regime, stopping power uncertainties contribute least to overall lifetime uncertainties.

Phenomenologically, as discussed in [46], stopping powers can be fitted with

$$\frac{1}{\rho}\frac{dE}{dx} = K_e\left(\frac{v}{v_0}\right) + K_n\left(\frac{v_0}{v}\right) \tag{3.5}$$

near $v_0 = \alpha c$, the Bohr speed, where α is the fine structure constant, $e^2/\hbar c$, ρ is the density of the stopping medium, and K_e and K_n are the electronic and nuclear stopping coefficients. K_e can be determined experimentally, then K_n is fit to data or calculations at lower speed.

Equations 3.4 and 3.5 can now be solved for $v(t)$. For the sake of simplicity in this derivation, we assume low recoil speeds, unidirectional recoils, and no large angle scattering. Other effects are included in the analysis, and will be discussed later in this chapter.

We first combine equations 3.4 and 3.5

$$\frac{dv}{dt} = -\frac{\rho}{M}\left[K_e\left(\frac{v}{v_0}\right) + K_n\left(\frac{v_0}{v}\right)\right] \tag{3.6}$$

and for convenience, we define

$$\omega = \frac{\rho K_e}{M v_0}. \tag{3.7}$$

Then, multiplying each side by v/v_0^2

$$\frac{d}{dt}\left(\frac{v}{v_0}\right)^2 = -\frac{2}{\omega}\left[\left(\frac{v}{v_0}\right)^2 + \frac{K_n}{K_e}\right] \tag{3.8}$$

and making a change of variables:

$$W = \left[\left(\frac{v}{v_0}\right)^2 + \frac{K_n}{K_e}\right]. \tag{3.9}$$

which gives:

$$\frac{dW}{dt} = -\frac{2}{\omega}W \tag{3.10}$$

and has the solution:

$$W(t) = \left[\left(\frac{v}{v_0}\right)^2 + \frac{K_n}{K_e}\right] = Ce^{-2t/\omega}. \tag{3.11}$$

To solve for C, we then impose the initial condition $v(t=0) = v_i$,

$$C = \left[\left(\frac{v_i}{v_0}\right)^2 + \frac{K_n}{K_e}\right] \tag{3.12}$$

and substitute this in for C, giving

$$\left[\left(\frac{v}{v_0}\right)^2 + \frac{K_n}{K_e}\right] = \left[\left(\frac{v_i}{v_0}\right)^2 + \frac{K_n}{K_e}\right] e^{-2t/\omega}. \tag{3.13}$$

We then make another change of variables, $V = \frac{v}{v_0}$

$$V^2 = \left[V_i^2 + \frac{K_n}{K_e}\right] e^{-2t/\omega} - \frac{K_n}{K_e}. \tag{3.14}$$

To compute dN/dV, we then need to solve for t and dt in terms of N and dN

$$t = \frac{\omega}{2} \ln \left[\frac{V^2 + K_n/K_e}{V_i^2 + K_n/K_e}\right]. \tag{3.15}$$

This applies until nuclei stop, at t_c such that $v(t_c) = 0$

$$t_c = \frac{\omega}{2} \left[\ln\left(V_i^2 + \frac{K_n}{K_e}\right)\right] + \ln\left(\frac{K_e}{K_n}\right) \tag{3.16}$$

Substituting in gives:

$$\frac{d}{dt}V^2 = \frac{-2}{\omega}\left[V_i^2 + \frac{K_n}{K_e}\right] e^{-2t/\omega} dt \tag{3.17}$$

dN/dt is given by an exponential decay law,

$$dN = \frac{N_0}{\tau} e^{-t/\tau} dt \tag{3.18}$$

rearranging gives:

$$dt = \frac{-\omega V}{V_i^2 + K_n/K_e} e^{2t/\omega} dV \tag{3.19}$$

and plugging this in gives:

$$\frac{dN}{dV} = \frac{N_0}{\tau}\left[\frac{V^2 + K_n/K_e}{V_i^2 + K_n/K_e}\right]^{\omega/2t} \frac{\omega V}{V^2 + K_n/K_e} \tag{3.20}$$

for all nuclei that decay before stopping. To account for the number of nuclei N_c that decay after t_c, a delta function must be added:

$$\frac{dN}{dV} = \frac{N_0}{\tau}\left[\frac{V^2 + K_n/K_e}{V_i^2 + K_n/K_e}\right]^{\omega/2t} \frac{\omega V}{V^2 + K_n/K_e} + N(t_c)\delta(V). \tag{3.21}$$

3.3 Lineshape analysis

While equation 3.21 gives us a lineshape under several simplifying assumptions, real experiments include broadening by several factors. Major factors are listed in the following paragraphs.

Kinematic broadening occurs due to an initial velocity distribution that will then be broadened by a range of Doppler shifts as well as a range of recoil angles. One way to reduce this is to limit the acceptance of the ejectile, which kinematically limits the accepted γ-ray angles.

Aberration occurs due to Doppler boosting. In the rest frame of the recoil, the solid angle subtended by the detector is larger than that of the lab frame. The relationship between the two angles is given by:

$$\cos \theta_{lab} = \frac{\cos \theta_{cm} + \beta}{1 + \beta \cos \theta_{cm}} \tag{3.22}$$

which is non-negligible for recoils with $\beta \gtrsim 5\%$.

At low speeds, dominated by nuclear stopping, ions will have large scattering angles. For lifetimes sufficiently long to reach these low speeds, there can be a large smearing of the angle of the recoils, which leads to a large range of Doppler shifts, in turn broadening the lineshape.

So far, we've assumed a point detector at $0°$. However, real detectors have finite size, therefore covering a larger spread in γ-ray angles. This broadening typically dominates the intrinsic detector resolution. One must also consider the efficiency as a function of angle. While this doesn't broaden the distribution, it does affect the lineshape.

γ-ray detectors also have an intrinsic energy resolution and lineshape. Ideal lineshapes must be convoluted with these intrinsic responses to produce accurate comparisons with experimental data. This lineshape is determined from fitting γ-ray lines from either radioactive sources or long lived states that have time to fully stop before decaying. This procedure is done for many γ-rays to determine the response as a function of energy.

Angular distributions may also be anisotropic, which would affect the lineshape. The recoil angular distribution will depend on the angular momentum transfer. γ-ray angular distributions are isotropic for spin 0 or 1/2 levels, but otherwise anisotropic. Both of these angular distributions can

be described by a sum of Legendre polynomials.

For low lying states, the excited state of interest can be populated either directly or by higher lying states. Population via higher lying states can artificially increase the extracted lifetime if not accounted for. In certain cases, this can be avoided by selecting beam energies such that population of higher lying states is negligible, or in cases such as this one, looking at states where higher lying states do not γ-decay, but decay through other channels, such as proton emission.

The discussion so far has assumed a beam without any spatial distribution. However, physical beams have some spatial extent. A large beam spot leads to a smearing in angle, leading to a larger range of Doppler shifts. Care should be taken to ensure a small beam spot for DSAM measurements. For a spot size of a few millimeters, however, the uncertainty due to the distribution of the beam will be negligible compared to other effects such as uncertainty in the stopping power.

All of these points must be considered, and included if applicable, when simulating lineshapes to extract lifetimes. For cases where the recoil velocity is sufficiently large to lead to a γ-ray distribution broader than the detector resolution, then lineshape analysis is appropriate.

3.4 Advantages of inverse kinematics

While DSAM can in principle be done in either normal or inverse kinematics, there are several advantages to inverse kinematics, where a heavy beam impinges on a light target, including:

- Recoils tend to be in the electronic stopping power regime. Electronic stopping powers are both more easily measured and have smaller angular scattering, leading to smaller uncertainties in the extracted lifetimes.

- Velocity change can be larger, due to a maximum in stopping powers for typical systems around recoil energies of tens of MeV for nuclei with mass number $A \approx 20 - 40$. This is particularly helpful for extracting finite lifetimes for short lived states.

- Higher recoil velocities lead to larger Doppler shifts, making it easier to distinguish unshifted peaks from shifted peaks, particularly at low energies, where the absolute shift is small.

CHAPTER 4

^{32}S(^{3}He,α)^{31}S EXPERIMENT

This chapter discusses the experimental equipment used in ^{32}S(^{3}He,α)^{31}S Doppler Shift Attenuation Method (DSAM) experiments. Two experimental runs were performed at TRIUMF. The first run suffered from large backgrounds, due largely to a beam delivery issue, caused by a quadrupole focusing magnet wired to have the wrong polarity by the TRIUMF operations group. Both runs used the same setup, save a few details discussed below.

4.1 Beam delivery

Before atoms can be accelerated, they need to be ionized. Stable beams at TRIUMF-ISAC are ionized using the Offline Ion Source (OLIS). OLIS uses multiple types of ionization techniques, depending on the ion of interest. Sulfur beams are delivered using the Multicharge Ion Source (MCIS) [47]. A magnet is then used to separate the various isotopes, in this case, selecting mass 32. Ions then enter the Radiofrequency Quadrupole (RFQ), which bunches the beam into packets separated in time by 85 ns and accelerates the beam.

A thin carbon foil is then used for charge stripping, here to the 7+ charge state. Further acceleration is then provided by a Drift-Tube Linac (DTL). This stage can accelerate ions from 150 keV/u to 1.9 MeV/u, and is the final acceleration stage for experiments in the ISAC-I hall. For experiments in the ISAC-II hall, such as this one, ions then enter the superconducting linac, which allows for beam energies ranging from 150 keV/u to 16.5 MeV/u (for A/q=2). In ISAC-II, typical beam characteristics include a 0.2% FWHM energy spread and 2 mm beam spot size. The layout of the lab can be seen in Figure 4.1.
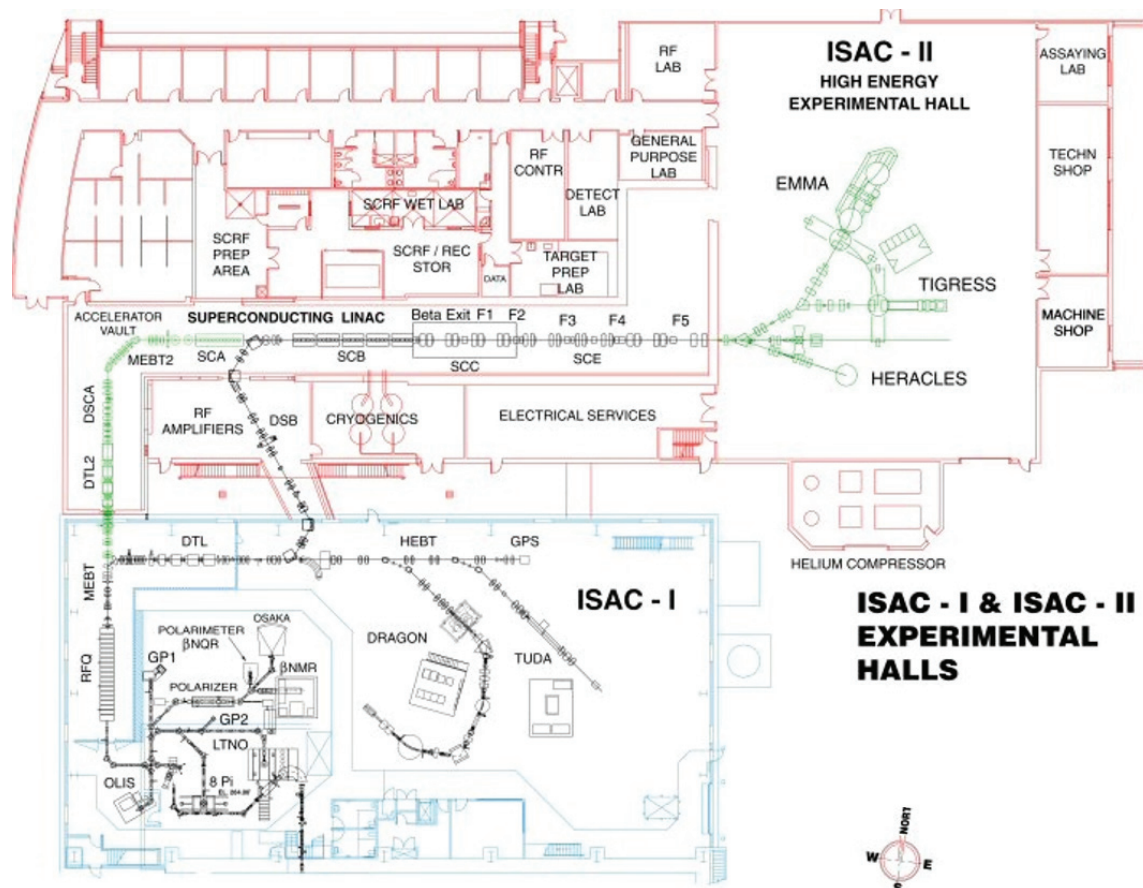
Figure 4.1 Layout of TRIUMF-ISAC facility.

4.2   Gold targets implanted with ^{3}He

A 25 μm× 2.5 cm × 2.5 cm Au target foil was implanted over a 2.85 cm^2 circular area with 35 keV ^{3}He ions using the ion implanter at McMaster University in Hamilton, ON, Canada for the first run. A density of 4×10^{17} ions/cm^2 was implanted into the foil. The foil thickness was selected to completely stop heavy reaction products and unreacted beam, while allowing for the light particles to propagate through to the ΔE-E Si telescope.

However, during the run at TRIUMF, this foil was found to be dirty, and the dirt was likely accumulated during the implantation process. For the second run, an identical gold foil was implanted at the University of Montreal, where foils for previous DSAM experiments have been cleanly implanted with an areal density of 6×10^{17} ions/cm^2.
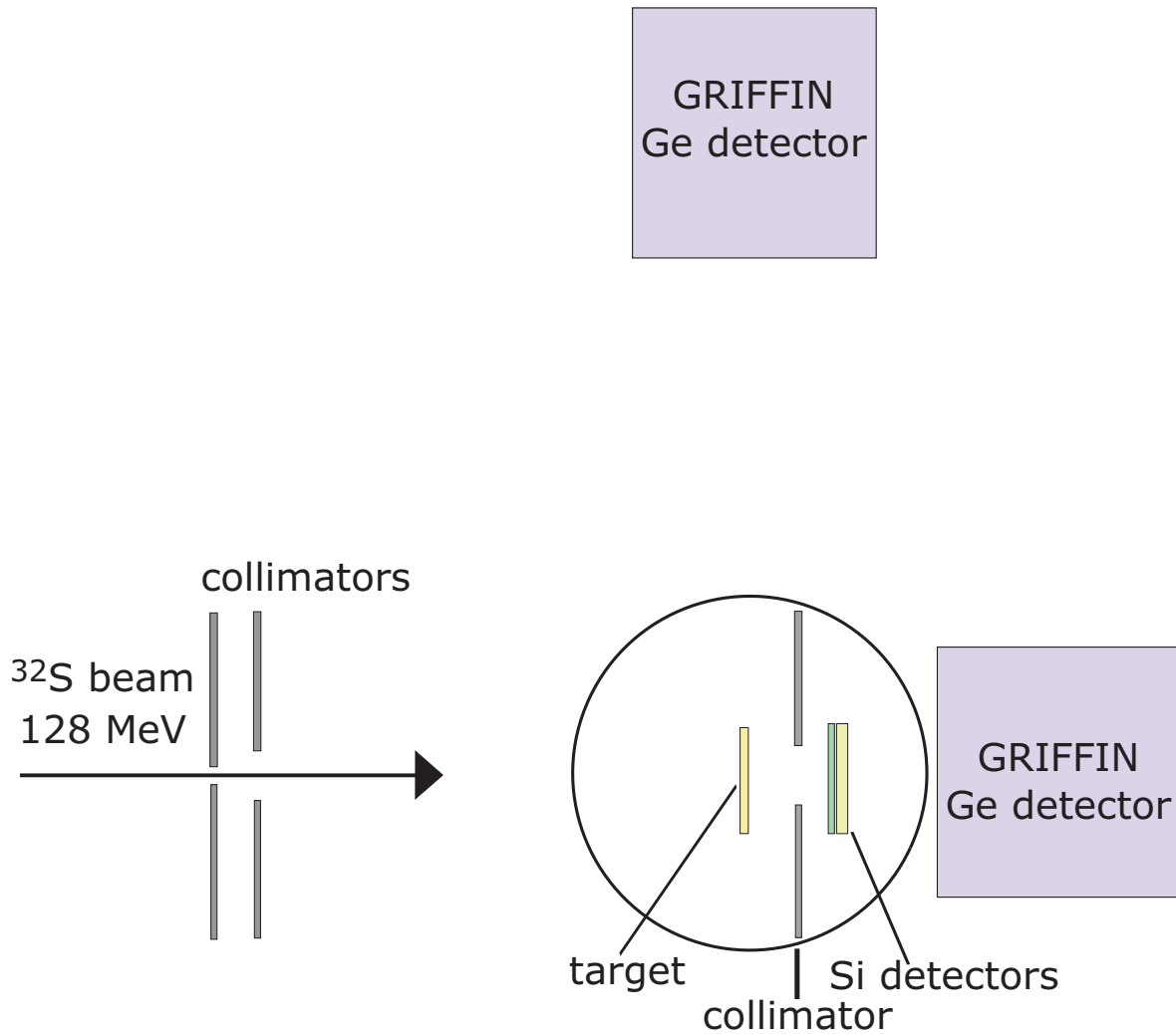
Figure 4.2 Schematic of the detector setup at TRIUMF. Detector sizes not to scale.

During Run 1, the loss of ^{3}He was monitored via the ratio of the ^{3}He elastic scattering rate to the beam current. The temperature of the foils is monitored via a PT-100 resistance thermometer. If these foils are heated, ^{3}He can potentially diffuse out of the foils, so the foils must be cooled. Temperatures of the target ladder and cold shroud throughout the run can be seen in Figure 4.3.
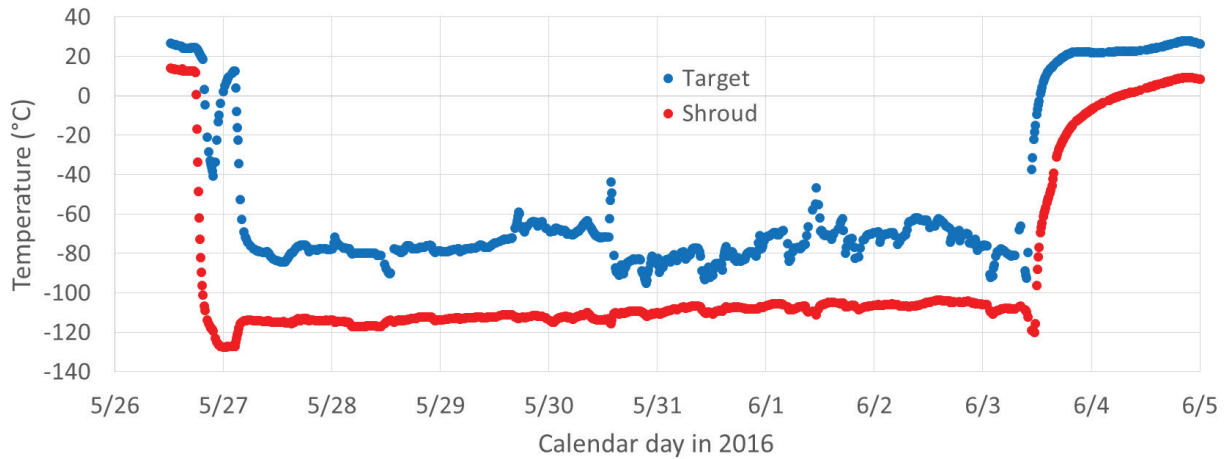
Figure 4.3 Graph of temperatures of the target ladder and cold shroud from Run 1, in 2016. Beam tuning on the target ladder began around midnight on May 27, where the ladder was not in thermal contact with the shroud. Subsequent temperature spikes correspond to short runs with the target ladder in the lowest target position, which had poor thermal contact with the shroud, due to bent BeCu springs. The dewar was last filled June 2, and after the beam was turned off on June 3, additional LN_2 in the dewar was blown out.

4.3 Target chamber

The Dopppler Shift Liftetimes (DSL) chamber at TRIUMF has been designed specifically for DSAM experiments. Drawings of the chamber can be seen in Figure 4.4. To further reduce potential contamination, an additional turbomolecular pump is also employed in the target chamber. This chamber allows for cooling of the target and a surrounding cold trap. The cold trap surrounds the beam with an LN_2 cooled copper shroud to reduce the condensation of carbon, water, and other contaminants onto the target. The LN_2 dewar used to cool the target was filled every 24 hours. With these measures, typical pressures in the DSL chamber during this experiment were between 9×10^{-8} and 3×10^{-7} torr.

Additionally, the target must be kept somewhat cool. However, to keep the target clean, it should remain warmer than the cold trap, as contaminants preferentially condense on the coldest surface. The target ladder is cooled via BeCu fingers in contact with a BN plate attached to the copper shroud. BN is a ceramic that acts as a good electrical insulator, and provides moderate thermal insulation. This keeps the target cool, but still warmer than the shroud. A photo of the
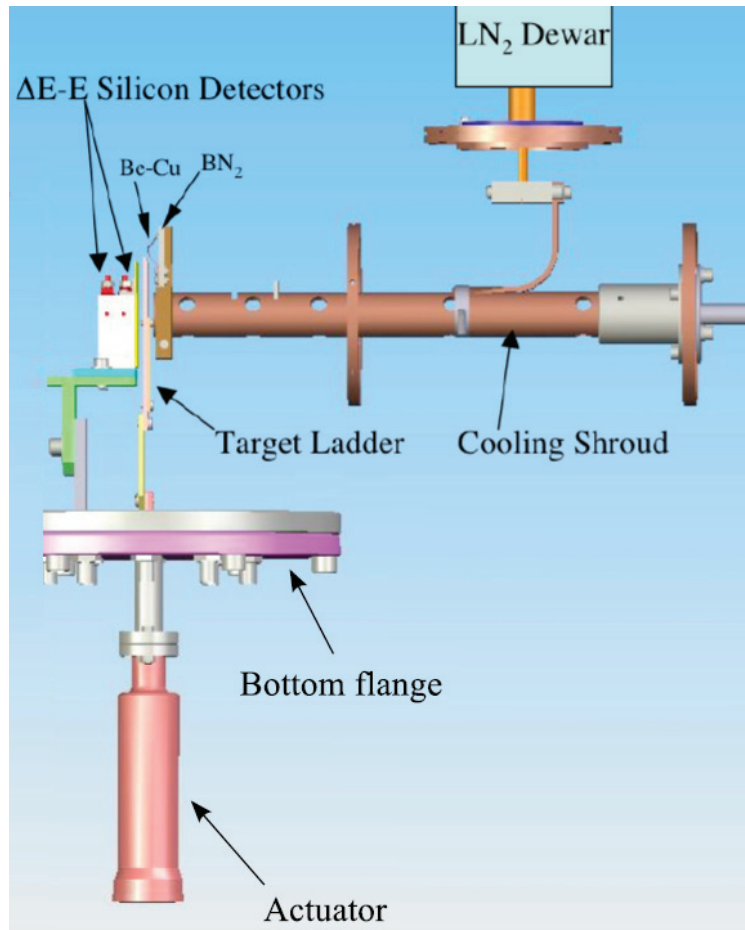
Figure 4.4 Drawing of the DSL chamber. The target and silicon detectors are located in the aluminum chamber, and a copper braid provides thermal contact to the LN_2 dewar.

ladder with targets from Run 1 can be seen in Figure 4.5.

The DSL chamber also contains two collimators, with diameters of 2.5 and 3.0 mm to ensure that the beam spot is well defined, as a large beam spot would lead to a large uncertainty in the reaction position, leading to poor lifetime sensitivity. The smaller collimator is placed further upstream, and the larger collimator is closer to the target, to clean up beam particles scattered off the first aperture. In the initial run at TRIUMF, these collimators were composed of copper. In conjunction with the poor beam tune, this lead to a large background in this run, which will be discussed further in the following chapter. To mitigate this background in the second run, tantalum collimators were used.

Electrical beam currents were read from the smaller, upstream collimator and the target ladder.
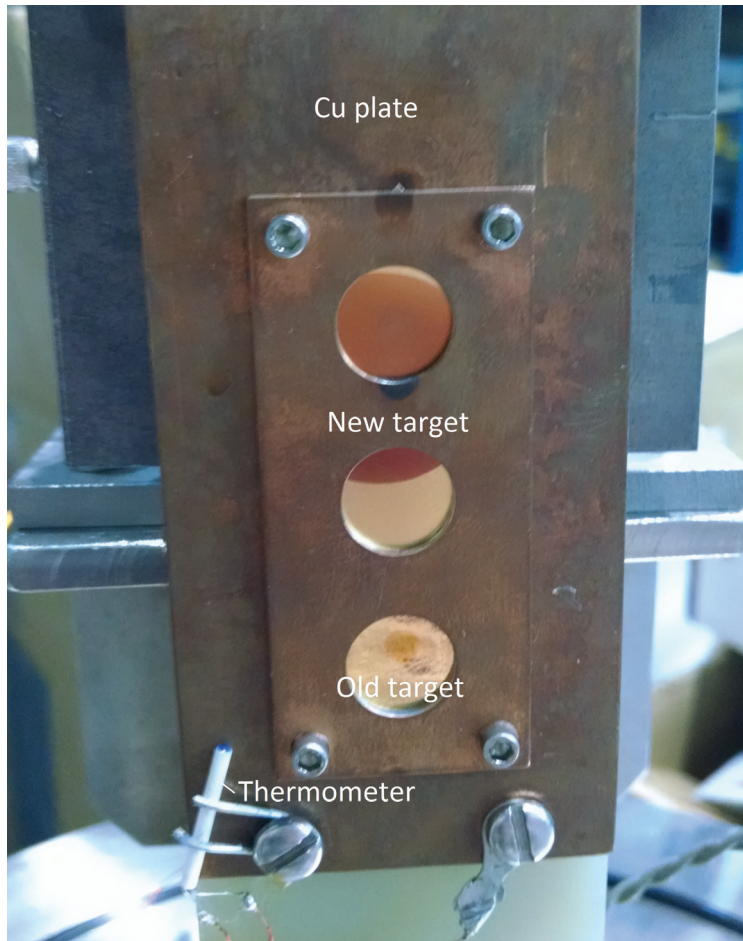
Figure 4.5 Photo of the target ladder immediately after the Run 1. Target temperature is monitored with the PT100 thermometer in the bottom left. The target implanted at McMaster filled the top two target positions, and an old target from [12] that is known to be dirty was placed in the bottom position.

These currents were used as beam tuning diagnostics. During tuning, currents on the collimator are minimized and currents on the target ladder are maximized. Early in the TRIUMF run, the beam is tuned with the target ladder in the lowest position, with beam hitting the copper plate. After we realized that we were activating the copper with the beam, all other tuning was done on the area of unimplanted gold in the second target position. An image of the collimator readouts and cooling can be seen in Figure 4.6.
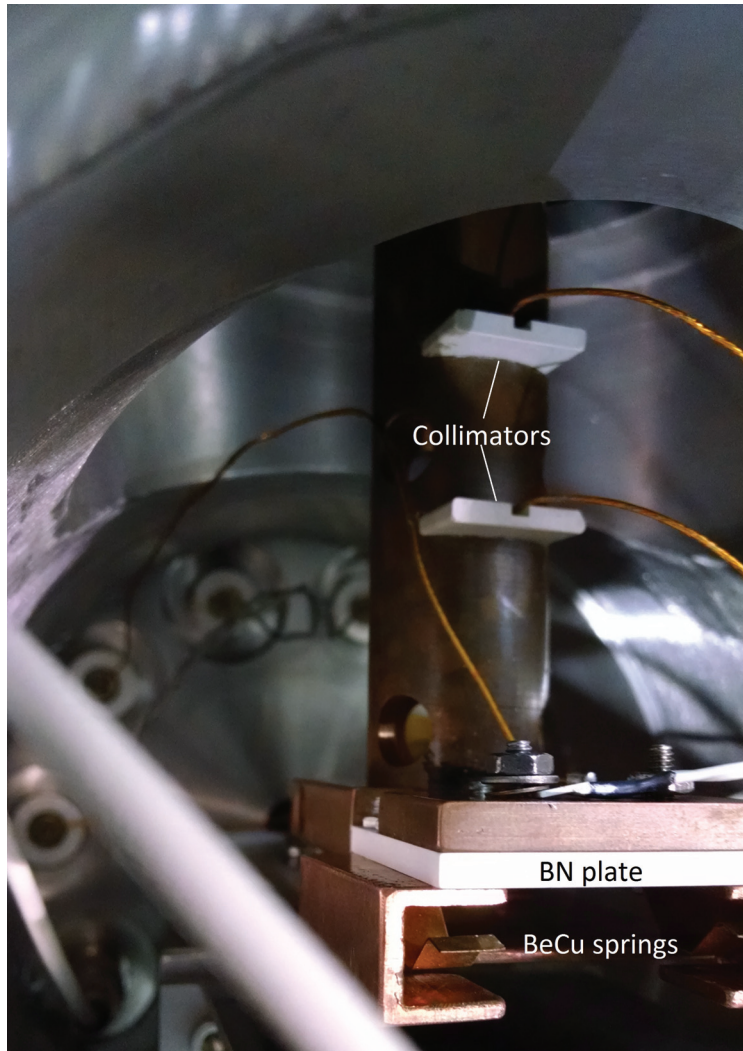
Figure 4.6 Photo of the collimators and cooling mechanism within the target chamber. The beam direction in this photo is from the top downward.

4.4 Detectors

This experiment uses two Ge clover detectors along with two Si detectors, which will be discussed in the following subsections. Additionally, this experiment used two PT100 thermometers to monitor the temperature of the copper shroud and the target ladder. These thermometers are platinum wires, and the resistance of these wires increases monotonically with rising temperature.

Both silicon and germanium are semiconductors. In all crystalline materials, the periodic lattice establishes allowed energy bands. In the lower band, or valence band, electrons are bound to

particular lattice sites. The conduction band is a higher lying band, in which electrons are free to move within the crystal. The gap between these bands is referred to as the bandgap. Metals are excellent conductors due to the fact that their valence band is not filled, and electrons can move within the valence band. For insulators, this bandgap is quite large, typically 5 eV or greater. Semiconductors are an intermediate case, with a smaller bandgap of roughly 1 eV.

Semiconductor detectors are operated with an applied bias voltage such that no charge is initially flowing, or "reverse-biased". When ionizing radiation passes through the biased semiconductor, electron-hole pairs are created and drifted in opposite directions, with the number of electron-hole pairs being proportional to the energy of the radiation. Without this bias, electron-hole pairs would equilibrate and recombine. Due to the small amount of energy needed to create an electron-hole pair ($\approx$3 eV) compared to other types of detectors such as gas filled detectors ($\approx$30 eV) a relatively better resolution can be obtained.

At $0°$, behind the target, two silicon detectors were placed on an aluminum stand inside the DSL chamber on a movable plate. This allows for $\Delta E - E$ particle identification, which will be discussed in the following chapter. Both detectors are Ortec B Series silicon surface barrier detectors with 150 mm^2 active area. For Run 1, the thin, or ΔE detector was 500 μm thick, and the thick, or E detector was 1000 μm thick. The α particles of interest lose roughly 50% of their energy in the ΔE detector and they are stopped in the E detector. A collimator was placed in front of the silicon detectors to avoid edge effects. A picture of the silicon detectors in the DSL chamber can be seen in Figure 4.7.

In both experiments, two high-purity germanium clover detectors were placed near the target, with one at $0°$, for maximal Doppler shift, and another at $90°$, for reference. Clover detectors consist of four germanium crystals, packed in a square configuration within a single cryostat. Due to the low bandgap in germanium, electron hole pairs can be generated thermally, which leads to leakage current and broadening of energy peaks. To combat this thermal noise, germanium detectors are operated at liquid nitrogen temperatures. The liquid nitrogen dewars in thermal contact are typically refilled every 8-12 hours. An image of the detector setup at TRIUMF is shown in Figure
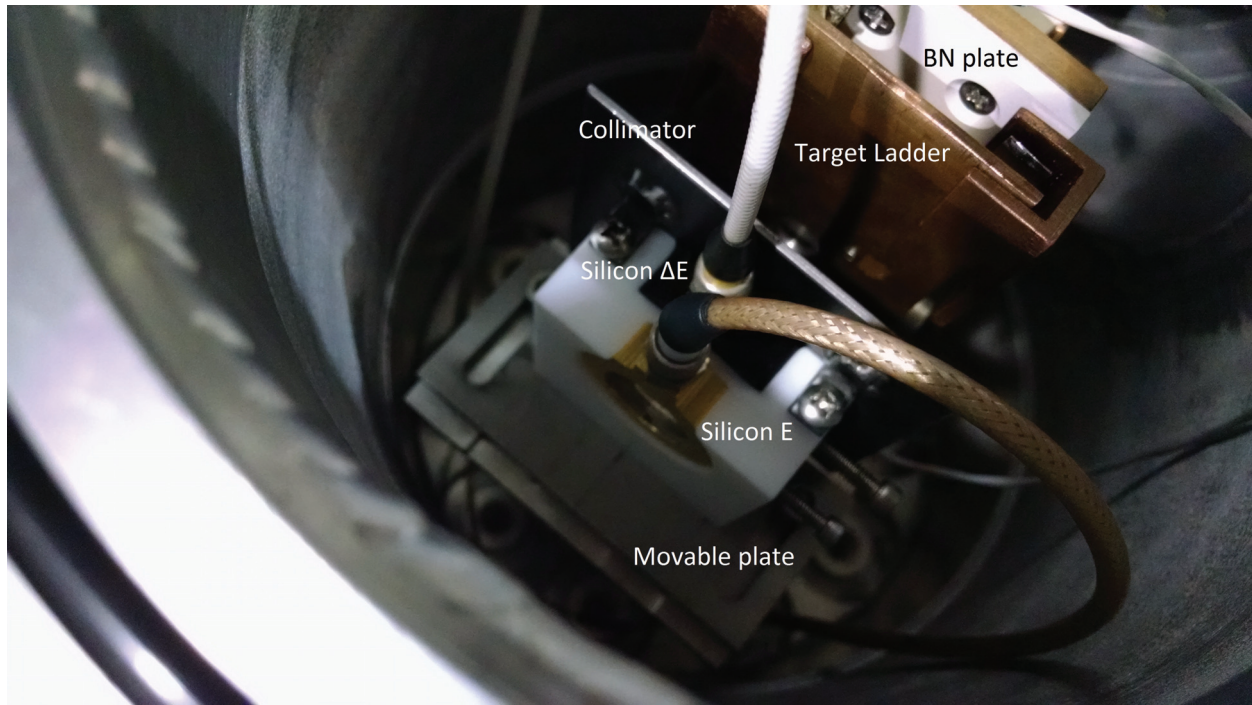
Figure 4.7 Photo of the target chamber with the silicon detectors and target ladder installed. The beam comes from the top right in this photo.

4.8.

While incoming charged particles directly create electron-hole pairs in the silicon detectors, γ-rays in germanium detectors interact in multiple ways. At energies below $\sim$200 keV, photoelectric absorption is most likely, where the photon is absorbed by a germanium atom, freeing an atomic electron. For energies $\sim$200-1200 keV, Compton scattering dominates, where the photon transfers some energy to an atomic electron. For energies above 1022 keV, twice the electron mass, pair production can occur. In pair production, a high energy photon near a nucleus can produce an electron-positron pair. When the positron annihilates with another electron, two 511 keV photons are produced.

There are a number of general characteristics in germanium detector response for a single γ-ray energy. I briefly cover these characteristics here, and more detail can be found in [48]. For high energy γ-rays, pair production is the most significant mechanism for energy deposition. If either the positron or electron escapes this leads to a peak at 511 keV below the full energy peak, referred
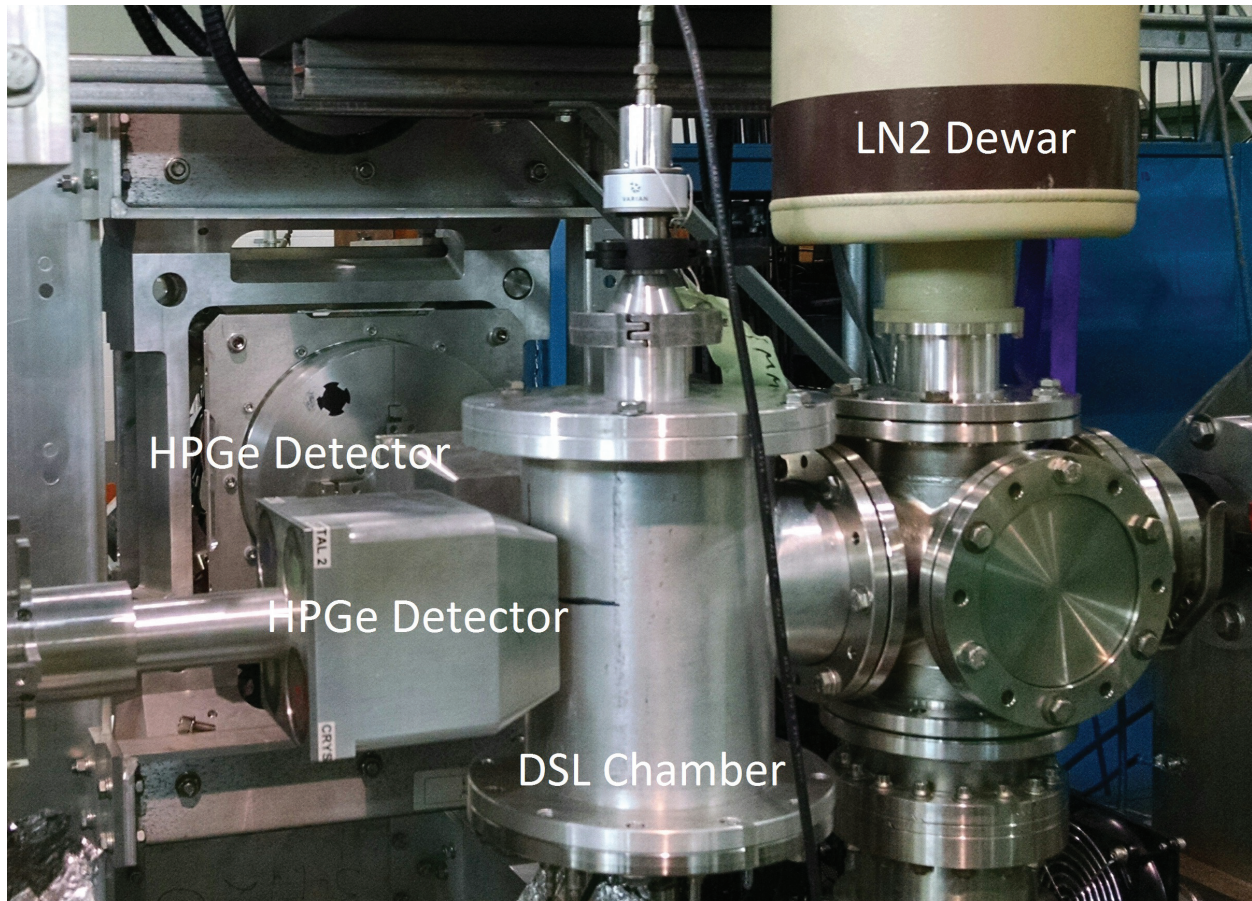
Figure 4.8 Picture of the detector setup at TRIUMF-ISAC II.

to as a single escape peak, and if both the electron and positron escape, this leads to a double escape peak, 1022 keV below the full energy peak. A broad peak typically exists around 0.2-0.25 MeV, caused by γ-rays that first Compton scatter on a material surrounding the detector, referred to as a backscatter peak. The Compton edge corresponds to the maximum amount of energy transferred in a single Compton scattering event.

4.5 Electronics

An electronics diagram for this experiment can be seen in Figure 4.10. Preamplifiers couple each detector with a high voltage power supply and readout electronics. The silicon detector preamplifiers were attached directly to the feed-through on the DSL chamber flange, to reduce the length
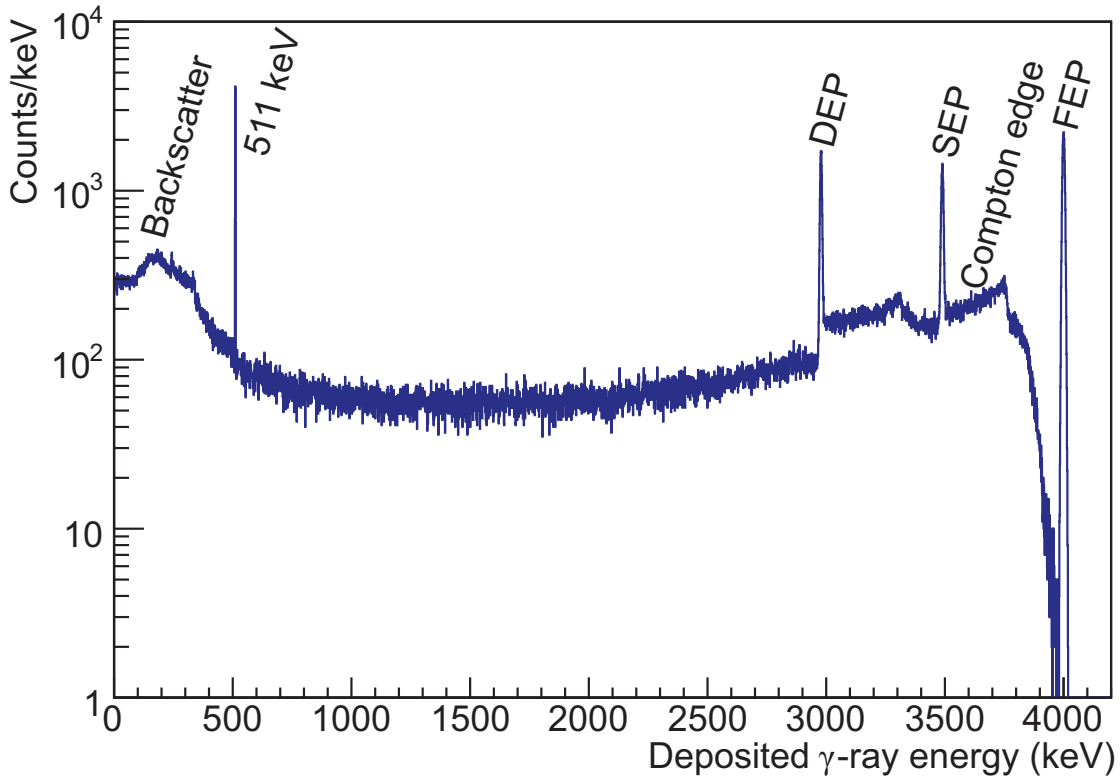
Figure 4.9 Simulated Ge detector spectrum for a monoenergetic 4000 keV γ-ray. FEP, SEP, and DEP correspond to the full energy peak, single escape peak, and double escape peak.

of cable available to pick up noise. To avoid RF noise, the DSL chamber, electronics racks, and detectors were grounded separately from the beamline.

Preamplifier signals from the two silicon detectors and eight germanium crystals were read into a single GRIF-16 card. These digitizers are 16-channel, 14-bit analog-to-digital converter (ADC) with a sampling rate of 100 MHz. The Maximum Integrated Data Acquisition System (MIDAS), developed at PSI and TRIUMF interfaces with the GRIF-16 digitizer to create a high-throughput system to write experimental data to disk. More information on the acquisition can be found in [49]. In the first run, the DAQ required 2 coincident events in the silicon detectors to write data to disk.
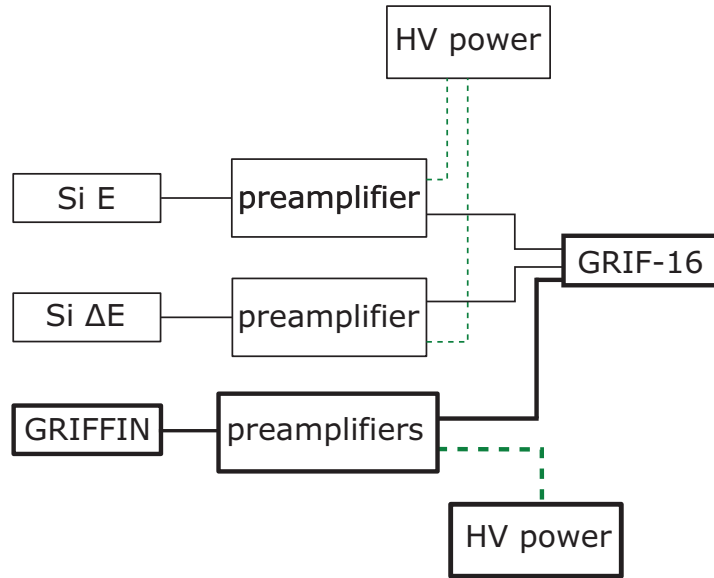
Figure 4.10 Block diagram of the data acquisition from Run 1. Bold lines signify multiple connections.

4.6 Run 2 experimental differences

The second run of this experiment was rather similar to the first one with a few small changes. Due to damage to the 500 μm ΔE detector was replaced with an 87 μm detector, which provides reasonable particle identification, but comes with the disadvantage of not completely stopping α particles with energies corresponding to direct population of the first excited state of ^{31}S. The Si detectors were also placed farther back from the target, decreasing the solid angle coverage, which improves energy resolution while decreasing count rate. As discussed previously, the upstream collimators were replaced with tantalum. Current monitors on the collimators were inadvertently disconnected. A cleaner target was fabricated at University de Montreal, where targets for previous DSAM experiments were performed. This run also used a triggerless DAQ and wrote all events above thresholds to disk.

CHAPTER 5

^{32}S(^{3}He,α)^{31}S ANALYSIS AND DISCUSSION

This chapter outlines the preliminary analysis of a two datasets from TRIUMF. While ^{31}S proton unbound state lifetimes could not be extracted from Run 1 data, useful insight on an improved second experiment was provided. Identification of background sources and methods to mitigate these backgrounds are provided. Reduction of background from Run 1 to Run 2 and tentative assignments for peaks in Run 2 will be briefly discussed.

5.1 Calibration

This section discusses the calibration of the silicon and germanium detectors both with radioactive sources and in situ data.

5.1.1 Silicon Detectors

The silicon detectors were calibrated before the run, using a triple-α source containing ^{239}Pu, ^{241}Am, and ^{244}Cm, with the strongest α branches of 5.155 MeV, 5.486 MeV, and 5.805 MeV respectively. This source was then affixed to the target ladder, without the BN plate or BeCu springs in place. Each detector was sufficiently thick to stop the α particles, so the thick E detector was calibrated before the thin ΔE detector was put in place.

An uncalibrated energy spectrum of one of these triple-α source runs can be seen in Figure 5.1. During these runs, the resolution for each silicon detector was detemerined to be 0.8%. A linear calibration was applied and used to extrapolate to higher energies. The extrapolation was verified by comparing beam-on data to SRIM calculations. The calibration of these detectors could then be used for particle identification and applying particle energy gates, to impose restrictions on the initial excitation energy in the nucleus of interest.
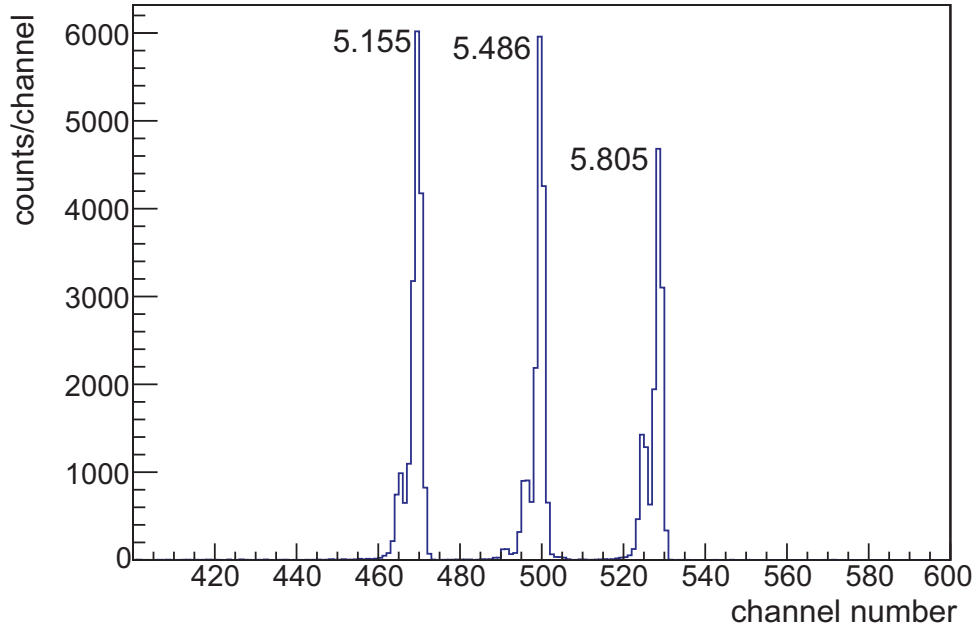
Figure 5.1 Uncalibrated α energy spectrum taken with a triple-α source at the target position with the thick silicon detector (thin detector removed). The energies of the three peaks used for calibration are labeled.

5.1.2 Germanium Detectors

Before this experiment, data were taken with a ^{56}Co source, which was used for the initial calibration. This source provides γ-rays up to 3.6 MeV, and the calibration was linearly extrapolated to higher energies and confirmed using the 6129 keV γ-ray from ^{16}O background. This calibration was sufficient for monitoring online data, which was confirmed using stopped γ-ray lines at 547 keV from Coulomb excitation, as well as a number of lines in ^{39}K, including those at 2814 and 3597 keV.

Temperature fluctuations between day and night time lead to daily drifts in the gain corresponding to 4-5 keV near E_γ=3.5 MeV. To correct for this temperature fluctuation, a run-by-run calibration was performed. The initial calibration was used to identify strong, narrow lines (not Doppler shifted), which could then be used in the run-by-run calibration. A linear calibration was applied using a line from ^{197}Au Coulomb excitation at E_γ=279.00(5) keV and a line from ^{39}K produced in ^{32}S+^{12}C fusion evaporation at E_γ=2814.06(20) keV. This calibration was then confirmed

44

at the end of the run using well known lines from ^{90}Nb β-decay from collimator activation.

5.2 Run 1 analysis

This section discusses analysis of Run 1 data, including a discussion of major background sources and potential methods to mitigate those backgrounds.

5.2.1 Particle identification

Particle identification (PID) was performed by gating on a $\Delta E - E$ plot. ΔE was measured by a silicon detector that is sufficiently thin that the particle deposits some, but not all of its energy, and then the remaining energy is measured in a thick silicon detector. This energy loss gives us information about the charge of the incoming nucleus. The stopping power, dE/dx, can be described using the Bethe formula given below

$$-\frac{dE}{dx} = \frac{4\pi e^4 Z^2}{m_e v^2} NB \tag{5.1}$$

where

$$B \equiv z \left[\ln \frac{2m_e v^2}{I} - \ln \left(1 - \frac{v^2}{c^2} \right) - \frac{v^2}{c^2} \right] \tag{5.2}$$

and v, Ze, z, N, and m_e are the velocity and charge of the incoming charged particle, the atomic number and number density of the absorber atoms, and the electron mass, respectively. I is a parameter related to the mean excitation and ionization potential of the absorber that is typically determined experimentally. For particles passing through the same amount of silicon, Δx, the energy loss is $\Delta E \propto \frac{Z^2}{v^2}$. Multiplying by $E = \frac{1}{2}Mv^2$, gives

$$\Delta E \times E \propto M \times Z^2 \tag{5.3}$$

Then a $\Delta E - E$ plot should show hyperbolic curves for each particle group corresponding to different values of MZ^2. The PID plot for Run 1 can be seen in Figure 5.2.
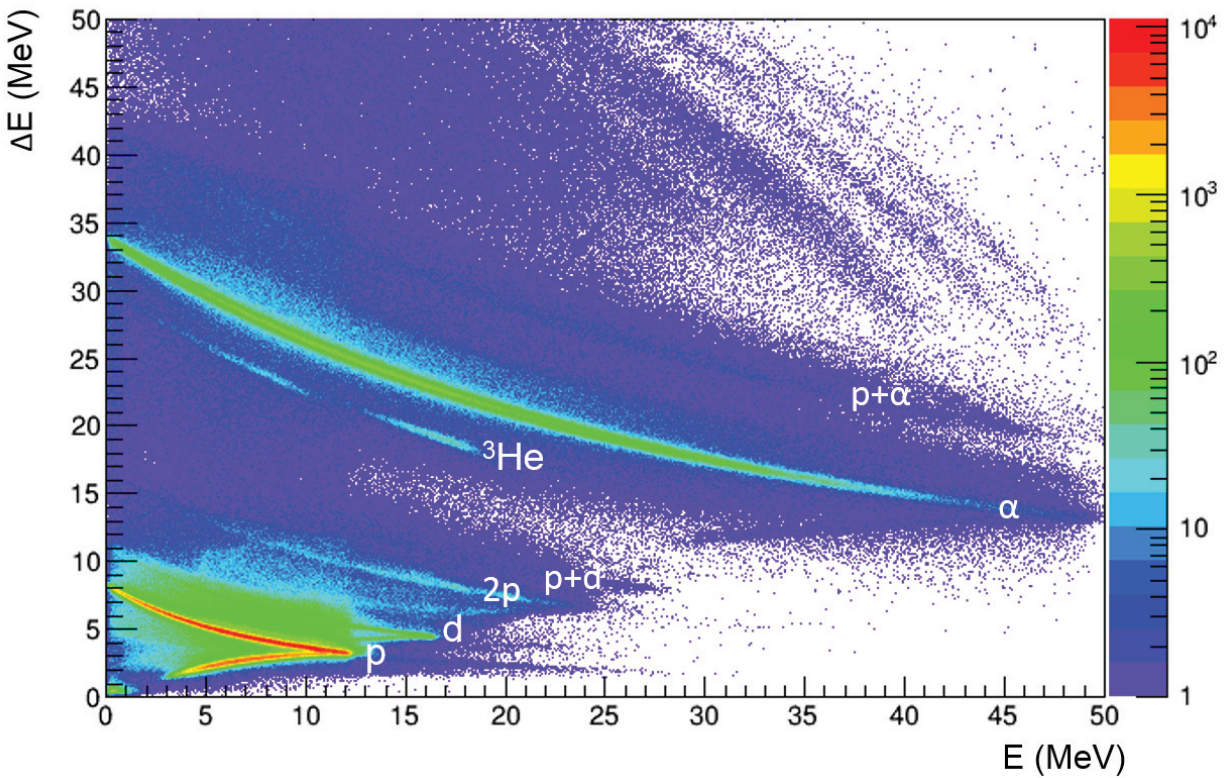
Figure 5.2 Particle identification plot for Run 1.

5.2.2 γ-ray identification

As there were many sources of background in this experiment, many different techniques were used to try to identify the source of the various γ-rays. Initially, we considered for each transition, the integral in the α-gated γ spectrum compared the integral in the proton-gated γ spectrum. If a peak was visible in the α-gated spectrum, but not (or very weakly) in the proton gated spectrum, we assumed that the event came from a channel that did not produce protons (neutrons could still be emitted and would not be detected), and occurred at the target position, so that the α particles could reach the silicon detectors.

If a peak was observed both in the α and proton gated spectra, a ratio of the integrals of these peaks was taken. Ratios close to 1 correspond to events from reaction channels that emit one proton and one α-particle. Ratios of less than 0.1 α/proton were attributed to decay channels that did not produce α-particles, and that the α-gated events were false coincidences. A transition with a ratio

46

of around 0.19 was assigned to events that were false coincidences with other events, as this ratio corresponds to the ratio of the total number of α particle events over the number of total proton events.

For events that could not be identified using the technique above, the geometry of this setup was used to gain position information. Our $0°$ detector was placed at a distance of 7.5 cm from the target to the face of the detector. Due to space constraints, the $90°$ detector was placed at a distance of 21 cm. This lead to roughly an order of magnitude difference in geometrical efficiency for events that occured at the target position. However, the difference in the distance between the detectors and the upstream collimator was much more similar, leading to a difference in geometric efficiency of a factor of 2. Therefore, ratios of integrals between the various detectors provided information about the source position of these radiations. These provided some constraints on what reaction mechanisms are likely.

5.2.3 ^{31}S first excited state

Although this experiment suffered from high background, the first excited state of ^{31}S was clearly visible above background at 1249 keV. Even though transitions from higher lying states were obscured by background, we could gate on this γ-ray and look at the α energy spectrum, to get an idea of what ^{31}S excited states are feeding the first excited state. More energy goes into populating higher lying excited states, leading to lower α-particle energies. The γ-ray lineshape of the 1st excited state and 1st excited state gated α energy can be seen in Figure 5.3.

In Figure 5.3, we see the first excited state has a fairly weak direct population, that is well separated from higher lying excited states, as expected. Fortunately, roughly 50% of the α particles from ^{32}S(^{3}He,α)^{31}S correspond to feeding of states with E_x =5-7 MeV, corresponding to our states of interest. This feeding was used to make rate estimates for Run 2.
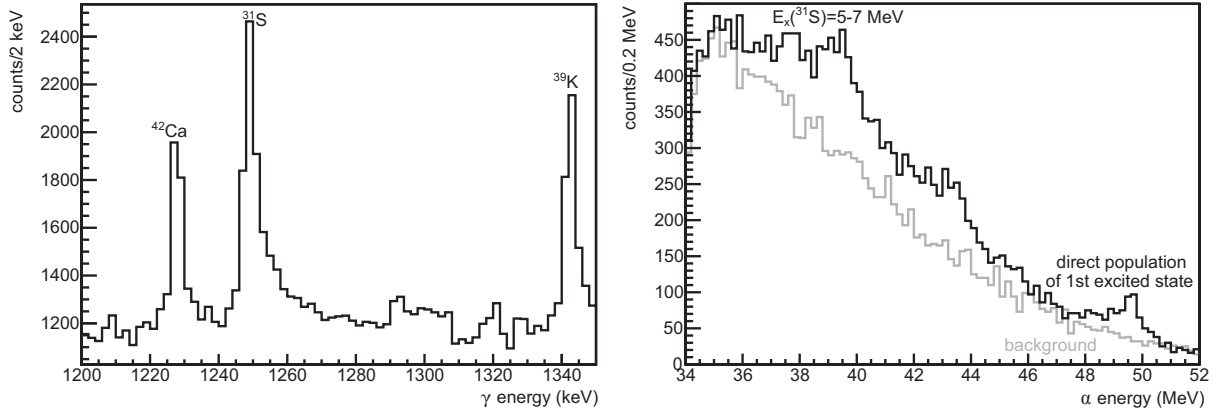
Figure 5.3 Left: α-gated γ spectrum zoomed in on the ^{31}S first excited state. Right: 1249 keV γ-ray energy gated α energy spectrum. The background in gray is taken by applying a gate on background γ rays with slightly lower energies.

5.2.4 ^{32}S first excited state

^{3}He inelastic scattering, populating the first excited state in ^{32}S provides a fairly high statistics, low background peak to test the validity of our lineshape simulation code. A fit of

5.2.5 Fusion evaporation reactions

The majority of the background in this experiment came from fusion-evaporation reactions. In these reactions, heavy nuclei collide, and fuse into a hot compound nucleus. These reactions tend to populate continuum states which emit, or evaporate, protons, neutrons, and α particles. All fusion evaporation calculations in this thesis used PACE4 [50], based on a modified JULIAN fusion evaporation Monte-Carlo code [51] included in the software package LISE++ [52].

This experiment suffered from the build up of a carbon layer on the surface of the target before or during implantation. The carbon compounds forming this layer turn orange under beam heating and can be seen in Figure 4.5, with the top two target positions holding the target implanted for this run, and the bottom position with a target that was cooled improperly in another experiment [12], which resulted in hydrocarbon condensation on the target.

Reactions on the carbon were particularly problematic: since they were on the surface of the
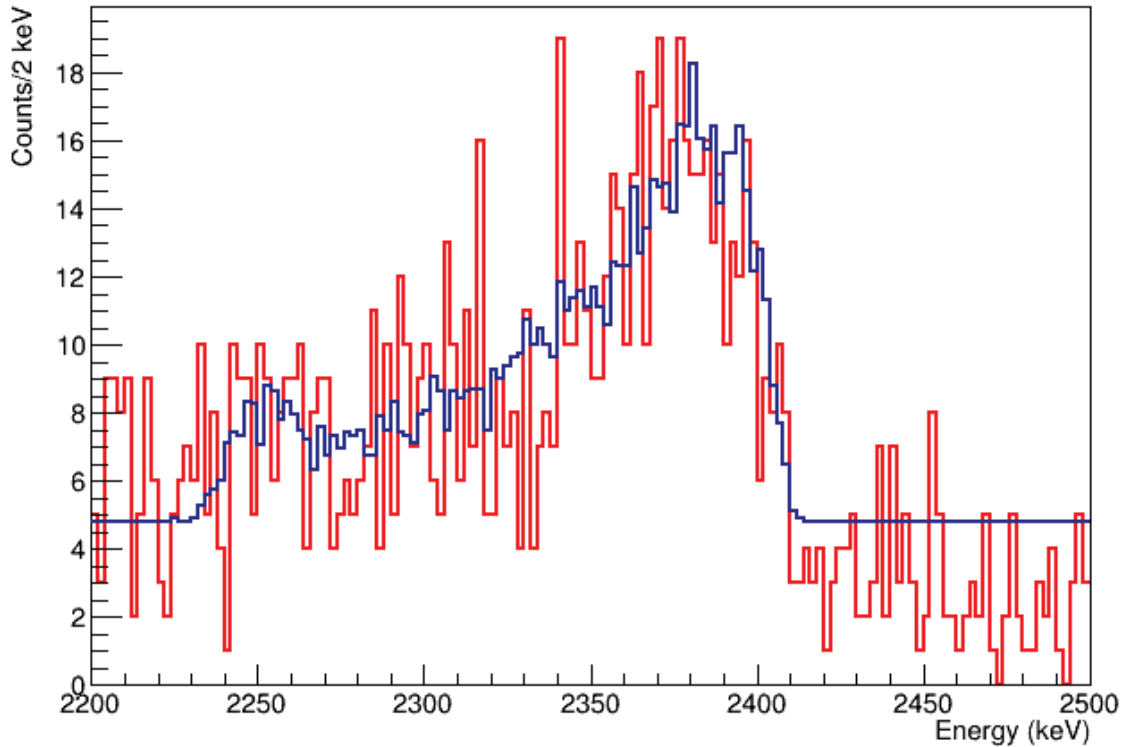
Figure 5.4 Data from ^{32}S(^{3}He,^{3}He')^{32}S* in red along with preliminary best fit lineshape and flat background in blue. The lifetime extracted from this fit, 240(30) fs agrees with the literature lifetime of 244(15) fs [13].

target, light reaction products could propagate to the silicon telescope, and could not be gated out. Not only did many channels produce α-particles, but the energy distribution of the α-particles from the carbon fusion-evaporation reactions was peaked at the region of interest for ^{32}S(^{3}He,α)^{31}S . An α-gated spectrum with peaks from ^{12}C+^{32}S reactions labeled can be seen in Figure 5.5.

By comparing to cross sections calculated with PACE4, as well as short runs with the dirty target from [12], we determined the areal density of the carbon to be roughly 3×10^{17} atoms/cm^2. This areal density is comparable to that of the implanted ^{3}He. Unfortunately, the cross section for α-particle producing events from ^{32}S+^{12}C is calculated by PACE4 to be roughly 800 millibarns, compared to the cross section for ^{32}S(^{3}He,α)^{31}S of only 95 mb calculated by PACE4.

In previous experiments, [53, 54] while some carbon contamination was present, levels of
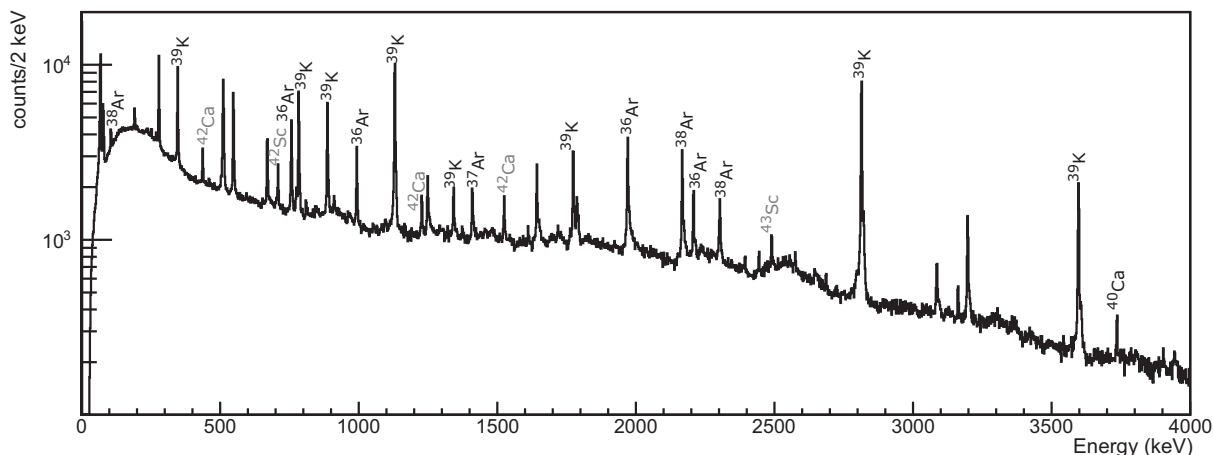
Figure 5.5 α-gated γ-ray spectrum with peaks from ^{12}C+^{32}S reactions labeled. Peaks with gray labels correspond to false coincidences with proton events.

contamination were 1-2 orders of magnitude lower. This level of carbon contamination would be manageable, and would not create much background in the region of interest. To mitigate this problem in Run 2, we have implanted a new foil at University de Montreal, where targets from previous experiments were successfully implanted.

Due to a poor beam tune, up to 80% of the beam was dumped on our copper collimators early on in the run, and even after spending extra time on an improved tune, typically half of the beam was lost on the collimator. The collimator essentially acted as a thick target, which combined with a cross section of roughly 800 mb at the full energy lead to a very high yield.

These reactions populate nuclei with Z≈39-44 and A≈85-94. These nuclei are sometimes populated in excited states, which lead to a few low energy γ-rays, which can be seen in Figure 5.6. If this were the only background from the copper, it would not have any significant impact on a successful analysis of this data set, due to the low γ-ray energies, below our region of interest. Unfortunately, these reactions also lead to a rather large continuum background. This effect has been seen before in a very similar system, ^{35}Cl+^{54}Fe at similar beam energy, in [55]. This continuum, seen in Figure 5.7, obscured the transitions of interest for this analysis.

To mitigate this background in any future experiments, new collimators were fabricated at TRIUMF for Run 2, using tantalum. Using a higher Z material leads to a larger Coulomb barrier.
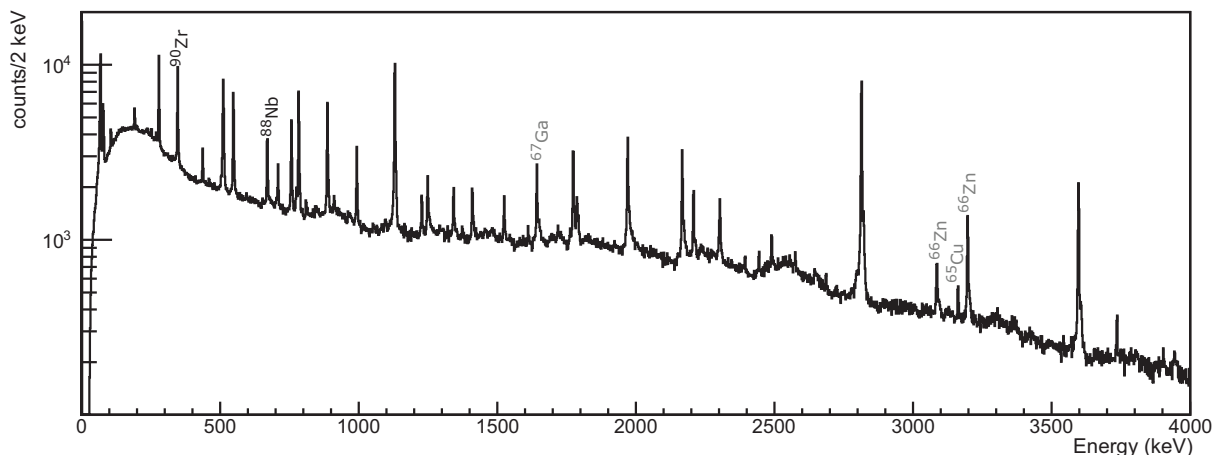
Figure 5.6 α-gated γ-ray spectrum with peaks from ^{63,65}Cu+^{32}S reactions labeled in black and ^{63,65}Cu+p,n,α reactions labeled in gray.
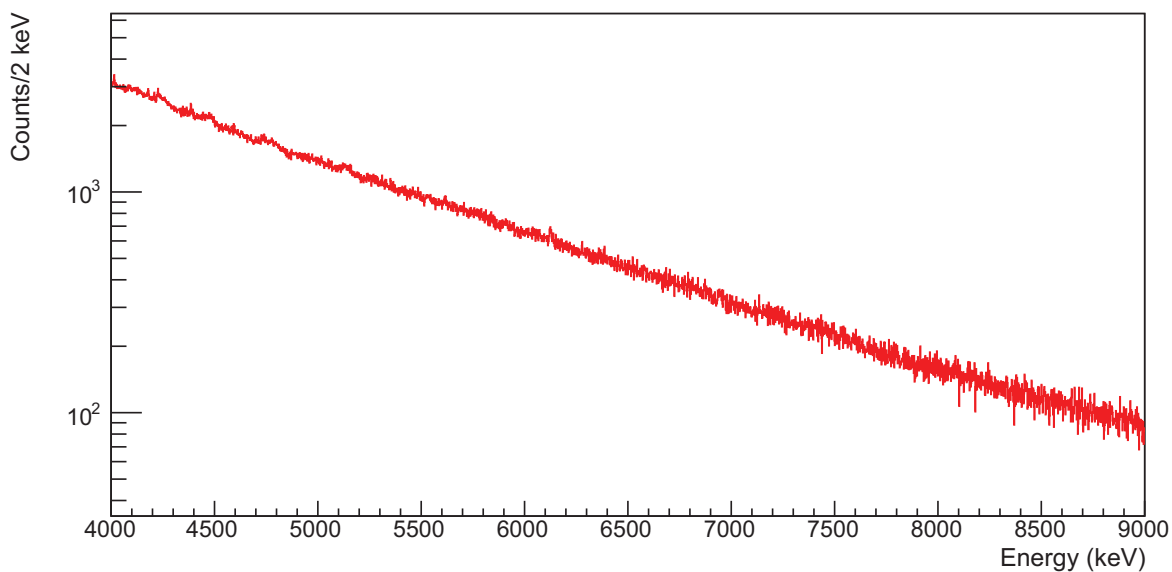
Figure 5.7 α-gated γ-ray spectrum showing continuum background at high energies from ^{63,65}Cu+^{32}S reactions.

Using the same beam energy as Run 1, we were below the Coulomb barrier for Run 2. The fusion evaporation cross section is then negligible, and the only concerns with tantalum collimators would then be Coulomb excitation of the tantalum and reactions on any contaminants in the tantalum. Tantalum Coulomb excitation has been well studied and will only give low energy γ-rays, below the region of interest. Contamination of the tantalum must be kept to a minimum, but with relatively

51

pure tantalum or a good beam tune, background from the collimator should be minimal.

In addition to γ-rays from the fusion-evaporation reactions, these reactions also produced large numbers of protons, neutrons, and α-particles. These light particles can then undergo reactions on the copper in the collimator. Photopeaks identified as coming from these reactions can be seen in Figure 5.6, labeled in gray. Replacing the collimators mitigates this background.

5.2.6 Collimator activation

Some of the isotopes produced by the reactions on the collimator have long half-lives, up to 107 days for ^{88}Y. β-delayed γ-rays were not time-correlated with the beam, and were effectively gated out of the on-line data. However, after the beam was turned off, these β-delayed γ-rays were counted for 8 hours, then briefly again after 2.5 days of calibration runs. The first 8 hours of data can be seen in Figure 5.8.
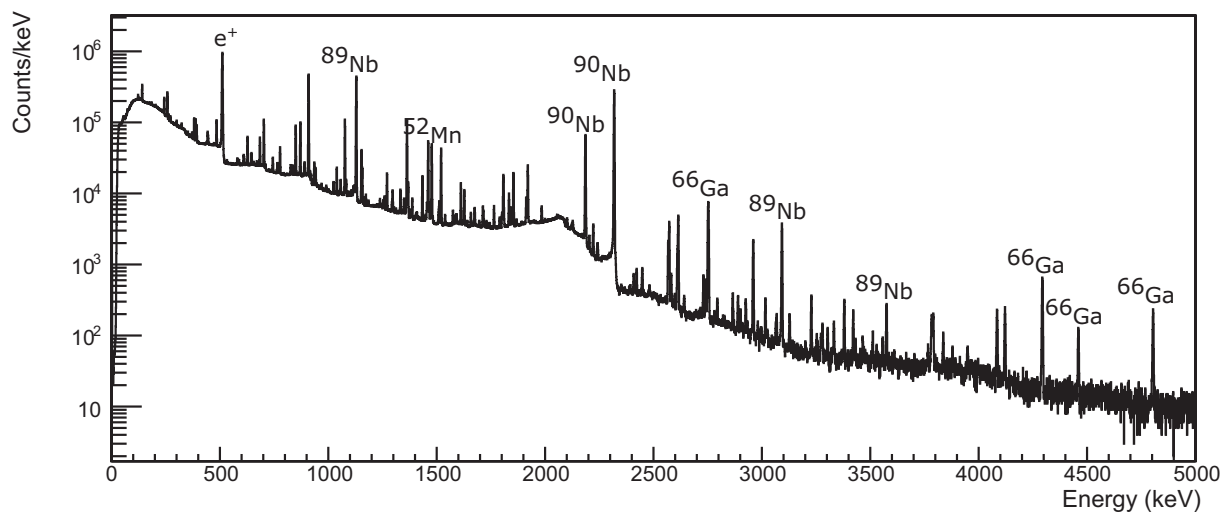
Figure 5.8 γ-ray spectrum showing β-delayed γ rays in the 8 hours immediately after the beam was turned off.

In the analysis of this spectrum, initial assignments were made using expected β-decay daughters of nuclei identified during the experiment, corresponding to fusion evaporation products. Identifying other lines in the spectrum lead to the realization that light particle induced reactions were

also occurring in the collimator.

5.3   Preliminary analysis of Run 2 data

A detailed analysis of Run 2 data is beyond the scope of this dissertation; however, preliminary results are discussed below. This data was calibrated using the same procedure as discussed above. Silicon detectors were calibrated with a triple α source, and germanium was calibrated run by run using the 247 keV γ-ray from ^{197}Au Coulomb excitation and the 2841 keV γ-ray from ^{32}S(^{12}C,$p\alpha$)^{39}K. Particle identification can be seen in Figure 5.9.
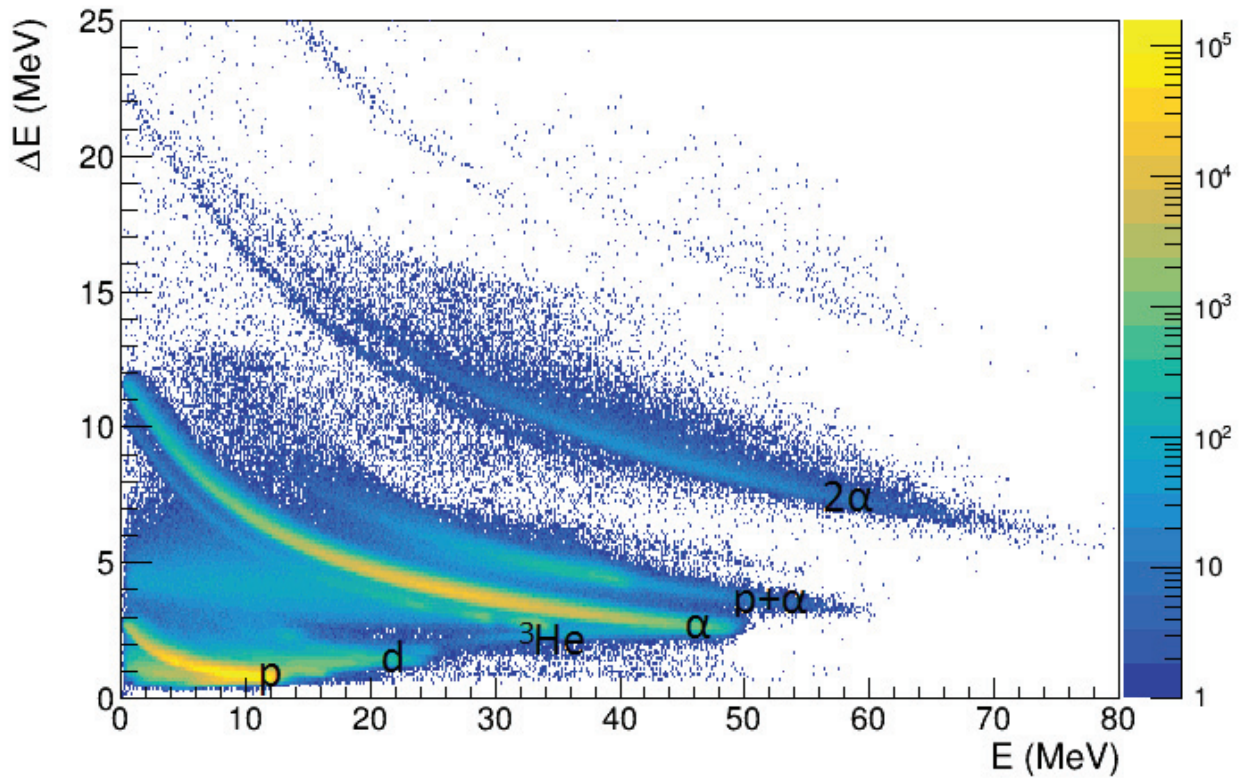
Figure 5.9 ΔE-E particle identification plot.

5.3.1 Background reduction

High energy γ-ray background obfuscated peaks of interest in Run 1 data. Figure 5.10 shows the reduction in background by reducing carbon contamination on the surface of the target as well as replacing copper collimators with new collimators. The background is reduced by roughly a factor of three in the region of interest. The major sources of remaining high energy γ-ray background are likely fusion evaporation reactions on dirt and ice on the surface of the target and fluorine contamination in the tantalum collimators.
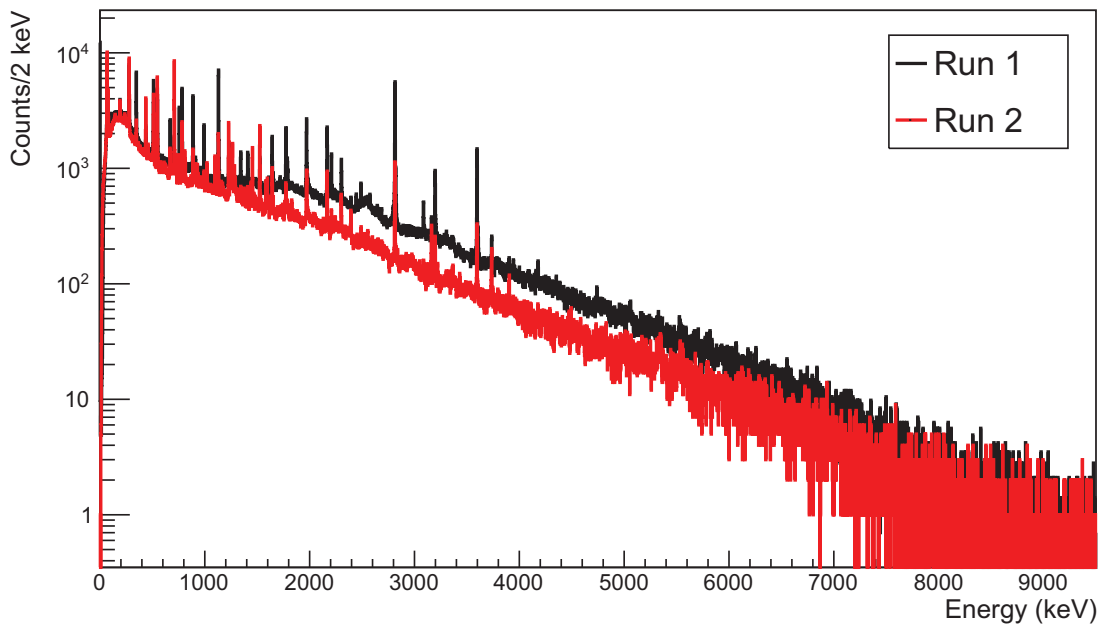
Figure 5.10 γ-ray spectra gated on all α particles, where Run 1 data is scaled based on the ratio of photopeak counts in the 1249 keV γ-ray, corresponding to depopulation of the ^{31}S first excited state.

While it was possible to entirely remove copper background from our experiment, carbon contamination at some level will always be present. As seen in Figure 5.11, the intensity of the 3597 keV line (as well as other ^{39}K lines not shown) are reduced by roughly a factor of five, which suggests the new target is a factor of five cleaner than the old target.
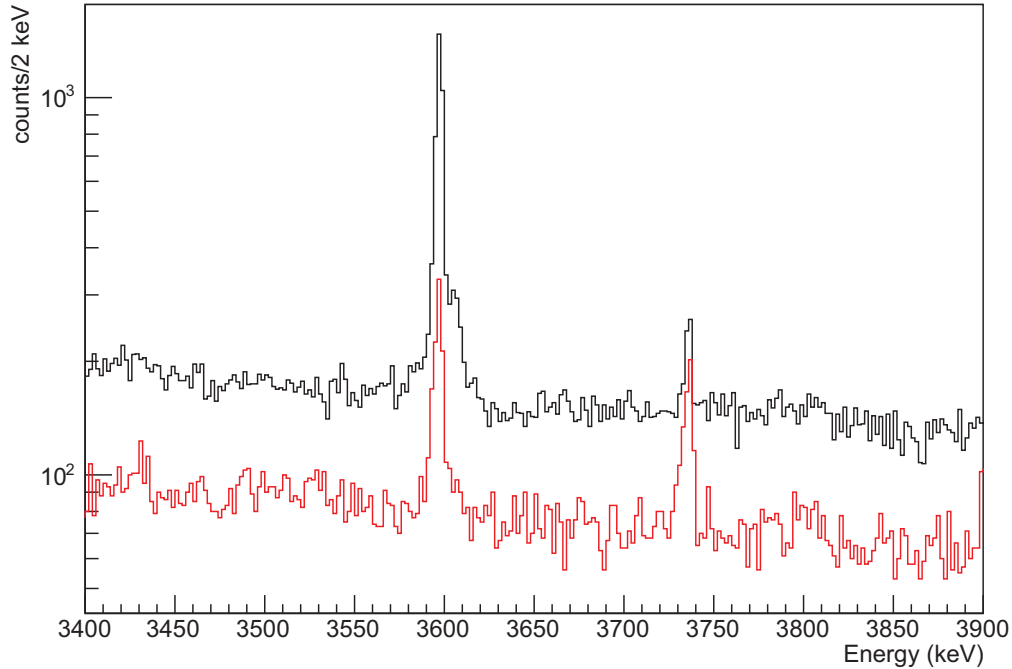
Figure 5.11 Same as Figure 5.10, zoomed in to show two γ-ray lines from carbon contamination, from ^{39}K at 3597 keV and at 3736 keV from ^{40}Ca, and the reduction in intensity from Run 1 to Run 2.

5.3.2 Tentative transition identification

While an in depth analysis of this data set has not yet been performed, I outline here tentative assignments of new peaks seen in this data.

Below, in Figures 5.9-16, α particle energy gated γ-ray spectra are shown for a number of α-particle energies, along with tentative assignments for various peaks, including two states in the region of interest for classical nova nucleosynthesis. To guide the eye, lineshape simulations for these tentative assignments are included, without included background. For states where there is no experimentally determined lifetime in the literature, a lifetime of 10 fs is assumed. Lifetimes of 1-30 fs are expected for most of these states, based on comparisons of ^{31}S states to shell model calculations and the mirror nucleus, ^{31}P. The major difference in lineshapes from 1 fs to 30 fs lifetimes is the width of the lineshape. Shorter lifetimes correspond to a narrower lineshape, and

longer lifetimes correspond to a broader lineshape.
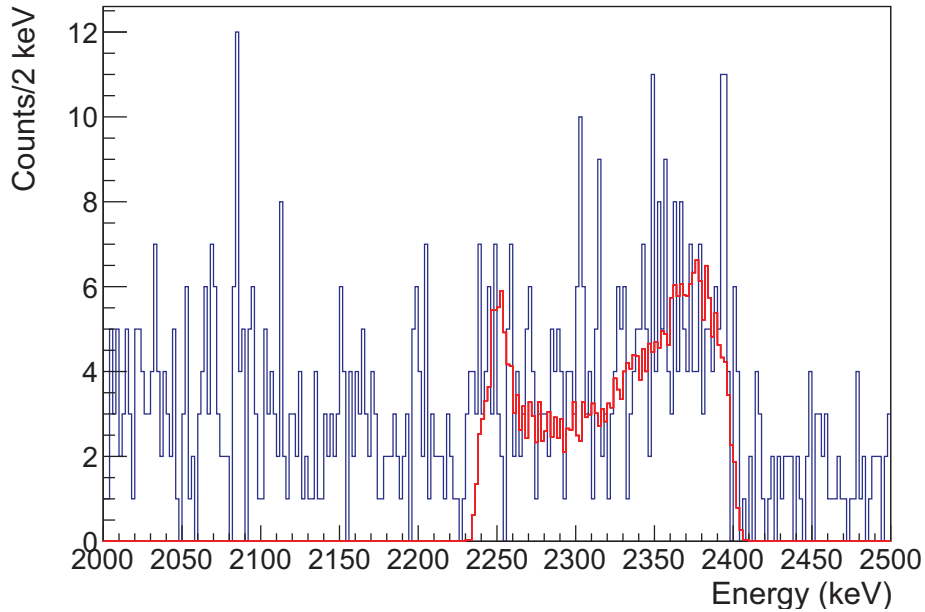
Figure 5.12 Second excited state to ground state transition, gated on α particle energy 47-49 MeV with a simulated lineshape for the literature lifetime of 320 fs (red) [13].

The only ^{31}S excited states observed in this run with literature lifetimes are the first and second excited states. These states can be used to confirm that our lineshape simulation works as expected. We expect to place constraints on bound states at 3077, 4971, and 5157 keV that currently do not have experimentally determined lifetimes in the literature. We also expect to be able to place constraints on lifetimes of two or three states in the region of astrophysical interest, at 6392, 6400, and 6542 keV. Detailed analysis of this data set is beyond the scope of this work.
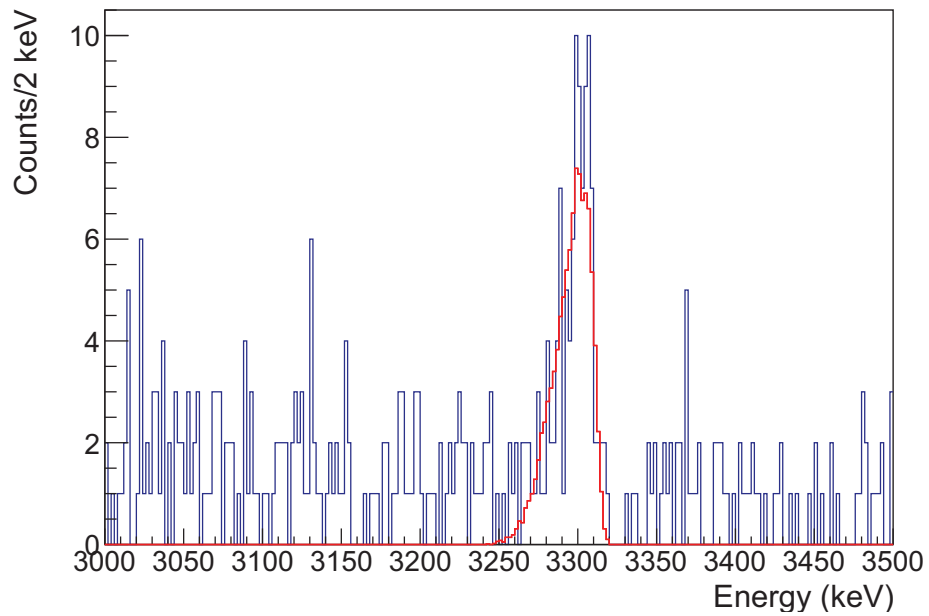
Figure 5.13 Third excited state to ground state transition, gated on α particle energy 46-48 MeV (blue) with a simulated lineshape with arbitrary lifetime of 10 fs (red).
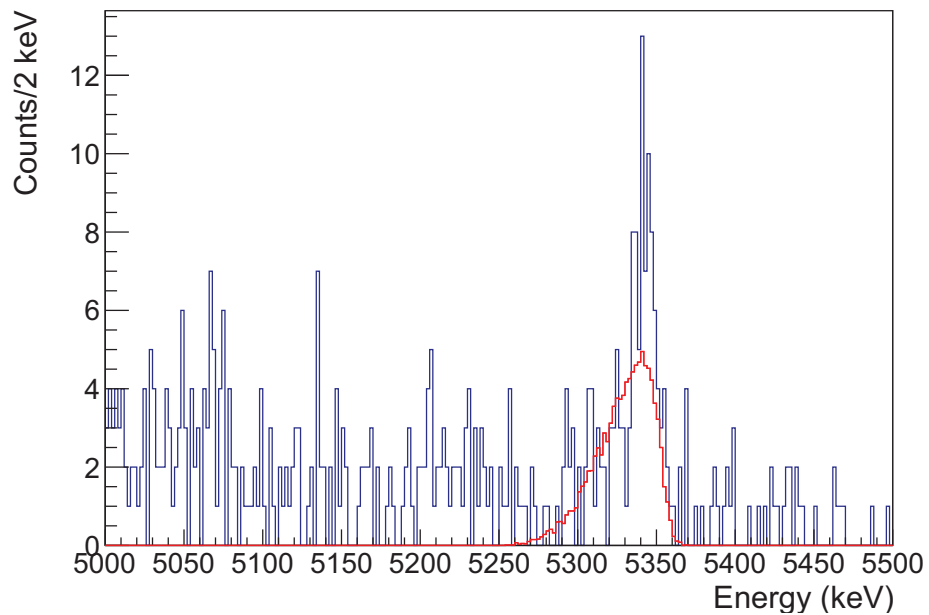
Figure 5.14 4971 keV excited state to ground state transition, gated on α particle energy 42-44 MeV (blue) with a simulated lineshape with arbitrary lifetime of 10 fs (red).
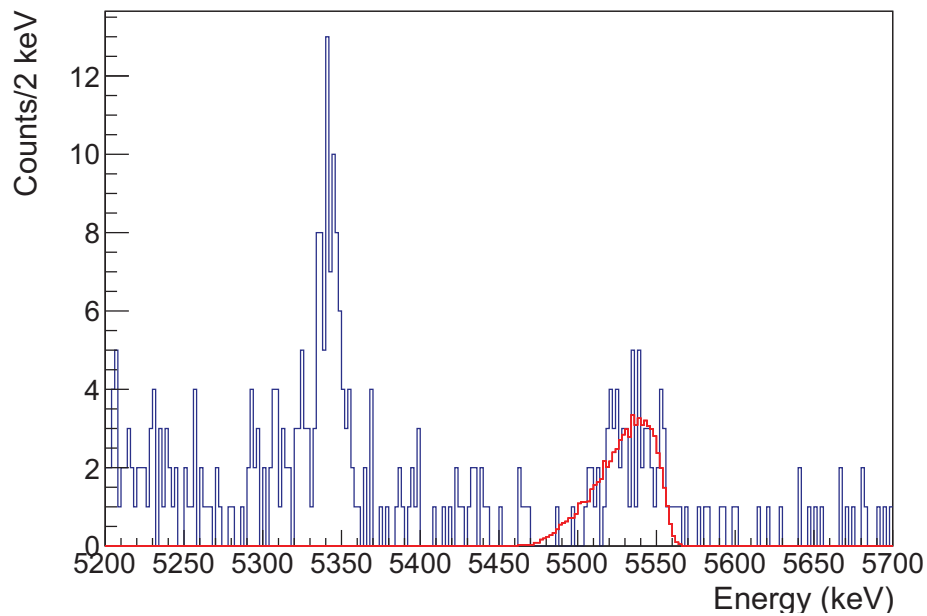
Figure 5.15 5157 keV excited state to ground state transition, gated on α particle energy 42-44 MeV (blue) with a simulated lineshape with arbitrary lifetime of 10 fs (red).
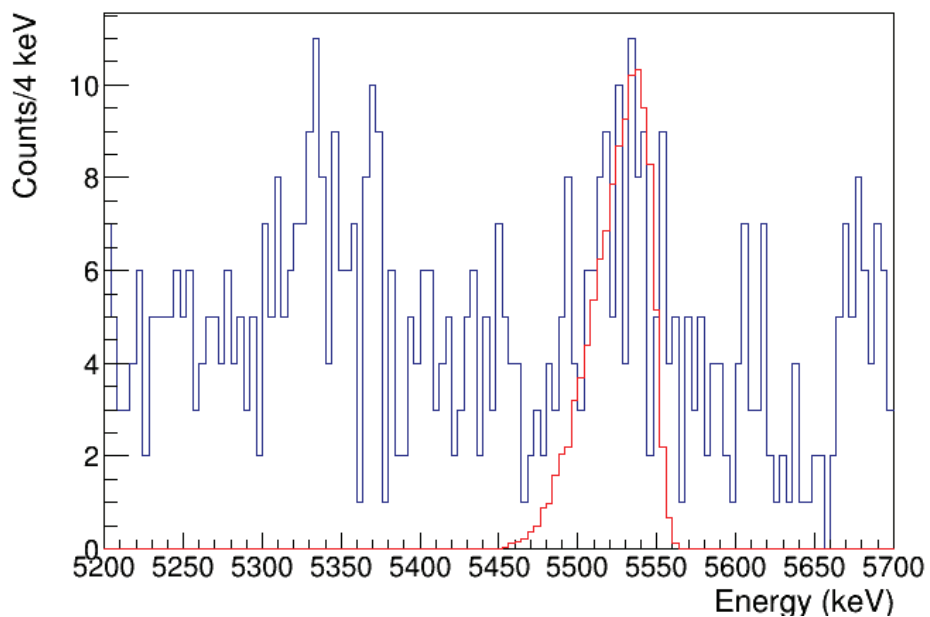
Figure 5.16 6400 or 6392 keV excited state to first excited state transition, gated on α particle energy 39-41 MeV (blue) with a simulated lineshape with arbitrary lifetime of 10 fs for the 6400 keV state (red).
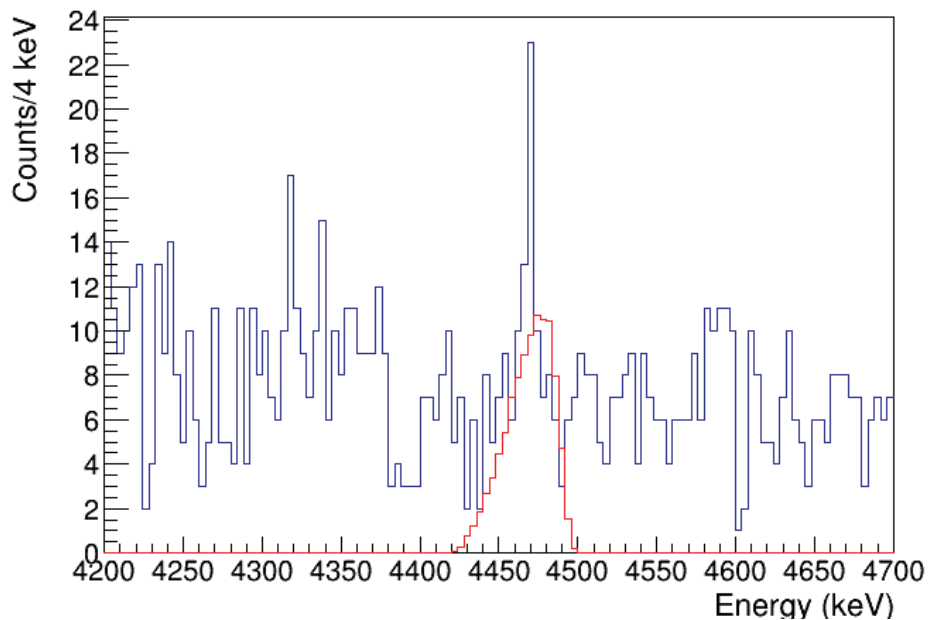
Figure 5.17 6400 or 6392 keV excited state to second excited state transition, gated on α particle energy 39-41 MeV (blue) with a simulated lineshape with arbitrary lifetime of 10 fs for the 6400 keV state (red).
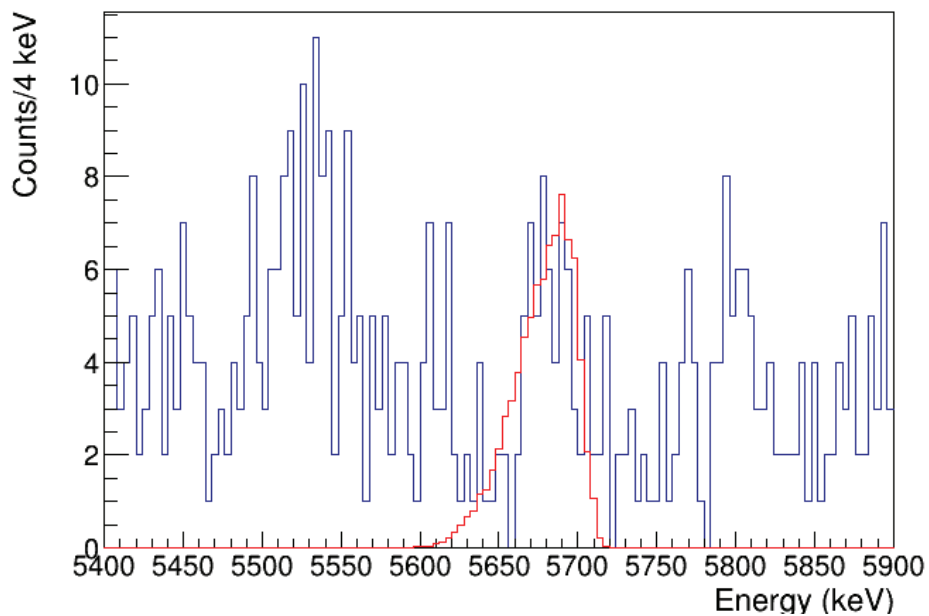
Figure 5.18 6542 keV excited state to first excited state transition, gated on α particle energy 39-41 MeV (blue) with a simulated lineshape with arbitrary lifetime of 10 fs (red).

CHAPTER 6

^{36}Ar$(d,t)^{35}$Ar EXPERIMENT

This chapter discusses the method used to search for ^{35}Ar excited states just above the proton emission threshold. The procedure for making the ion-implanted targets used for this measurement is briefly discussed and the remaining portion of the chapter discusses measurements performed at the Maier-Leibnitz Laboratorium (MLL) in Garching, Germany in January 2014. The layout of the facility can be seen in Figure 6.2.

6.1   Ion-implanted C targets

The ^{36}Ar targets used were fabricated by implanting 3-6 µg/cm^2 ^{36}Ar into a 30 µg/cm^2 ^{nat}C foil at the Center for Experimental Nuclear Physics and Astrophysics (CENPA) using several beam energies (25-70 keV) to provide a more uniform depth distribution than a single beam energy would permit. This technique was used to fabricate targets of several isotopes, including ^{36}Ar. A model of the depth distribution is shown in Figure 6.1. Further details of the implantation and other uses of these targets can be found in [14, 56, 57]. One target used in this run was fabricated by the authors of [14] and backup targets were fabricated by Ronaldo Ortez and Alejandro Garcia, coauthors on [58].

^{32}S targets were used for calibration. 10.4 µg/cm^2 of ^{32}S ions were implanted into 40 µg/cm^2 isotopically enriched ^{12}C foils. This implantation was carried out at the Tandetron Accelerator Laboratory (TAL) at University of Western Ontario, as described in [59, 25, 26]. This target was chosen over the ^{32}S target made using the procedure outlined in [14] used for the ^{36}Ar target due to the higher amount of ^{32}S and lower amount of ^{13}C.
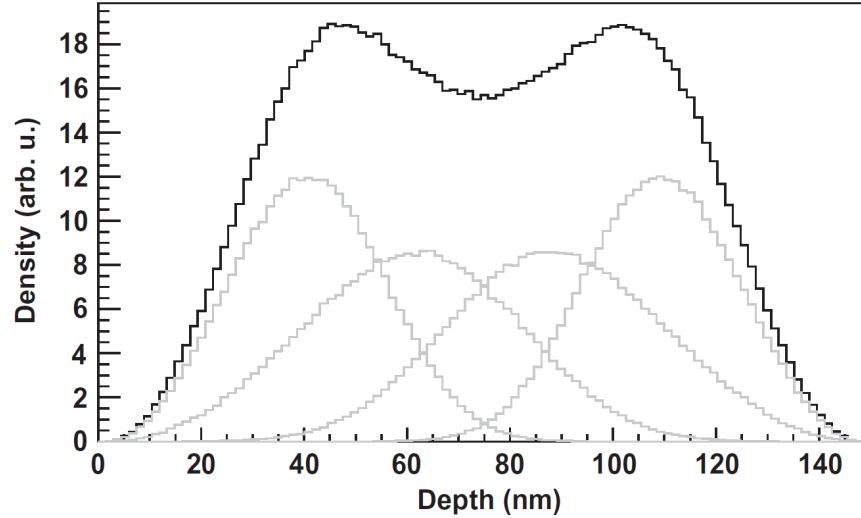
Figure 6.1 Calculated depth distribution for ^{24}Mg implanted in C foils using the same methods as the ^{36}Ar target, as discussed in [14]. The black line represents the total depth distribution, and the grey lines show components from individual energies.

6.2 ^{2}H ion source

This section discusses the ion source used to provide the deuteron beam used for this measurement. Molecular deuterium (D$_2$) gas is moved into a dissociator by an atomic jet, which is created by adiabatic expansion [60]. A radiofrequency (RF) field is created in the cold plasma in the dissociator using a high frequency AC circuit. This causes the electrons in the plasma to oscillate in helical orbits. These electrons collide with the molecular deuterium, producing neutral atomic deuterium. This deuterium then enters another pumping stage, which helps to minimize the scattering of the beam and charge exchange between the atomic and residual molecular deuterium. This provides intensities on the order of 10^{16} atoms/s for the Electron Cyclotron Resonance (ECR) ionizer.

The ECR ionizer ionizes the atomic deuterium, producing D$^+$ ions by impacting electrons in a static magnetic field and an RF field in a plasma. An axial magnetic field is provided by two sets of coils, which helps to confine the plasma. The 2.45 GHz RF field is applied to the plasma through a waveguide, insulated by a cylindrical pyrex tube. Radial confinement is provided by a sextupole field produced by FeNdB magnets. This ionization process has an efficiency of a few percent.

The ion beam is then transported through a system of electrostatic lenses into a cesium vapor
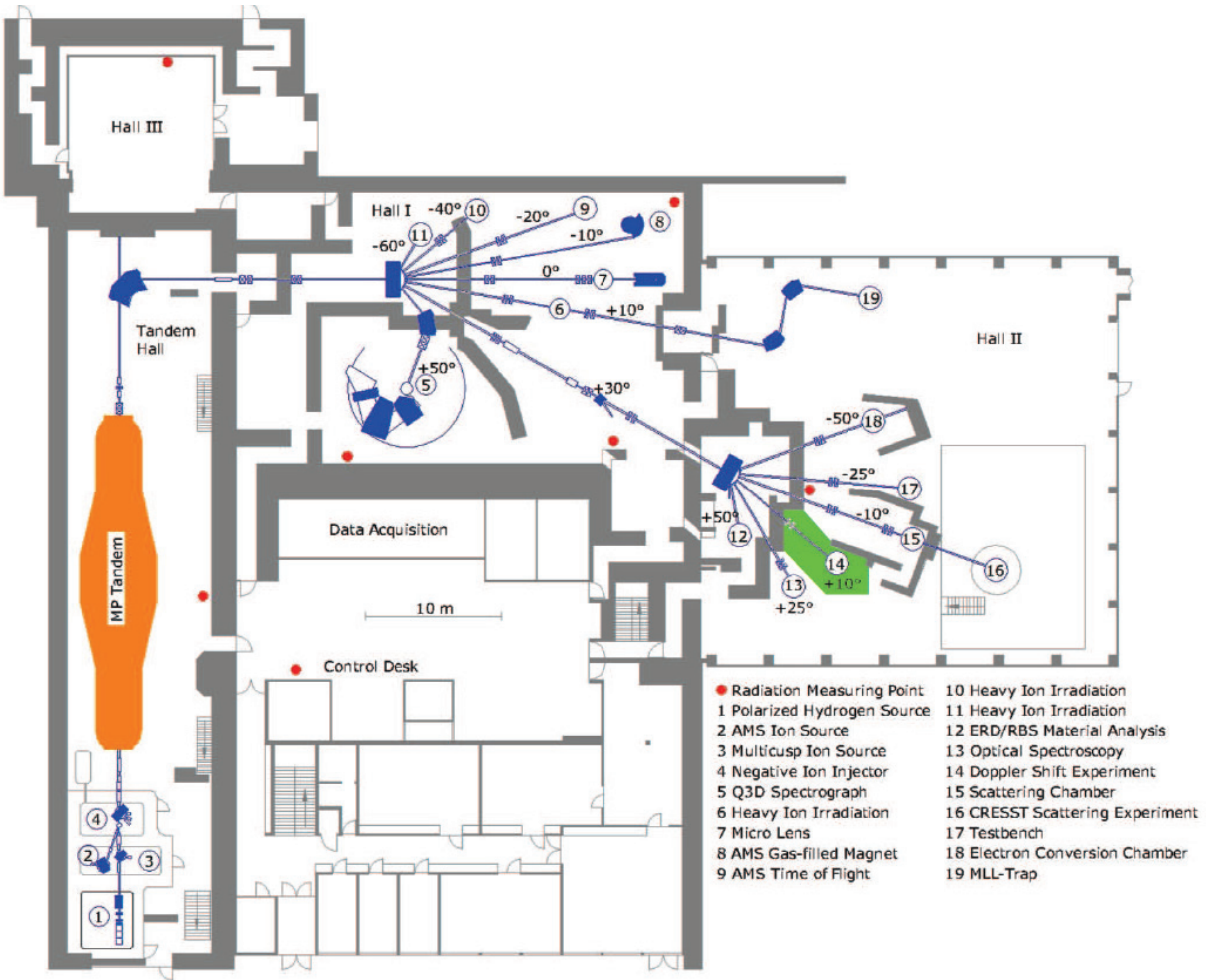
Figure 6.2 Layout of the MLL facility

region. The extraction electrodes are placed at a large diameter to allow the atomic beam to leave the region unhindered to be pumped out. The beam is extracted by a series of electrodes followed by an Einzel lens, which focuses the beam without changing its energy using electrostatic fields. The beam is then focused onto a cesium target (which has a low ionization energy), where it acquires a negative charge (D^-). This charge flipping efficiency is approximately 22%. The beam then leaves this region with an energy of a few hundred keV. A conceptual flow chart of the source can be found in Figure 6.3.
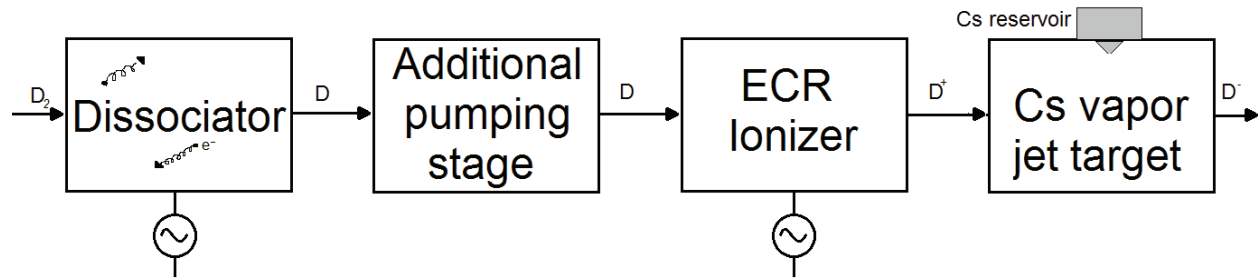
Figure 6.3 Flow chart of the ion source components at MLL

6.3 Munich M-P tandem Van de Graaff accelerator

After leaving the ion source, the deuterons are further accelerated by the MP tandem Van de Graaff accelerator, downstream of the Cs vapor target. Like most Van de Graaff accelerators, there is an electrically charged terminal that accelerates the charges through a series of insulated tubes in high vacuum. However, for this tandem accelerator, there are two sets of accelerating tubes in one pressure tank. At the junction of these two accelerating tubes is a positive high voltage terminal. This terminal is kept at a high voltage by delivering charge using three pelletron chains which each deliver a current of 100 μA [61]. These chains consist of metal pellets charged by induction that are joined by insulating nylon.

Negative ions coming from the Cs vapor target are accelerated to an energy given by the charge times the voltage. They are then charge stripped in a carbon foil and accelerated again, this time with a positive charge. For isotopes of hydrogen, the ions reach an energy of $E = 2q_e V$, where V is the terminal voltage and q_e is the electron charge. After acceleration, the beam is bent by an analyzing magnet through a set of slits that provides a further cut on beam energy, improving the resolution. More information on this accelerator can be found in [61].

6.4 Target interaction

The beam is then delivered to the target chamber upstream of the Q3D spectrograph. The target chamber is a cylindrical metal vacuum chamber and houses the target ladder. Once the target ladder

is inserted, the chamber is pumped down to avoid energy loss and background reactions on air in the chamber. Each target ladder has 6 positions, 5 for targets, and a collimator for beam tuning. A schematic of the target ladder can be seen in Figure 6.4.
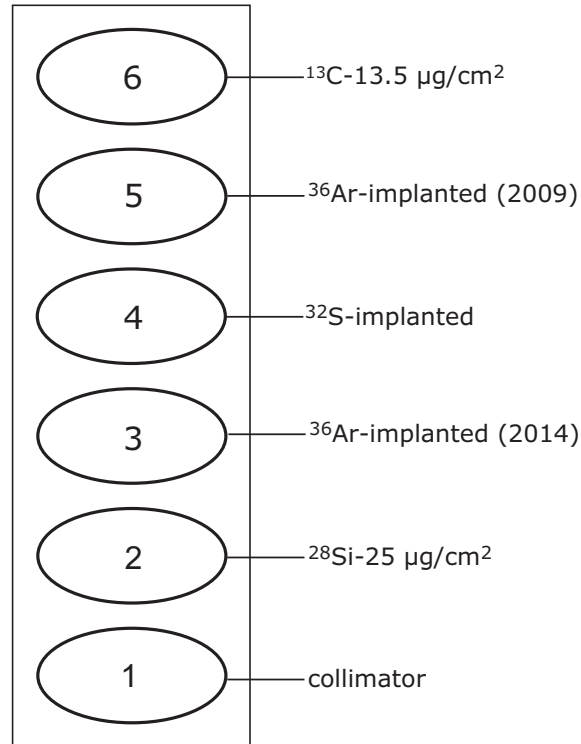
Figure 6.4 Schematic of the Munich target ladder and targets used in the run. Details of the implanted targets are discussed in the text. ^{36}Ar targets are labeled by the year of first use.

The target can also be rotated by an angle θ in the plane between the beam and the target. Increasing the angle θ increases the amount of target nuclei seen by the beam, increasing statistics. However, increasing this angle also increases the effects of energy loss and straggling within the target, effectively broadening the peak shape of triton position at the focal plane. The energy loss of the higher energy deuterons is much less than that of the lower energy tritons, leading to an asymmetric peak shape.

The amount of charge incident on the target is also a quantity of interest. A Faraday cup is located behind the target at $0°$ and connected to a current integrator. This determines the amount of charge that has passed through the target. Since most of the deuterons pass through the target

without undergoing nuclear reactions, this is a good approximation of the total beam current incident on the target. The Faraday cup also provides instantaneous current, which is a useful way to monitor the stability of beam delivery. During this experiment the beam current was typically 200-700 nA.

6.5   Q3D magnetic spectrograph

For this measurement, a magnetic spectrograph was used to separate the reaction products of interest. The light reaction products traverse a magnetic field and are separated by their momentum over charge. The momentum can then be calibrated for each particle group from position information in the focal plane. Knowing the momentum of the reaction product and the ground state masses, excitation energies can be determined. The spectrograph focuses light reaction products onto a position sensitive detector. For the sake of acquiring statistics, a large solid angle acceptance is also desired.

These requirements, along with kinematic broadening need to be corrected for in the geometry and magnetic field configurations. Spectrographs are typically optimized using computer simulations and ray tracing. These aspects were considered in the design of the Q3D (quadrupole-dipole-dipole-dipole) spectrograph. The quadrupole focuses the particles in the vertical direction and defocuses in the horizontal direction. The first dipole then focuses the particles onto a line in the horizontal direction. A multipole element then corrects for kinematic broadening in the horizontal direction. The particles then see two more dipoles separated by an electrostatic deflector. A schematic is shown in in Figure 6.5.

The solid angle acceptance of the Q3D assuming the entrance slits are fully open is 13.9 msr, which was the case throughout this experiment. The attainable energy resolution $\Delta E/E = 2 \times 10^{-4}$ is similar to that of the tandem accelerator. The operating software takes as inputs the reaction of interest and the excitation energy and applies settings to place reaction products corresponding to the state of interest to be at the center of the focal plane detector. Proton NMR is used to monitor
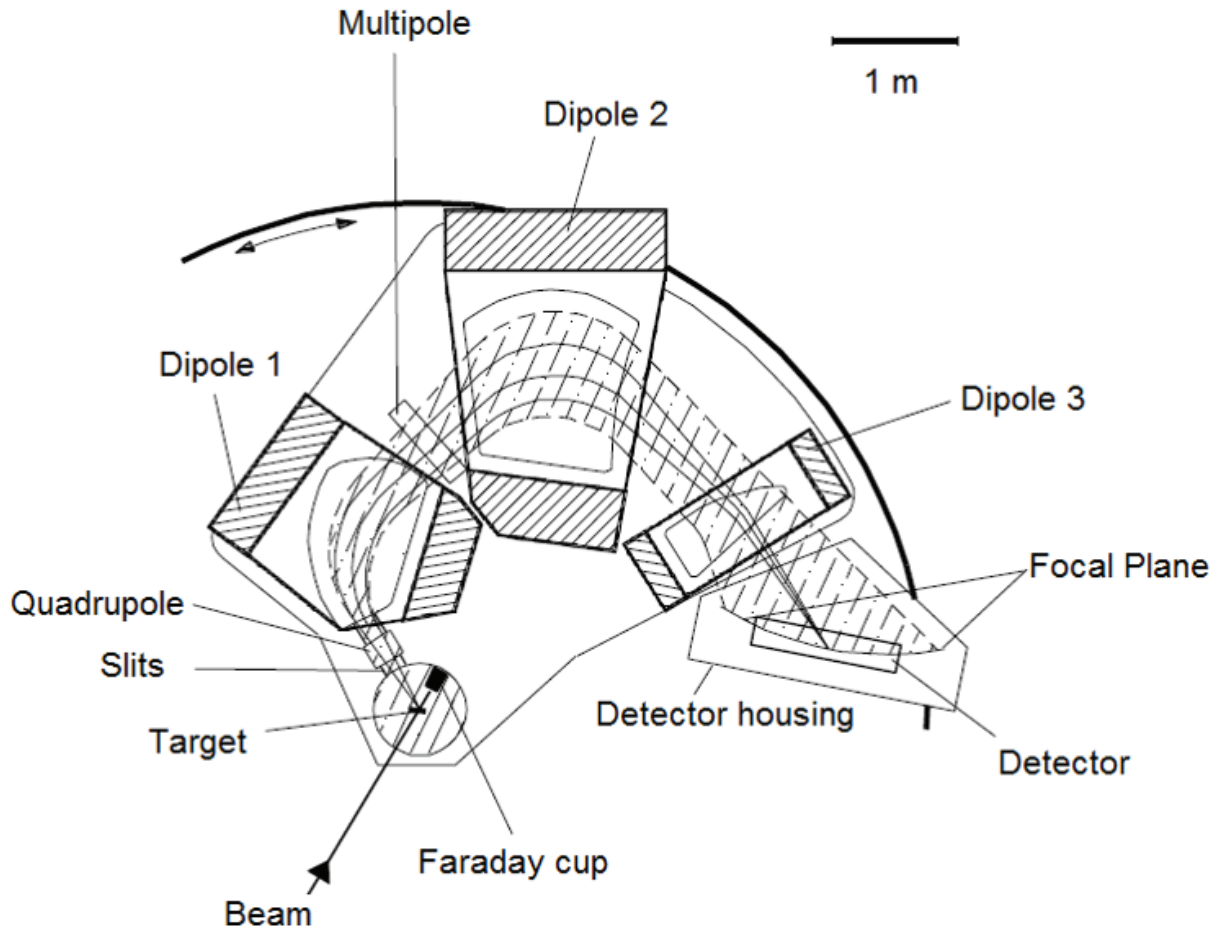
Figure 6.5 Top down view of the ion optics of the Q3D magnetic spectrograph at MLL. Figure adapted from [15].

and stabilize the magnetic field produced by the second dipole.

6.6 Position sensitive cathode strip detector

After the particles have been separated, they are detected at the focal plane by a device with similar resolution to the beam energy and the Q3D field configuration to take advantage of this high resolution setup. In this case, a position sensitive cathode strip detector was designed with these criteria as well as things such as detector geometry and positioning in mind. A diagram of the entire detector can be seen in Figure 6.6.

A particle enters the detector by passing through 25 µm Kapton foil into a region filled with
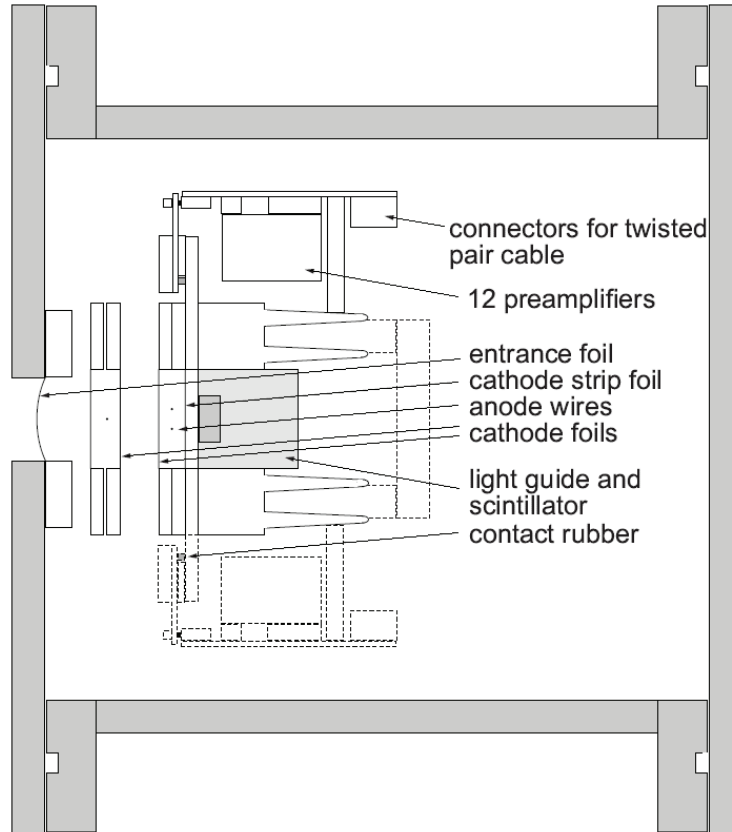
Figure 6.6 Top down view of the focal plane detector of the Q3D. Figure from [16].

isobutane gas. The particle then encounters a proportional counter consisting of a cathode foil and an anode wire. The particle ionizes the gas and creates electron-ion pairs. The particles near the anode will be accelerated, and then ionize more gas atoms, creating a charge avalanche. The charge collection at the anode is proportional to the energy loss of the particle from the first ionization. This energy loss is referred to as $\Delta E1$.

The particle then passes through the cathode foil, a gas filled region, and another cathode foil, both made of 2.9 μm aluminized mylar [15, 16]. The particle enters another proportional counter composed of two anode wires. The particle then creates an avalanche of ion-electron pairs. Energy loss is then measured and called ΔE.

Cathode strips are located after the anode wires. These cathode strips are electrically isolated and 3.5 mm wide, with a separation distance of 0.5 mm. There are 255 of such strips that cover 890 mm of the Q3D focal plane. Based on the incoming angle, charge is typically induced on about

6 strips. The position can then be extracted by fitting the charge distribution with a Gaussian. A diagram showing this position reconstruction based on the induced charge can be seen in Figure 6.7. The particles then travel through the cathode strips and deposit their residual energy in a scintillator.
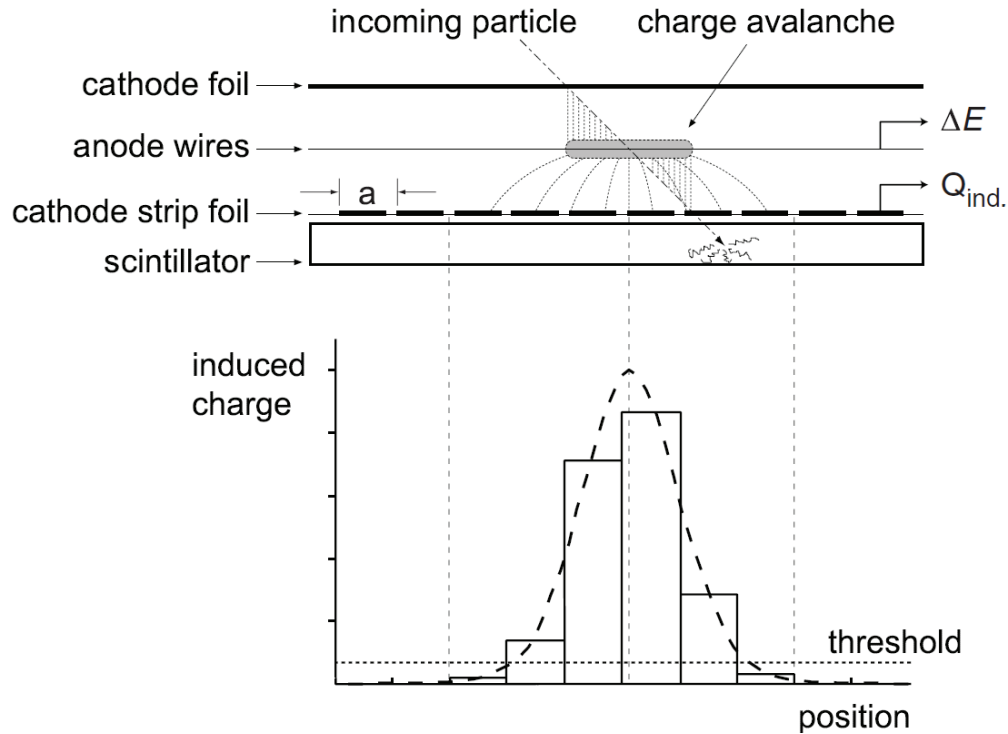
Figure 6.7 Conceptual diagram of the position reconstruction used in the MLL Q3D focal plane detector. Figure from [16].

While a Gaussian fit provides better position resolution, using this method online is too slow and would increase the dead time. Instead, the center of gravity method is used to look at online data. This calculation is similar to finding the center of mass of a system of masses. The calculation is faster but introduces systematic effects due to the separation of the cathode strip foils. Periodic minima occur in the position spectra. Gaussian fits can then be performed offline, and after performing this fit, the position resolution is reported to be less than 0.5 mm FWHM [15].

6.7 Data acquisition system (DAQ)

The data acquisition system at MLL is called the Multi-Branch System (MBS) and ROOT based online/offline utility (MARaBOU). This system controls the conversion of analog signals and produces digital outputs to be interpreted and manipulated by the acquisition computer. The MBS developed at GSI in Darmstadt, is used as the front end, which reads out the data, builds the events and transports the data. The back end provides software libraries for setup, run control, and for data analysis and storage, using the ROOT analysis software. More details can be found in [62].

The modules used in the data acquisition are connected and operated under the Computer Automated Measurement and Control (CAMAC) system. The system is set up such that the Application Specific Integrated Circuit (ASIC) only records good events. For an event to be recorded, it is required that 3-7 adjacent cathode strips have induced charge above the threshold within a window of 100 ns. If this event has an invalid multiplicity, then the system is reset, which takes about 4 μs. If an event is good, then the signals are sent to an Analog to Digital Converter (ADC) and the event is written to disk. A diagram of the electronics can be seen in Figure 6.8.
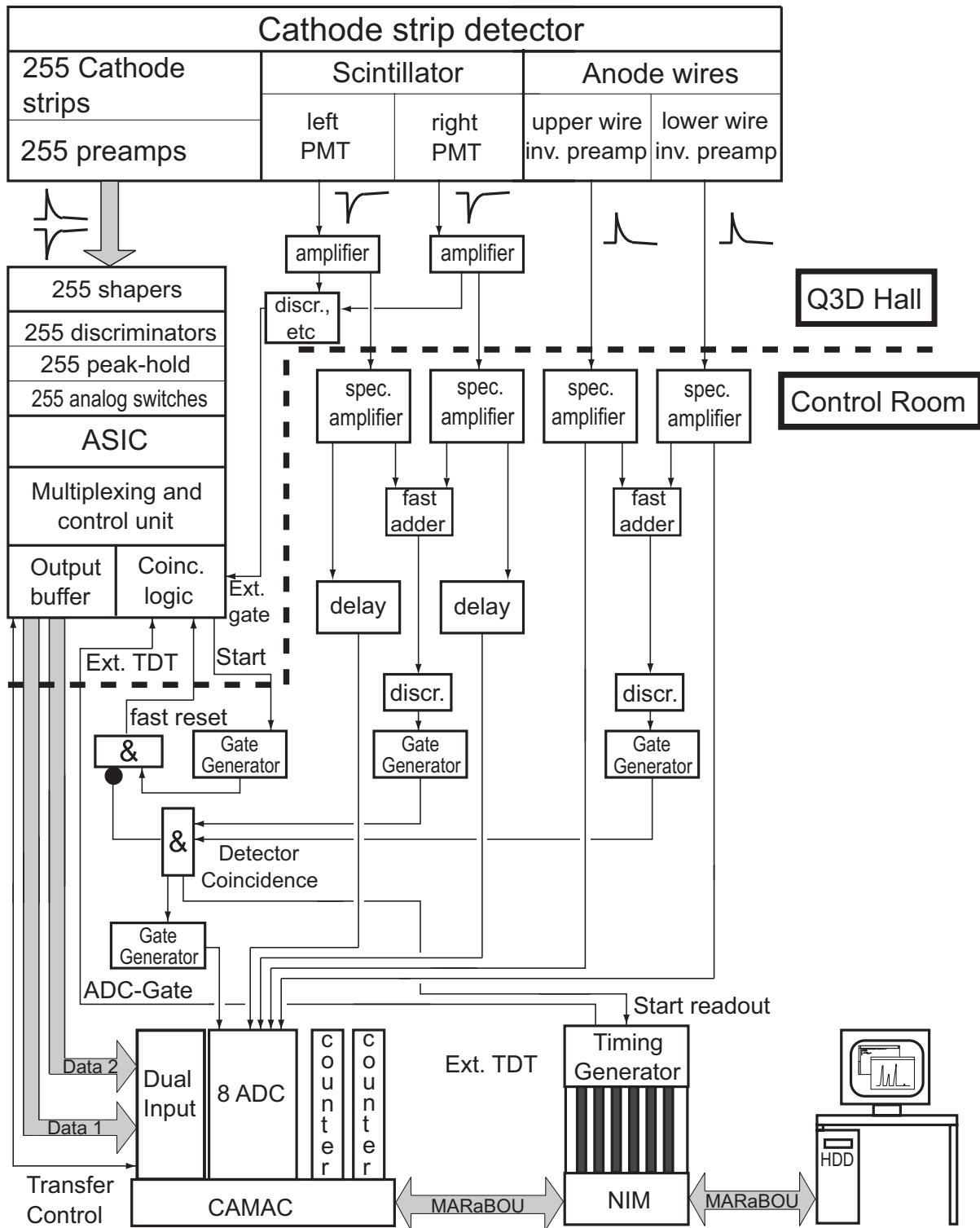
Figure 6.8 Diagram of the DAQ electronics for the MLL experiment. Figure adapted from [15].

This chapter gives an overview of the data analysis and a discussion of the results of the experiment outlined in the previous chapter. Many of the techniques discussed here are applicable to other transfer reaction studies. Particle identification (PID), spectrograph plotting, calibration techniques, and extracted excitation energies are discussed. A discussion of the measured level density of ^{35}Ar is also presented.

7.1 Particle identification

Particle identification was performed by gating on a $\Delta E - E$ plot. ΔE is measured in a detector that is sufficiently thin that the charged particle deposits some, but not all of its energy, and then the remaining energy is measured in another detector. This energy loss gives us information about the charge of the incoming nucleus. The stopping power, dE/dx, can be described using the Bethe formula given below

$$-\frac{dE}{dx} = \frac{4\pi e^4 Z^2}{m_e v^2} NB \tag{7.1}$$

where

$$B \equiv z\left[\ln\frac{2m_e v^2}{I} - \ln\left(1 - \frac{v^2}{c^2}\right) - \frac{v^2}{c^2}\right] \tag{7.2}$$

and v, Ze, z, N, and m_e are the velocity and charge of the incoming charged particle, the atomic number and number density of the absorber atoms, and the electron mass, respectively. I is a parameter related to the mean excitation and ionization potential of the absorber that is typically determined experimentally. For particles passing through the same amount of absorber, Δx, then the energy loss, $\Delta E \propto \frac{Z^2}{v^2}$. If we multiply by $E = \frac{1}{2}Mv^2$, we find that

$$\Delta E \times E \propto M \times Z^2 \tag{7.3}$$

Then a $\Delta E - E$ plot should show hyperbolic curves for each particle group corresponding to different values of MZ^2, as seen in Figure 7.1.
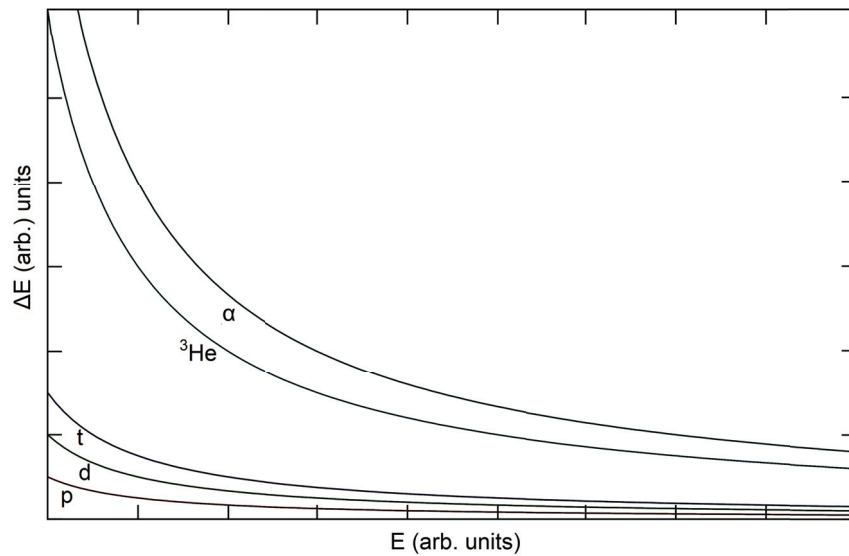
Figure 7.1 Expected shape and relative separation for stable hydrogen and helium isotopes

In this case, the ΔE detector is a multi-wire proportional counter, and the rest of the energy (E) is deposited in a plastic scintillator. Due to the geometry of the detection setup (discussed in Section 6.6) ΔE depends on the incoming angle, which effectively broadens the expected line width. The total energy is constrained by the Q3D settings, turning the expected bands into more circular shapes. Similarly, a comparison of the total energy lost in the proportional counter (ΔE) can be compared to the energy lost in a portion of the proportional counter (ΔE_1) to provide further constraints on the PID. These plots, including triton gates can be seen in Figure 7.2.

7.2   Background subtraction

In this experiment, the targets used contained ^{36}Ar, ^{12}C, and ^{13}C. Both ^{12}C and ^{13}C have the potential to introduce background in addition to the peaks of interest from reactions on ^{36}Ar. For all but the 25° data, all peaks from ^{12}C$(d,t)^{11}$C are excluded from the focal plane by the kinematics. In the 25° data, the first excited state of ^{11}C (E_x=2000.0(4) keV) is populated, but the
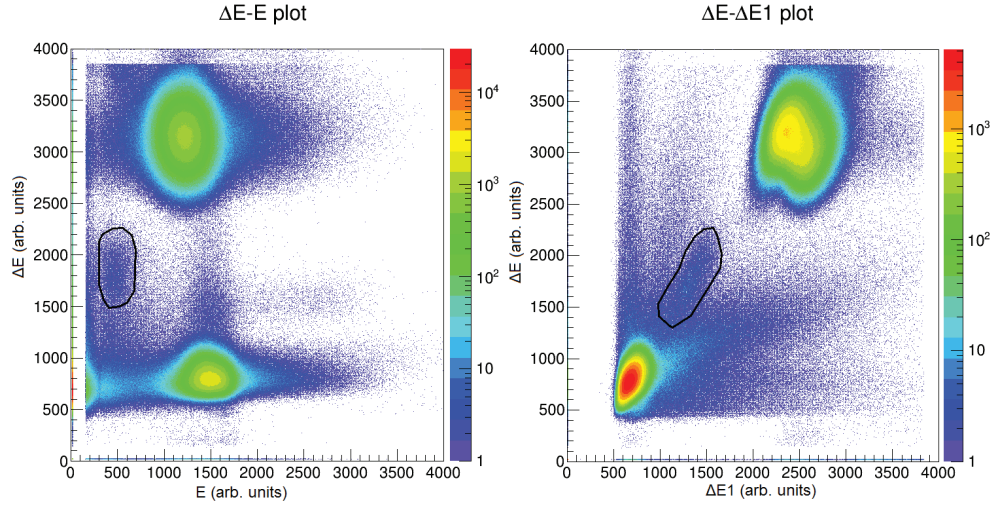
Figure 7.2 Particle identification plots, along with triton gates, for the first set of $15°$ data taken on the ^{36}Ar implanted target. The particle group at high ΔE corresponds to α particles, and the particle group at low ΔE corresponds to unresolved protons and deuterons.

corresponding peak is on the edge of the focal plane. To deal with this, an additional peak was added to the fit in that region.

^{13}C$(d,t)^{12}$C produced a broad, defocused peak (E_x=16.1 MeV) in all of the spectra other than the $54°$. Spectra from these runs can be seen in Figure 7.3. In addition, nearby peaks with large intrinsic widths of 1.15 and 1.5 MeV produced a relatively flat background. To deal with this background, runs were taken on an enriched ^{13}C target with a thickness of 13.5 μm/cm^2. Then based on the amount of ^{13}C in each of the targets and the dead time corrected integrated beam rate, a normalization was applied to the collected ^{12}C spectra. These targets were also different thicknesses. The differences in energy loss were estimated to be 2 keV at $15°$, $20°$, and $25°$, and 3 keV at $54°$ (due to the increased effective thickness because of the geometry).

For this analysis, spectra were rebinned by a factor of five. Once this was done, a rough calibration of 1 bin≈0.5 keV was obtained. This was used to determine the shift to apply to the ^{13}C$(d,t)^{12}$C spectra. After applying these corrections, a bin by bin subtraction was performed. Poisson statistics were used to estimate the errors in the number of counts in each bin, and these uncertainties were then combined for the subtracted spectra. These spectra were then used for the final fitting in the analysis of this data. An example spectrum can be seen in Figure 7.4.
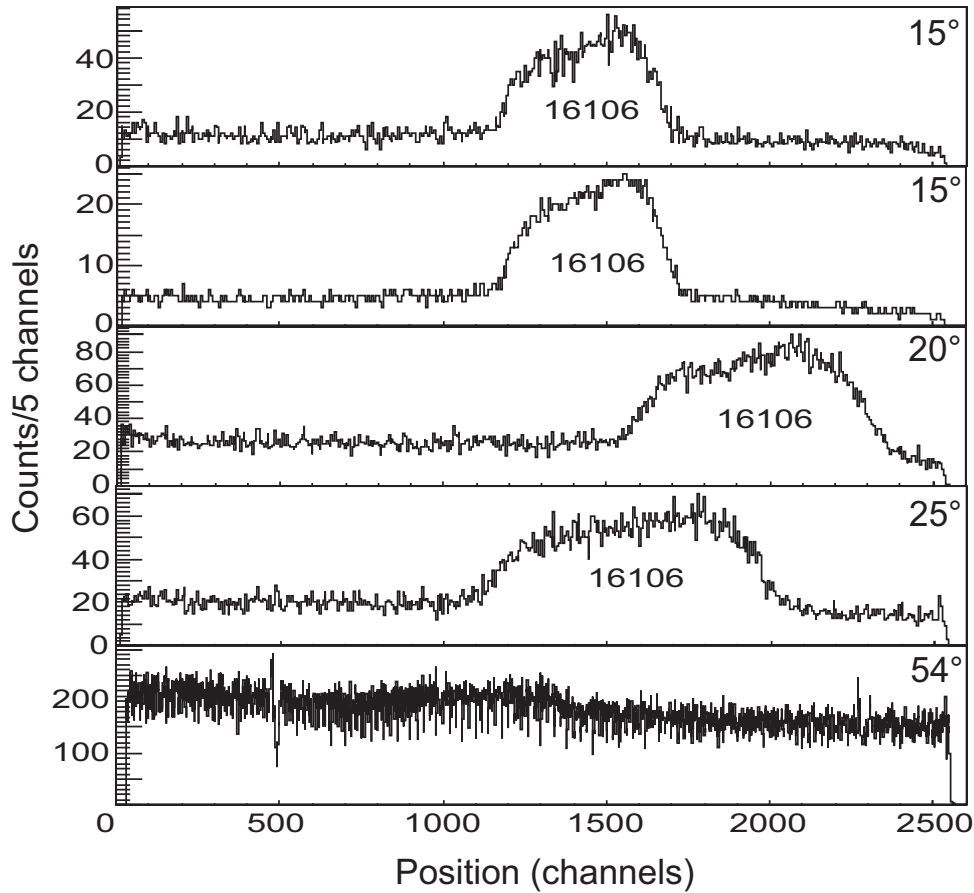
Figure 7.3 $^{13}C(d,t)^{12}C$ data.

7.3 Spectrograph plotting

Once the reaction of interest has been identified, known peaks in the position spectrum need to be identified. For this measurement, it was expected that we would see many previously unidentified peaks, but the ^{31}S and ^{27}Si peaks need to be identified before they can be used to calibrate the excitation energies of the ^{35}Ar peaks. For this work, a program called SpecPlot, which is a part of a larger simulation package Nukesim-classes [63], was used.

SpecPlot calculates the bending radius (ρ) of each of the light reaction products given momentum p and charge q, in a magnetic field B. The momentum can be determined using relativistic kinematics. If we combine these results we see that for a particle with an energy E, their radius is

74
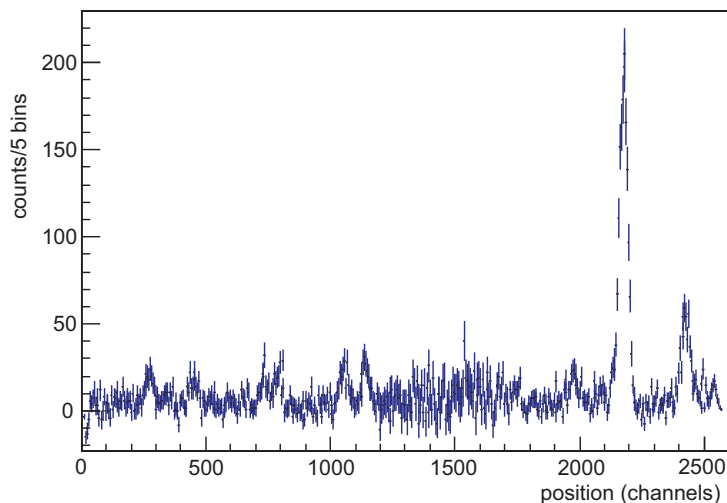
Figure 7.4 A background subtracted ^{36}Ar$(d,t)^{35}$Ar spectrum taken at $15°$.

given by

$$\rho = \frac{1}{qB}\sqrt{\left(\frac{E}{c}\right)^2 - (mc)^2}$$

(7.4)

Using the knowledge of the light reaction product and using conservation of energy, one can determine the mass of the excited state (ground state mass plus excited state energy) of the heavy recoil nucleus. SpecPlot calculates the focal plane position of the light reaction products given information on the ground state mass and excitation energy inputs. Light particle energy increases with increasing ρ, which corresponds to decreasing excitation energy in the target nucleus. Figure 7.5 shows an example of this calculated position spectrum.
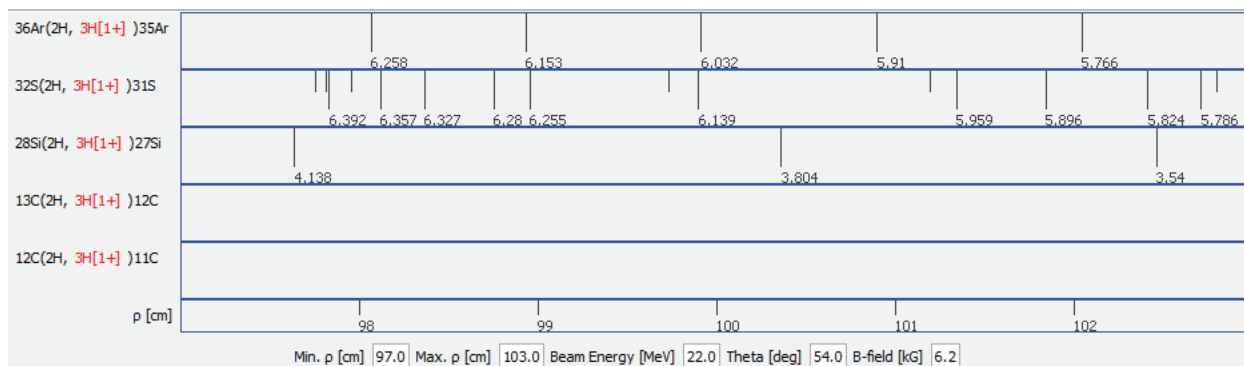
Figure 7.5 A sample SpecPlot output for relevant reactions at $54°$.

SpecPlot takes as inputs both nuclear masses and excitation energies for all nuclei involved in

75

the calculation. Mass inputs for this code come from the 2003 Atomic Mass Evaluation (AME) [64]. This mass database was compiled in 2003, and since then more information has become available, and further mass evaluations have been performed. However, at this level, the previous data is sufficient to estimate the peak locations. Input excitation energies were taken from the Evaluated Nuclear Structure Data File (ENSDF) database [13]. Information on the beam energy and the reaction products, as well as the spectrograph angles are also required inputs.

To identify peaks, one can compare to previous data or use the Q3D centering settings to identify a reference state. From there, one can try to line up all other states in SpecPlot to a corresponding state in the position spectrum. This program is limited by the fact that it assumes that the particles traverse a constant magnetic field. The field strengths within the Q3D are not constant, but this provides a useful approximation. The input parameters such as radii and B can be tuned to attempt to match what is seen on the focal plane. Therefore the states are not expected to line up exactly. The Q3D dispersion also has a small variation which can add to these effects. Figure 7.6 shows a SpecPlot window aligned with ^{31}S and ^{35}Ar spectra obtained at $15°$.

SpecPlot can be used as a guide for identification of the states populated from both expected reactions and potential target contaminants. It is also useful in the planning of these experiments. Different beam energies and spectrograph angles can be input to optimize these parameters before the run. These parameters can be selected so that potential contaminant peaks are out of the way of those peaks of interest. Spectra used for calibration can be seen in Figures 7.7 (^{31}S) and 7.8 (^{27}Si).

7.4 Peak fitting

After the reaction products of interest are selected and calibration peaks are identified, the next step in this data analysis is to determine the peak centroids, for both calibration peaks and peaks of interest. This fitting was performed in ROOT [65]. The software that applies the PID gates and performs the position reconstruction mentioned earlier outputs a ROOT file containing histograms
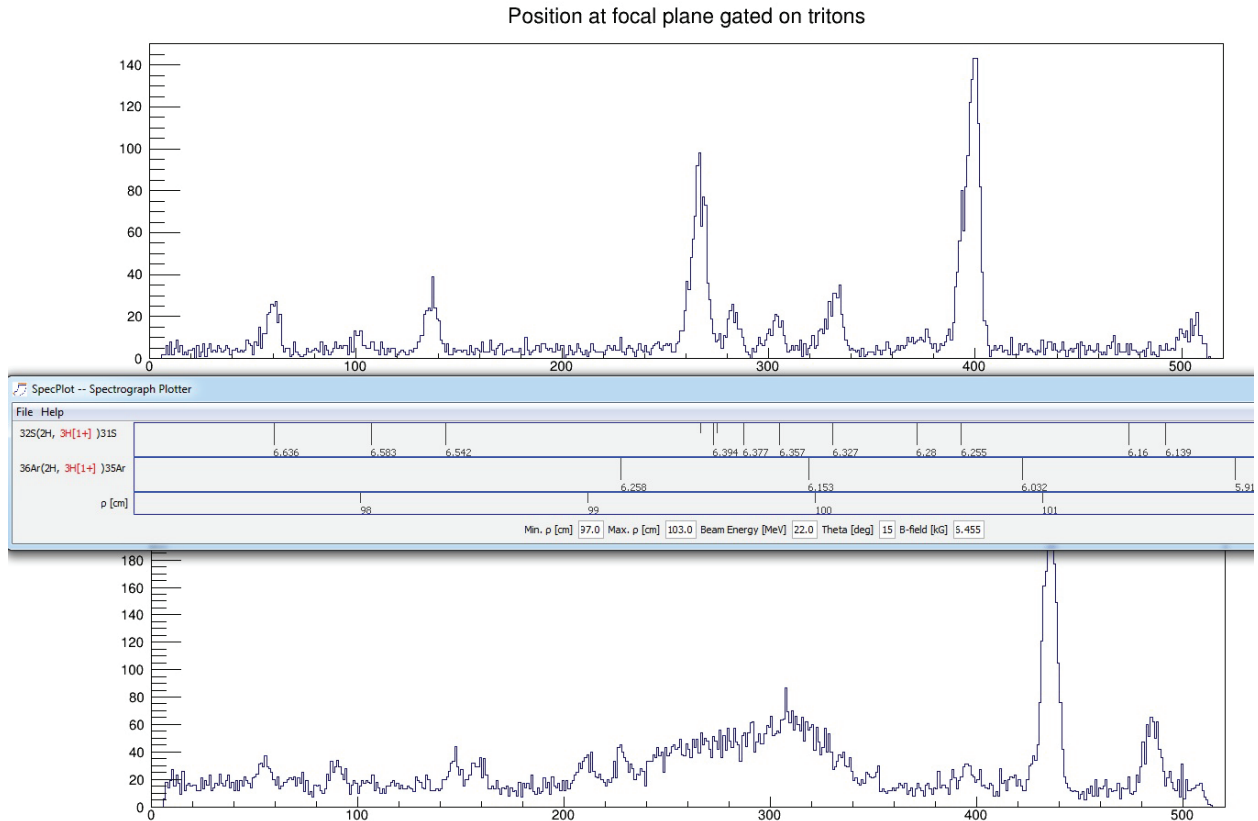
Figure 7.6 Data taken at 15°, showing the ^{32}S$(d,t)^{31}$S and ^{36}Ar$(d,t)^{35}$Ar spectra overlaid by SpecPlot, roughly aligning previously identified peaks. Only previously known information on ^{35}Ar is included in the SpecPlot input.

of the PID plots and the position spectrum.

Due to dissipative effects such as energy straggling in the target, an asymmetric peak shape was necessary to fit the observed peak shape. An exponentially modified Gaussian, which is the convolution of a Gaussian and an exponential was chosen for this analysis. This fit function can be written as:

$$f(x) = A \exp\left(\frac{\sigma^2}{2\tau^2} + \frac{x-\mu}{\tau}\right) \mathrm{erfc}\left(\frac{1}{\sqrt{2}}\left(\frac{\sigma}{\tau} - \frac{x-\mu}{\sigma}\right)\right) \tag{7.5}$$

where erfc is the complementary error function, A is related to the height of the peak, τ describes the asymmetry of the peak, σ is the width of the Gaussian, and μ is the centroid of the Gaussian.

A ROOT macro was written to fit a given number of peaks with this peak shape, as well as to include a linear background. Since nonlinear fitting is sensitive to the initial guess, fairly good
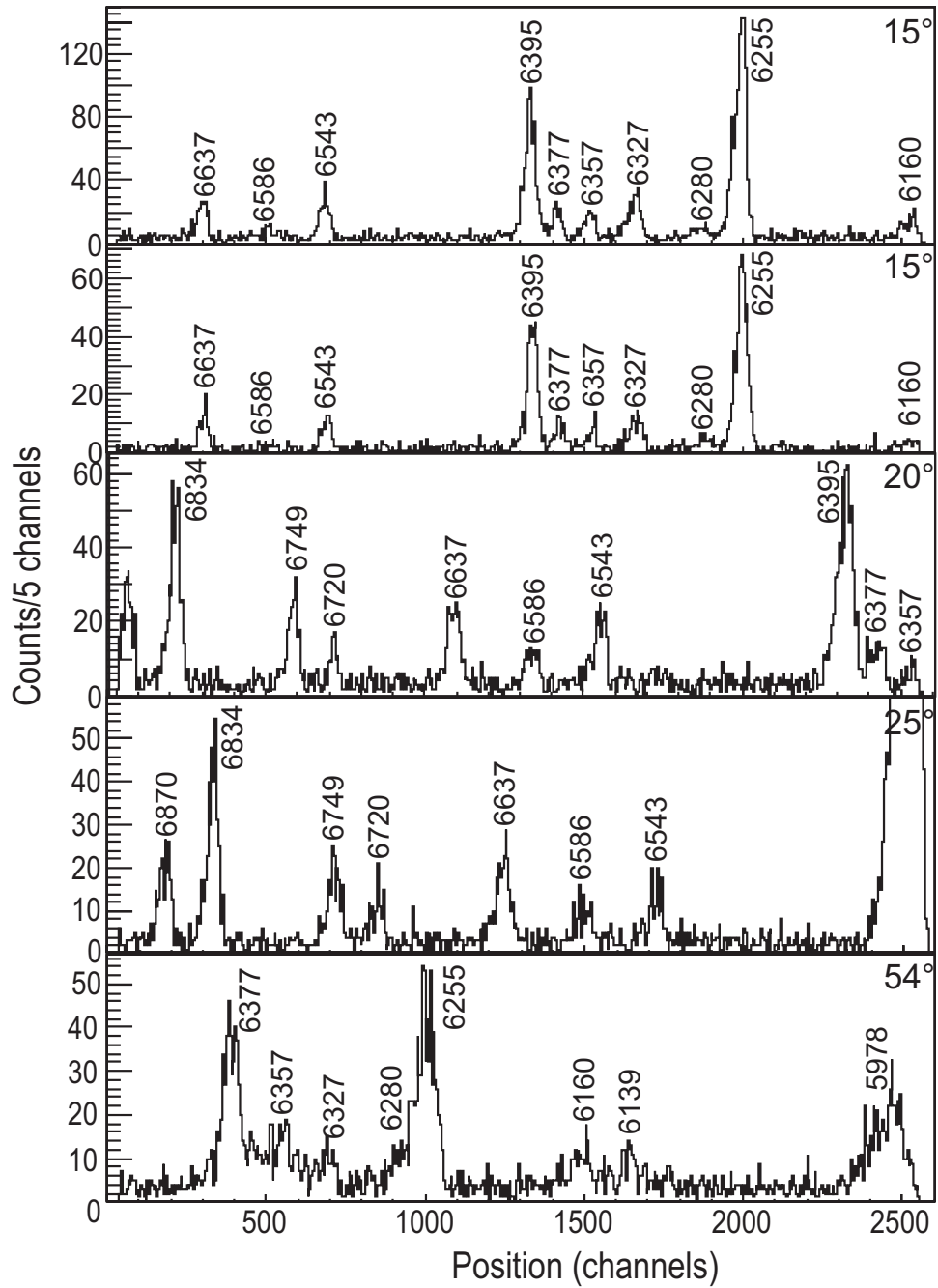
Figure 7.7 ^{32}S$(d,t)^{31}$S spectra used for calibration.

estimates of the fit parameters were needed as inputs. Output parameters for each peak were then written out to a data file. This fit was performed over various regions of the focal plane, being sure to select a large enough region to characterize the background. An example fit can be seen in
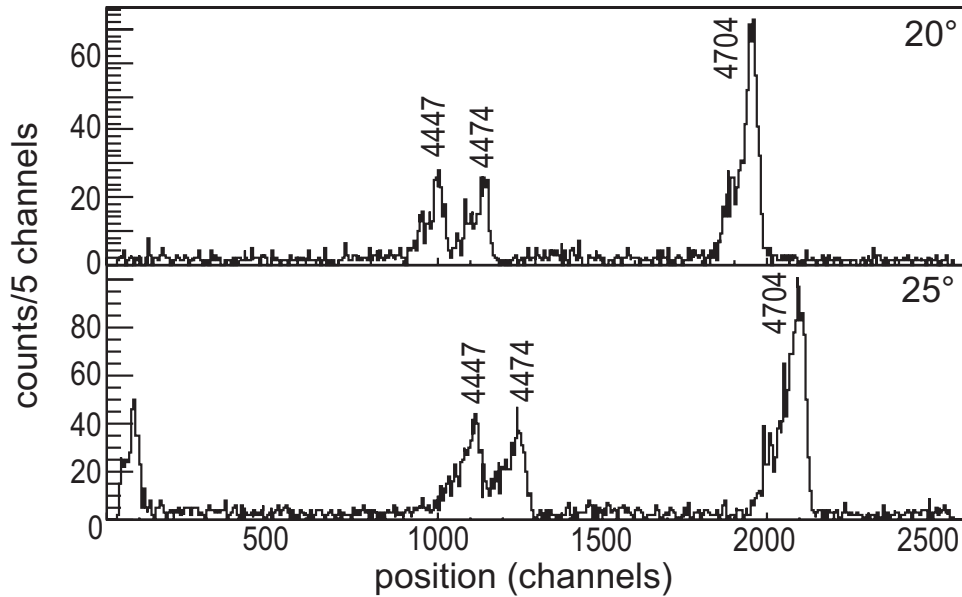
Figure 7.8 ^{28}Si(d,t)^{27}Si spectra used for calibration.

Figure 7.9. For these fits, τ was fixed for each spectrograph angle, and σ was fixed based on the widths of nearby high statistics peaks.

For one case, the left edge of the focal plane in the 54° spectrum, the fitting was complicated by the fact that there were no well isolated peaks in the region. The width for each peak in this fit was constrained by the widths of other peaks in the ^{35}Ar data at this angle and peaks near the left edge of the focal plane in the ^{31}S data, accounting for the kinematic broadening. Then, this region was fit with a flat background and adding peaks until a reasonable value of χ^2/ν was achieved. Based on this procedure, 6 peaks were used in the fit. This fit can be seen in Figure 7.10.

7.5   Calibration

Once peak centroids have been extracted for all of the peaks of interest and calibration peaks, a calibration can then be applied to extract energies for the peaks of interest. This calibration was done using a program called SPANC (SPlitpole Analysis Code), which is also a part of the Nukesim-classes package [63]. Inputs for SPANC include a description of the targets, a list of the
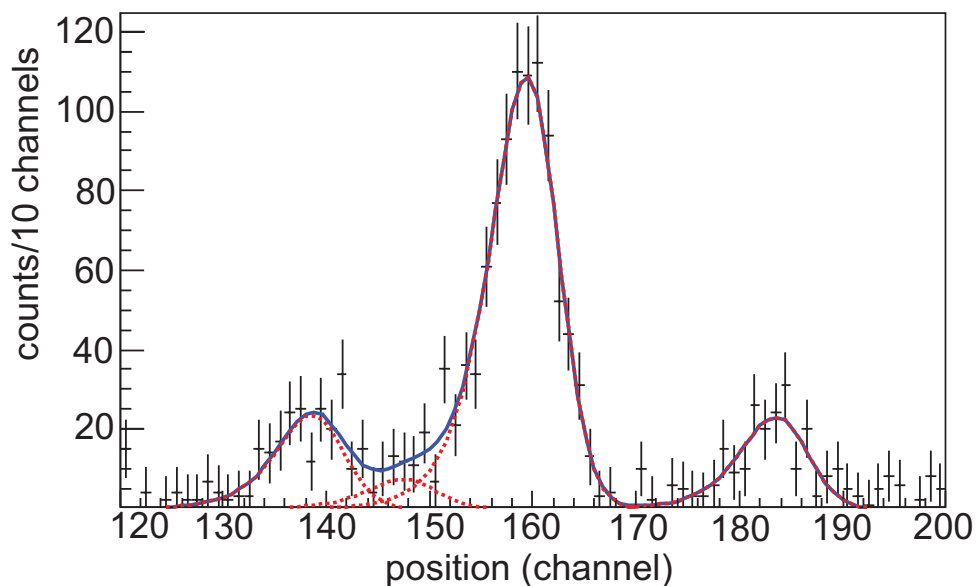
Figure 7.9 Example of the fit procedure used in the data analysis. Shown is the middle of the focal plane in the 54° ^{36}Ar$(d,t)^{35}$Ar data.
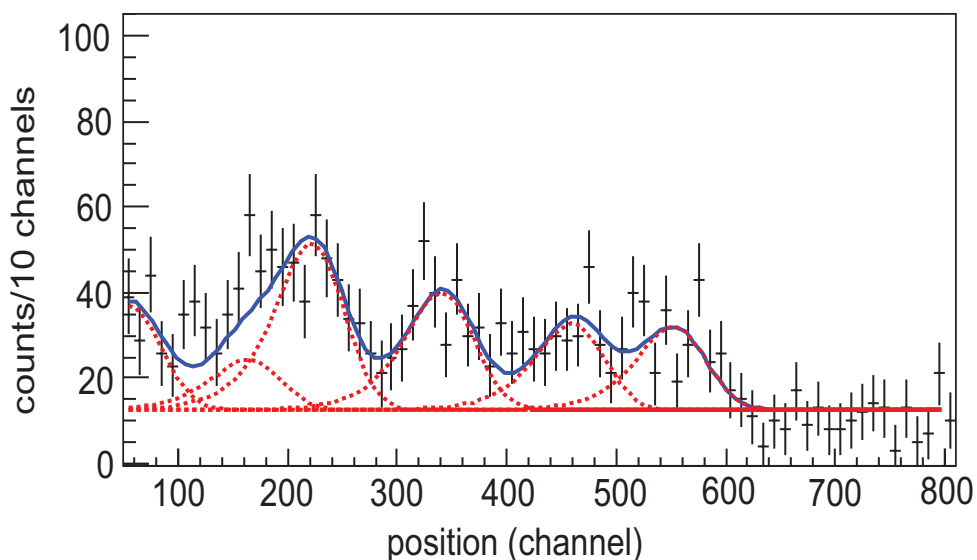
Figure 7.10 Fit for the left of edge of the focal plane at 54° for ^{36}Ar$(d,t)^{35}$Ar .

reactions, the beam energy, the projectile's charge state, the spectrograph angle and B field, and the energy and position of each calibration peak. To estimate the energy loss in these targets, it is assumed that the interaction occurs in the center of the target.

This code also requires as input the ground state masses of all nuclei in the reaction, to calculate

the Q values. Incorrect Q value calculations lead to a systematic shift in the extracted energies. Since SPANC was written, using AME 2003 [64], two new mass evaluations have been released, and the recommended mass for ^{31}S has changed by ≈ 1 keV. To properly account for this, mass values were updated in the code to reflect the then current values in AME 2012 [66].

For the calibration peaks, SPANC then calculates the expected ρ value for each calibration peak. For this measurement, calibration peaks from ^{31}S were used at all angles, and at $20°$ and $25°$, ^{27}Si peaks were also used. SPANC then fits ρ as a function of channel number. Once this fit is obtained, this can be applied to the centroids of other peaks to extract excitation energies. Peaks used for calibration were those that had low uncertainties, did not appear to be part of a doublet, and were located across but completely on the focal plane. SPANC then outputs the energies of input peaks, given their centroids. An example of these windows can be seen in Figure 7.11.
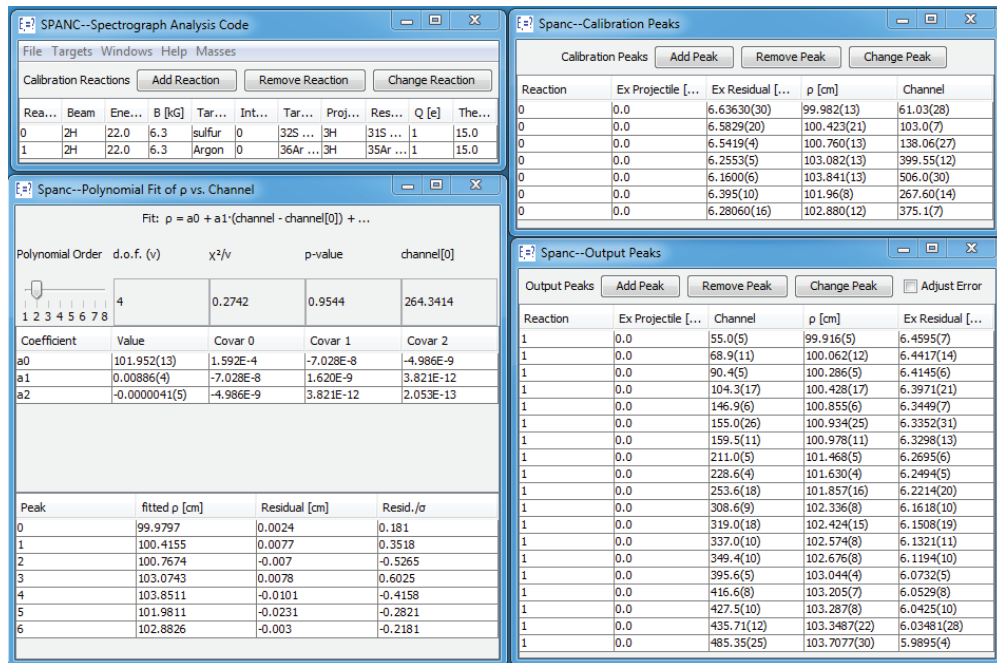
Figure 7.11 SPANC windows for the 15° data.

7.6   Excitation energies in ^{35}Ar

SPANC can take in the centroid of a peak and the uncertainty of that peak and output an excitation energy and a corresponding statistical uncertainty. In addition to statistical uncertainties, systematic effects also need to be considered. When the calibration or the averaging over the values obtained for different states had a value of $\sqrt{\chi^2/\nu}$ greater than unity, the statistical uncertainty was inflated by that factor. This lead to inflated statistical uncertainties of 1-2 keV.

The fit routines were varied to estimate systematic uncertainties, and these were found to be 1 keV. Potential shifts in beam energy and Q3D magnetic field were tracked using high yield peaks from ^{12}C$(d,\alpha)^{10}$B corresponding to the ground and first excited states of ^{10}B. A sample spectrum can be seen in Figure 7.12. In addition to these uncertainties, there exist conflicting literature data on the excitation energies of ^{31}S. This discrepancy is discussed in Section 2.3.4. These discrepancies span a range of $\approx$4 keV [9]. Calibration energies were dominated by one of these two data sets. We then shifted all energies downward by 2 keV to account for these discrepancies and added a 2 keV uncertainty to cover both possibilities.

Combining all of these systematic uncertainties in quadrature ($\delta E_{sys}^2 = \delta E_{fit}^2 + \delta E_{shift}^2 + \delta E_{calib}^2$) gives an overall systematic uncertainty of 2.4 keV. This systematic uncertainty is then combined in quadrature with the statistical uncertainty (inflated if the agreement at different angles is poor, as discussed previously), leading to total uncertainties of 3-5 keV, depending on the level. The extracted energies can be seen in Table ?? and Figure 7.13.

Two criteria were required to claim the discovery of a new level. First, it was required that each peak be observed in at least two spectrograph angles at the 3σ level, which provided kinematic confirmation that the peak was in fact from ^{35}Ar. Second, the significance of the peak was also required to be greater than 5σ total, where significances of peaks at separate angles are added in quadrature. Applying these criteria, 17 new levels were discovered, and the uncertainties in the excitation energies of 5 known levels were decreased by a factor of $\approx$3.
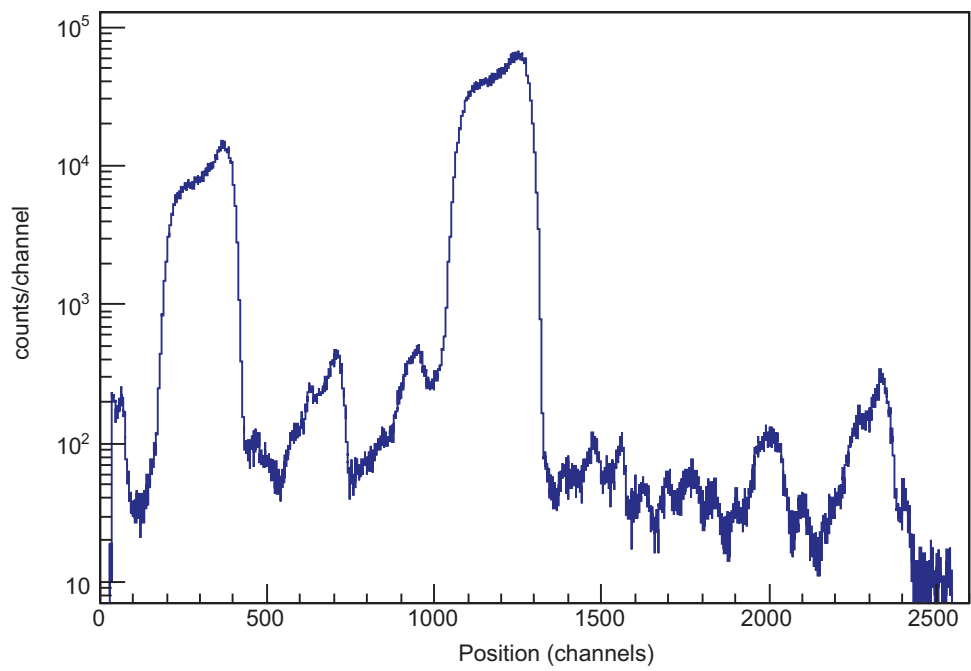
Figure 7.12 15° data gated on α particles, which was used to track drifts in the beam energy and magnetic fields.
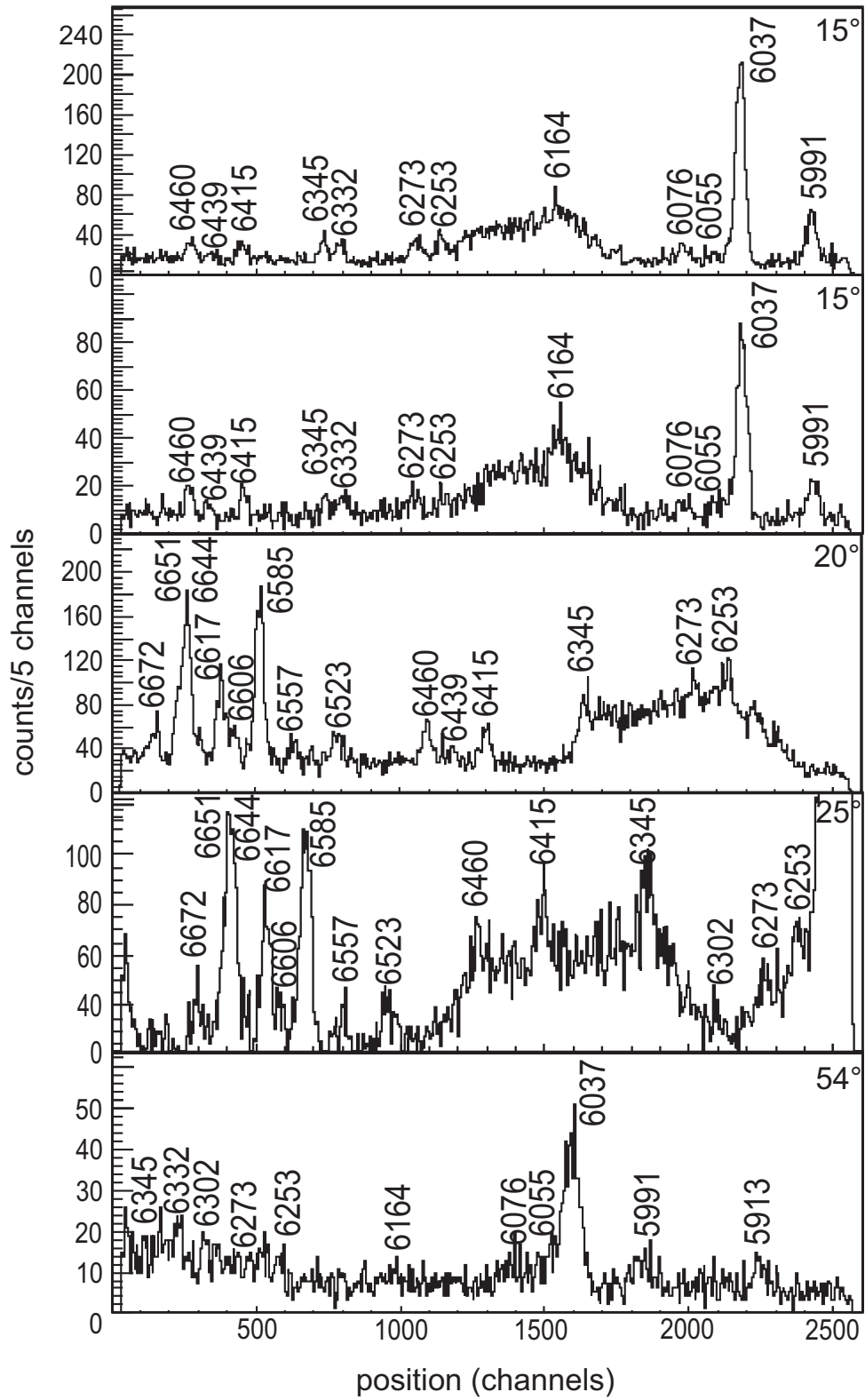
Figure 7.13 Position spectra from ^{36}Ar$(d,t)^{35}$Ar labeled with excitation energy in keV.

84

15°		15°		20°		25°		54°	
E_x (keV)	significance (σ)	E_x (keV)	significance (σ)	E_x (keV)	significance (σ)	E_x (keV)	significance (σ)	E_x (keV)	significance (σ)
								5913(5)	2.3
5994(2)	13	5990(2)	7.6					5994(3)	5.1
6039(2)	37	6038(2)	22					6041(3)	22
6057(2)	3.1							6065(7)	1.1
6078(2)	6.6	6078(2)	3.0					6082(3)	5.4
6167(2)	3.0	6167(2)	4.1					6168(4)	2.4
6254(3)	6.8	6256(3)	3.1	6256(3)	5.9	6256(3)	5.8	6260(5)	3.6
6273(3)	6.9	6277(3)	3.5	6276(3)	3.3	6275(3)	3.7	6281(4)	4.0
						6304(3)	8.5	6308(3)	5.9
6334(3)	7.0	6334(3)	4.7					6335(3)	4.2
6348(3)	6.2	6348(3)	3.9	6345(3)	5.9	6347(3)	5.6	6349(4)	3.2
6417(3)	5.2	6416(3)	5.9	6413(6)	8.9	6417(3)	5.0		
6444(3)	2.2	6446(3)	2.8	6437(3)	3.8				
6461(3)	6.4	6463(3)	5.9	6456(3)	8.4	6461(3)	3.7		
				6525(3)	5.8	6526(3)	5.3		
				6559(3)	5.4	6559(3)	3.3		
				6586(2)	25	6588(2)	18		
				6608(3)	5.6	6608(3)	6.1		
				6618(2)	12	6619(2)	15		
				6647(2)	4.1	6645(2)	7.6		
				6654(3)	5.1	6652(3)	3.4		
				6674(3)	14	6672(3)	3.7		

Table 7.1 ^{35}Ar excitation energies measured in each spectrum and the statistical significances of the corresponding peaks, expressed as standard deviations (σ). Uncertainties quoted include systematic uncertainties and statistical uncertainties from individual fits. Two separate measurements were taken at 15°. The results from the higher statistics measurements are reported in the left-most column and shown in the top panel of Figure 7.13.

E_x NDS [11]	E_x ^{36}Ar(^{3}He,α)^{35}Ar [45][1]	E_x ^{36}Ar(d,t)^{35}Ar present	E_r (C.M.) ^{34g}Cl(p,γ) present	E_r (C.M.) ^{34m}Cl(p,γ) present
5911(10)	5916(3)	5913(5)[2]	17(5)	
		5991(3)	95(3)	
6032(10)	6036(3)	6037(3)	140(3)	
		6055(3)[3]	158(3)	12(3)
		6076(3)	180(3)	33(3)
6153(10)	6162(2)	6164(3)	268(3)	122(3)
6258(10)	6267(12)	6253(3)	357(3)	210(3)
		6273(3)	376(3)	230(3)
		6302(3)	406(3)	259(3)
		6332(3)	436(3)	289(3)
		6345(3)	448(3)	302(3)
		6415(2)	518(2)	372(2)
		6439(4)[4]	543(4)	396(4)
		6460(3)	563(3)	417(3)
		6523(3)	627(3)	480(3)
		6557(3)	661(3)	515(3)
		6585(3)	689(3)	543(3)
		6606(3)	710(3)	563(3)
6630(10)	6614(2)	6617(2)	720(2)	574(2)
		6644(3)	748(3)	601(3)
		6651(3)	755(3)	608(3)
		6672(3)	775(3)	629(3)

Table 7.2 Previous and present ^{35}Ar excitation energies and corresponding center of mass (C.M.) resonance energies (keV) from the present work.

7.7 Level densities

^{35}Ar and ^{35}Cl are called a mirror pair. Their structure is expected to be similar because they differ by only one nucleon, a proton for ^{35}Ar and a neutron for ^{35}Cl. Therefore, the level density of ^{35}Cl should be able to provide some insight for what to expect in ^{35}Ar. However, if one compares

[1]unpublished
[2]only observed at 54°
[3]tentative
[4]tentative

the measured level density of ^{35}Ar to the level density of the mirror nucleus, ^{35}Cl, in this region of excitation energy, there are roughyly 10 more levels in ^{35}Ar. This can lead to one of two conclusions. Either some of the features that have been attributed to ^{35}Ar are from a contaminant, or some of the ^{35}Cl levels in this region have not yet been discovered. As a first check of potential contaminants, we looked at the ratio of beam currents for the various isotopes in the argon bottle used for the target implantation. These values agree well with the solar values, as shown in Table 7.3. Due to magnetic analysis of the ion beam, only mass 36 is delivered to the target.

mass number A	beam current (nA)	current ratio (%)	solar abundance (%)
36	19	0.315	0.334
38	4	0.066	0.063
40	6000	99.618	99.603

Table 7.3 Comparison of isotopic abundances in the argon bottle used for implanted targets and solar isotopic ratios.

Based on the focusing settings of the Q3D spectrograph, any triton groups from a reaction on anything with a different mass would be defocused (for an example, see the ^{28}Si$(d,t)^{27}$Si calibration data). Along with these considerations, all levels have been observed in spectra from at least two spectrograph angles. Due to the kinematics, one would not expect these features to all move together if they were not from the same nucleus.

Our measured level density is also greater than one would expect from an *sd* shell model calculation. However, at these excitation energies, one should also consider excitations of nucleons into the *pf* shell. $sd - pf$ shell model calculations including 0, 1, and 2 nucleon excitation from the *sd* shell into the *pf* shell by Alex Brown were compared to data. These level densities agree quite well, as shown in Figure 7.14. Further details can be found in [58] and references therein.

Based on these calculations and our experimental level density for ^{35}Ar, it is clear that there are still many undiscovered mirror levels in ^{35}Cl. However, even with the larger ^{35}Ar level density, this level density is not quite sufficient to rely on Hauser-Feshbach model calculations to produce the ^{34g,m}Cl$(p,\gamma)^{35}$Ar reaction rates in this case [67, 68], so detailed properties of individual res-
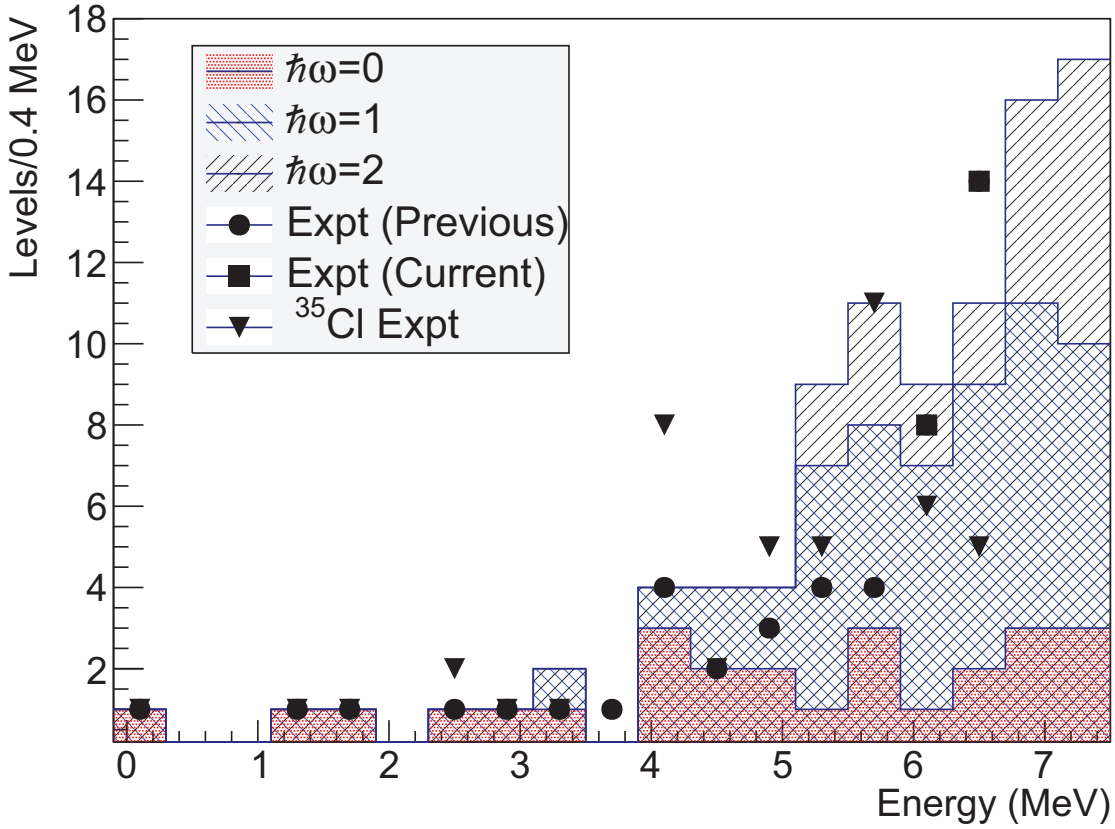
Figure 7.14 Experimental level densities of ^{35}Ar and the mirror nucleus ^{35}Cl and calculated shell model level densities. Experimental level densities for ^{35}Ar with $E_x < 5.9$ MeV and ^{35}Cl are taken from [11].

onances discovered in this work need to be determined. Only resonance energies are insufficient to constrain the reaction rate, but further information on these resonances could be used to guide matching of these levels to shell model states to create a hybrid reaction rate.

CHAPTER 8

SUMMARY AND OUTLOOK

This work has presented transfer reaction studies which are steps toward understanding nucleosynthesis in ONe classical novae, in particular, the production of ^{30}Si and ^{34}S. Here I provide a brief summary of this work and discuss future work to better understand the relevant reaction rates.

The experiment outlined in Chapters 3-5 endeavored to determine total widths of known ^{31}S resonances using the Doppler Shift Attenuation method, using the ^{32}S(^{3}He,α)^{31}S reaction. The first run of this experiment failed due to background that can be attributed to carbon on the target, and beam hitting a copper collimator due to a mis-wired quadrupole magnet. Data from a second run are still under analysis, but preliminary analysis shows an improvement in signal to noise in the new run. We expect to be able to set constraints on lifetimes of two relevant resonances.

Before the experiment presented in Chapters 6 and 7, only six levels in the astrophysical region of interest were known, most without a certain spin assignment, and all with energy uncertainties of at least 10 keV. In our effort at MLL, using ^{36}Ar(d,t)^{35}Ar, we discovered 17 new levels, and reduced uncertainties on new levels to typically 3 keV. Discovering most, if not all of the levels in the region of interest aids planning and analysis of future experiments to constrain the spins, parities, and partial widths of these resonances.

While these experiments are important steps toward understanding two reaction rates important for classical nova nucleosnythesis, ^{30}P(p,γ)^{31}S and ^{34g,m}Cl(p,γ)^{35}Ar, further experiments are needed. Partial widths of ^{31}S resonances need further experimental constraints. To complement the lifetime measurements presented here, a ^{31}Cl(βp)^{30}P measurement is scheduled in November 2018 at the NSCL to measure proton branching ratios for selected resonances [69]. Another experiment to better understand ^{34g,m}Cl(p,γ)^{35}Ar was recently run at the Argonne Tandem Linear Accelerator System measured γ-ray angular angular distributions for ^{35}Ar resonances populated via ^{32}S(α,n)^{35}Ar [70], which should lead to J^{π} constraints.

Further steps are still necessary to understand both of these reaction rates. Discrepancies exist among different data sets for ^{31}S resonance energies and spin assignments which need to be resolved with the help of further measurements. Further constraints on the partial widths are also needed, as some, but not all states were populated in this DSAM measurements. ^{35}Ar experimental data is much more incomplete, and several future experiments will be needed for a fully experimental ^{34g,m}Cl$(p,\gamma)^{35}$Ar reaction rate.

These two reaction rates warrant further study to reduce nuclear physics uncertainties in classical nova models used to understand nucleosynthesis in classical novae, particularly to understand silicon and sulfur isotopic ratios in presolar grains formed in classical novae.

BIBLIOGRAPHY

BIBLIOGRAPHY

[1] C. Iliadis. *Nuclear Physics of Stars*. Wiley-VCH Verlag, 2007.

[2] A. Sarangi and I. Cherchneff. Condensation of dust in the ejecta of Type II-P supernovae. *Astronomy and Astrophysics*, 575:A95, March 2015.

[3] Presolar grains in meteorites. `http://presolargrains.net/`, 1999.

[4] J. José, M. Hernanz, S. Amari, K. Lodders, and E. Zinner. The Imprint of Nova Nucleosynthesis in Presolar Grains. *Astrophysical Journal*, 612:414–428, September 2004.

[5] Peter Hoppe, Jan Leitner, Elmar Gröner, K Marhas, Bradley S. Meyer, and Sachiko Amari. Nanosims studies of small presolar SiC grains: New insights into supernova nucleosynthesis, chemistry, and dust formation. *Astrophysical Journal, v.719, 1370-1384 (2010)*, 719, 08 2010.

[6] J. Jose. Novae: theory and observations. In *11th Symposium on the Nuclei in the Cosmos*, page 50. Proceedings of Science, 2010.

[7] L. N. Downen, C. Iliadis, J. José, and S. Starrfield. Nuclear Thermometers for Classical Novae. *Astrophys. J.*, 762:105, January 2013.

[8] J. José, M. Hernanz, S. Amari, K. Lodders, and E. Zinner. The Imprint of Nova Nucleosynthesis in Presolar Grains. *Astrophys. J.*, 612:414–428, September 2004.

[9] C. Ouellet and B. Singh. Nuclear Data Sheets for A=31. *Nucl. Data Sheets*, 114:209–396, February 2013.

[10] A. Coc, M.-G. Porquet, and F. Nowacki. Lifetimes of ^{26}Al and ^{34}Cl in an astrophysical plasma. *Phys. Rev. C*, 61(1):015801, January 1999.

[11] J. Chen, J. Cameron, and B. Singh. Nuclear Data Sheets for A = 35. *Nucl. Data Sheets*, 112:2715–2850, November 2011.

[12] O. S. Kirsebom, P. Bender, A. Cheeseman, G. Christian, R. Churchman, D. S. Cross, B. Davids, L. J. Evitts, J. Fallis, N. Galinski, A. B. Garnsworthy, G. Hackman, J. Lighthall, S. Ketelhut, P. Machule, D. Miller, S. T. Nielsen, C. R. Nobs, C. J. Pearson, M. M. Rajabali, A. J. Radich, A. Rojas, C. Ruiz, A. Sanetullaev, C. D. Unsworth, and C. Wrede. Measurement of lifetimes in ^{23}Mg. *Physical Review C*, 93(2):025802, February 2016.

[13] Evaluated nuclear structure data file retrieval. `http://www.nndc.bnl.gov/ensdf/`.

[14] C. Wrede, K. Deryckx, B. M. Freeman, A. García, G. C. Harper, A. S. C. Palmer, D. A. Short, and D. I. Will. Preparation of ^{20}Ne, ^{24}Mg, ^{28}Si, ^{32}S, and ^{36}Ar targets by ion implantation into thin carbon foils. *Nucl. Instrum. Methods Phys. Res. B*, 268:3482–3484, December 2010.

[15] H. F. Wirth. *Bau eines hochauflösenden Fokalebenendetektors für den Münchner Q3D-Magnetspektrographen Untersuchungen zur Kernstruktur von* ^{129}Te. PhD thesis, Technischen Universität München, 2001.

[16] H.-F. Wirth, H. Angerer, T. von Egidy, Y. Eisermann, G. Graw, and R. Hertenberger. New Q3D Focal Plane Detector with Cathode-strip Readout Became Operational. *Maier-Leibnitz-Laboratorium Annual Report*, page 71, 2000.

[17] S. Starrfield, C. Iliadis, and W. R. Hix. The thermonuclear runaway and the classical nova outburst. *Publications of the Astronomical Society of the Pacific*, 128(963):051001, 2016.

[18] B. T. Draine. Interstellar Dust Models and Evolutionary Implications. In T. Henning, E. Grün, and J. Steinacker, editors, *Cosmic Dust - Near and Far*, volume 414 of *Astronomical Society of the Pacific Conference Series*, page 453, December 2009.

[19] K. Lodders and S. Amari. Presolar grains from meteorites: Remnants from the early times of the solar system. *Chemie der Erde / Geochemistry*, 65:93–166, May 2005.

[20] Z. R. Dai, J. P. Bradley, D. J. Joswiak, D. E. Brownlee, H. G. M. Hill, and M. J. Genge. Possible in situ formation of meteoritic nanodiamonds in the early solar system. *Nature*, 418:157–159, 2002.

[21] L. R. Nittler. Presolar stardust in meteorites: recent advances and scientific frontiers. *Earth and Planetary Science Letters*, 209:259–273, April 2003.

[22] Ian J Thompson and Filomena M Nunes. *Nuclear reactions for astrophysics: principles, calculation and applications of low-energy reactions*. Cambridge Univ. Press, Cambridge, 2009.

[23] R. L. Kozub. (p,d) Reaction on N=Z Nuclei in the 2s-1d Shell. *Phys. Rev.*, 172:1078–1094, August 1968.

[24] Z. Ma, D. W. Bardayan, J. C. Blackmon, R. P. Fitzgerald, M. W. Guidry, W. R. Hix, K. L. Jones, R. L. Kozub, R. J. Livesay, M. S. Smith, J. S. Thomas, and D. W. Visser. Astrophysically important ^{31}S states studied with the $^{32}S(p,d)^{31}S$ reaction. *Phys. Rev. C*, 76:015803, Jul 2007.

[25] D. Irvine, A. A. Chen, A. Parikh, K. Setoodehnia, T. Faestermann, R. Hertenberger, H.-F. Wirth, V. Bildstein, S. Bishop, J. A. Clark, C. M. Deibel, J. Hendriks, C. Herlitzius, R. Krücken, W. N. Lennard, O. Lepyoshkina, R. Longland, G. Rugel, D. Seiler, K. Straub, and C. Wrede. Evidence for the existence of the astrophysically important 6.40-MeV state of ^{31}S. *Phys. Rev. C*, 88(5):055803, November 2013.

[26] D. T. Irvine. A Study of the Astrophysically Important States of ^{31}S via the $^{32}S(d,t)^{31}S$ Reaction. Master's thesis, McMaster University, 2012.

[27] F. Ajzenberg-Selove and J. L. Wiza. Energy Levels of ^{31}S. *Phys. Rev.*, 143:853–855, Mar 1966.

[28] T. S. Bhatia, W. W. Daehnick, and G. J. Wagner. Search for $1p$ Neutron Strength in ^{31}S by the Reaction ^{32}S(^{3}He, α)^{31}S. *Phys. Rev. C*, 5:111–117, Jan 1972.

[29] J. Vernotte, G. Berrier-Ronsin, S. Fortier, E. Hourani, A. Khendriche, J.M. Maison, L.-H. Rosier, G. Rotbard, E. Caurier, and F. Nowacki. One-nucleon pickup reactions on ^{32}S: Experimental results and shell-model calculations. *Nucl. Phys. A*, 655:415–439, 1999.

[30] D. G. Jenkins, A. Meadowcroft, C. J. Lister, M. P. Carpenter, P. Chowdhury, N. J. Hammond, R. V. F. Janssens, T. L. Khoo, T. Lauritsen, D. Seweryniak, T. Davinson, P. J. Woods, A. Jokinen, H. Penttila, G. Martínez-Pinedo, and J. José. Reevaluation of the ^{30}P(p,γ)^{31}S astrophysical reaction rate from a study of the $T = 1/2$ mirror nuclei, ^{31}S and ^{31}P. *Phys. Rev. C*, 73:065802, Jun 2006.

[31] D. T. Doherty, G. Lotay, P. J. Woods, D. Seweryniak, M. P. Carpenter, C. J. Chiara, H. M. David, R. V. F. Janssens, L. Trache, and S. Zhu. Key Resonances in the ^{30}P(p,γ)^{31}S Gateway Reaction for the Production of Heavy Elements in ONe Novae. *Phys. Rev. Lett.*, 108:262502, Jun 2012.

[32] F. Della Vedova, S. M. Lenzi, M. Ionescu-Bujor, N. Mărginean, E. Farnea, M. Nespolo, G. de Angelis, M. Axiotis, D. Bazzacco, A. Bizzeti-Sona, P. G. Bizzeti, F. Brandolini, D. Bucurescu, A. Iordachescu, S. Lunardi, R. Menegazzo, D. R. Napoli, C. Rossi Alvarez, and C. A. Ur. Isospin Symmetry Along The N=Z Line In The sd Shell. *AIP Conference Proceedings*, 764(1):205–210, 2005.

[33] N. S. Pattabiraman, D. G. Jenkins, M. A. Bentley, R. Wadsworth, C. J. Lister, M. P. Carpenter, R. V. F. Janssens, T. L. Khoo, T. Lauritsen, D. Seweryniak, S. Zhu, G. Lotay, P. J. Woods, Krishichayan, and P. Van Isacker. Analog $E1$ transitions and isospin mixing. *Phys. Rev. C*, 78:024301, Aug 2008.

[34] C. Wrede, J. A. Caggiano, J. A. Clark, C. Deibel, A. Parikh, and P. D. Parker. New ^{30}P(p,γ)^{31}S resonances and oxygen-neon nova nucleosynthesis. *Phys. Rev. C*, 76:052802, Nov 2007.

[35] C. Wrede, J. A. Caggiano, J. A. Clark, C. M. Deibel, A. Parikh, and P. D. Parker. Measurements of ^{31}S energy levels and reevaluation of the thermonuclear resonant ^{30}P(p,γ)^{31}S reaction rate. *Phys. Rev. C*, 79(4):045803, April 2009.

[36] A. Parikh, K. Wimmer, T. Faestermann, R. Hertenberger, J. José, R. Longland, H.-F. Wirth, V. Bildstein, S. Bishop, A. A. Chen, J. A. Clark, C. M. Deibel, C. Herlitzius, R. Krücken, D. Seiler, K. Straub, and C. Wrede. Improving the ^{30}P(p,γ)^{31}S rate in oxygen-neon novae: Constraints on J$^{\pi}$ values for proton-threshold states in ^{31}S. *Phys. Rev. C*, 83(4):045806, April 2011.

[37] A. Kankainen, T. Eronen, S.P. Fox, H.O.U. Fynbo, U. Hager, J. Hakala, J. Huikari, D.G. Jenkins, A. Jokinen, S. Kopecky, I. Moore, A. Nieminen, H. Penttiä, S. Rinta-Antila, O. Tengblad, Y. Wang, and J. Äystö. Excited states in ^{31}S studied via beta decay of ^{31}Cl. *Eur. Phys. J. A*, 27:67–75, 2006.

[38] A. Saastamoinen. *Studies of T_z=-3/2 Nuclei of Astrophysical Interest*. PhD thesis, Univesity of Jyväskylä, 2011.

[39] M. B. Bennett, C. Wrede, B. A. Brown, S. N. Liddick, D. Pérez-Loureiro, D. W. Bardayan, A. A. Chen, K. A. Chipps, C. Fry, B. E. Glassman, C. Langer, N. R. Larson, E. I. McNeice, Z. Meisel, W. Ong, P. D. O'Malley, S. D. Pain, C. J. Prokop, H. Schatz, S. B. Schwartz, S. Suchyta, P. Thompson, M. Walters, and X. Xu. Isospin mixing reveals $^{30}P(p,\gamma)^{31}S$ resonance influencing nova nucleosynthesis. *Phys. Rev. Lett.*, 116:102502, Mar 2016.

[40] A. Parikh, K. Wimmer, T. Faestermann, R. Hertenberger, J. José, H.-F. Wirth, C. Hinke, R. Krücken, D. Seiler, K. Steiger, and K. Straub. Isotopic $^{32}S/^{33}S$ ratio as a diagnostic of presolar grains from novae. *Phys. Lett. B*, 737:314–319, October 2014.

[41] Nan Liu, Larry R. Nittler, Conel M. O'D. Alexander, Jianhua Wang, Marco Pignatari, Jordi José, and Ann Nguyen. Stellar origins of extremely ^{13}C- and ^{15}N-enriched presolar SiC grains: Novae or supernovae? *The Astrophysical Journal*, 820(2):140, 2016.

[42] P. Hoppe, W. Fujiya, and E. Zinner. Sulfur Molecule Chemistry in Supernova Ejecta Recorded by Silicon Carbide Stardust. *Astrophys. J. Lett.*, 745:L26, February 2012.

[43] R. R. Johnson and R. J. Griffiths. The ^{40}Ar(p, d) ^{39}Ar and ^{36}Ar(p, d) ^{35}Ar reactions at 27.5 MeV. *Nucl. Phys. A*, 108:113–123, January 1968.

[44] R. R. Betts, H. T. Fortune, and R. Middleton. Neutron Pickup from ^{36}Ar. *Phys. Rev. C*, 8:660–669, August 1973.

[45] S.-N. D. Vouzoukas. *A Study of the Levels of Astrophysical Importance in ^{32}Cl and ^{35}Ar*. PhD thesis, Univesity of Notre Dame, 1998.

[46] E. K. Warburton, J. W. Olness, and A. R. Poletti. Nuclear structure of ^{22}Na.i. gamma-ray correlations and lifetime measurements for levels of $E_{ex} < 3.1$ MeV. *Phys. Rev.*, 160:938–963, Aug 1967.

[47] K Jayamanna, G Wight, D Gallop, R Dube, V Jovicic, C Laforge, M Marchetto, M Leross, D Louie, R Laplante, Robert Laxdal, M McDonald, G J Wiebe, V Wang, and Fang Yan. A multicharge ion source (supernanogan) for the OLIS facility at ISAC/TRIUMF. In *Review of Scientific Instruments*, volume 81, page 02A331. 03 2010.

[48] Glenn F Knoll. *Radiation detection and measurement; 4th ed.* Wiley, New York, NY, 2010.

[49] A.B. Garnsworthy, C.J. Pearson, D. Bishop, B. Shaw, J.K. Smith, M. Bowry, V. Bildstein, G. Hackman, P.E. Garrett, Y. Linn, J.-P. Martin, W.J. Mills, and C.E. Svensson. The griffin data acquisition system. *Nuclear Instruments and Methods in Physics Research Section A: Accelerators, Spectrometers, Detectors and Associated Equipment*, 853:85 – 104, 2017.

[50] O.B. Tarasov and D. Bazin. Development of the program lise: application to fusion–evaporation. *Nuclear Instruments and Methods in Physics Research Section B: Beam Interactions with Materials and Atoms*, 204:174 – 178, 2003.

[51] A. Gavron. Statistical model calculations in heavy ion reactions. *Phys. Rev. C*, 21:230–236, Jan 1980.

[52] LISE++ team. Lise++. `http://lise.nscl.msu.edu/lise.html`.

[53] S. Mythili, B. Davids, T. K. Alexander, G. C. Ball, M. Chicoine, R. S. Chakrawarthy, R. Churchman, J. S. Forster, S. Gujrathi, G. Hackman, D. Howell, R. Kanungo, J. R. Leslie, E. Padilla, C. J. Pearson, C. Ruiz, G. Ruprecht, M. A. Schumaker, I. Tanihata, C. Vockenhuber, P. Walden, and S. Yen. Lifetimes of states in ^{19}Ne above the ^{15}O+α breakup threshold. *Physical Review C*, 77(3):035803, March 2008.

[54] N. Galinski, S. K. L. Sjue, G. C. Ball, D. S. Cross, B. Davids, H. Al Falou, A. B. Garnsworthy, G. Hackman, U. Hager, D. A. Howell, M. Jones, R. Kanungo, R. Kshetri, K. G. Leach, J. R. Leslie, M. Moukaddam, J. N. Orce, E. T. Rand, C. Ruiz, G. Ruprecht, M. A. Schumaker, C. E. Svensson, S. Triambak, and C. D. Unsworth. Lifetime measurements of states in ^{15}O. *Physical Review C*, 90(3):035803, September 2014.

[55] M.G. Herman, T.M. Cormier, and M. Satteson. Statistical origin of the highest-energy fusion-induced gamma rays. *Physics Letters B*, 203(1):29, 1988.

[56] C. Wrede, J. A. Clark, C. M. Deibel, T. Faestermann, R. Hertenberger, A. Parikh, H.-F. Wirth, S. Bishop, A. A. Chen, K. Eppinger, B. M. Freeman, R. Krücken, O. Lepyoshkina, G. Rugel, and K. Setoodehnia. Properties of ^{20}Na, ^{24}Al, ^{28}P, ^{32}Cl, and ^{36}K for studies of explosive hydrogen burning. *Phys. Rev. C*, 82(3):035805, September 2010.

[57] C. Wrede, J. A. Clark, C. M. Deibel, T. Faestermann, R. Hertenberger, A. Parikh, H.-F. Wirth, S. Bishop, A. A. Chen, K. Eppinger, A. García, R. Krücken, O. Lepyoshkina, G. Rugel, and K. Setoodehnia. Toward precise Q_{EC} values for the superallowed $0^+ \to 0^+$ β decays of T=2 nuclides: The masses of ^{20}Na, ^{24}Al, ^{28}P, and ^{32}Cl. *Phys. Rev. C*, 81(5):055503, May 2010.

[58] C. Fry, C. Wrede, S. Bishop, B. A. Brown, A. A. Chen, T. Faestermann, R. Hertenberger, A. Parikh, D. Pérez-Loureiro, H.-F. Wirth, A. García, and R. Ortez. Discovery of ^{34g,m}Cl $(p,\gamma)^{35}$Ar resonances activated at classical nova temperatures. *Phys. Rev. C*, 91(1):015803, January 2015.

[59] W. N. Lennard, K. Setoodehnia, A. A. Chen, and J. Hendriks. Ion-implanted ^{32}S targets for astrophysics studies. *Nucl. Instrum. Methods Phys. Res. B*, 269:2726–2729, December 2011.

[60] R. Hertenberger, A. Metz, Y. Eisermann, K. El Abiary, A. Ludewig, C. Pertl, S. Trieb, H.-F. Wirth, P. Schiemenz, and G. Graw. The Stern-Gerlach polarized ion source for the Munich MP-tandem laboratory, a bright source for unpolarized hydrogen and helium ion beams as well. *Nucl. Instrum. Methods Phys. Res. A*, 536:266–272, January 2005.

[61] W. Assmann, J. De Boer, U. Meyer-Berkhout, S. Skorka, E. Huenges, P. Kienle, H. Morinaga, E. Nolte, H. Vonach, H. Münzer, L. Rohrer, and H. Schnitter. The Munich MP tandem. *Nuclear Instruments and Methods*, 122:191–203, December 1974.

[62] R Lutter, O. Schaile, K. Schöffel, K. Steinberger, and C. Broude. Marabou, 2015.

[63] D. Visser. nukesim-classes: Java classes for nuclear physics simulation. `http://nukesim-classes.sourceforge.net/`.

[64] G. Audi, A. H. Wapstra, and C. Thibault. The Ame2003 atomic mass evaluation: (II). Tables, graphs and references. *Nucl. Phys. A*, 729:337–676, 2003.

[65] R. Brun and F. Rademakers. ROOT — An object oriented data analysis framework. *Nucl. Instrum. Methods Phys. Res. A*, 389:81–86, 1997.

[66] G. Audi, A. H. Wapstra, F. G. Kondev, M. MacCormick, X. Xu, and B. Pfeiffer. The Ame2012 atomic mass evaluation: (II). Tables, graphs and references. *Chinese Physics C*, 36:1603–2014, 2012.

[67] T. Rauscher. private communication.

[68] T. Rauscher and F.-K. Thielemann. Astrophysical Reaction Rates From Statistical Model Calculations. *Atomic Data and Nuclear Data Tables*, 75:1–351, May 2000.

[69] C. Wrede for the e17024 collaboration. NSCL proposal: Beta delayed proton decay of ^{31}cl.

[70] R. S. Ilieva. *Gamma-Ray Spectroscopy Studies of Explosive Stellar Phenomena*. PhD thesis, Univesity of Surrey, 2017.